Synchrotron Studies of Technologically Important Metal Oxide Surfaces

Coinneach Murchadh MacKenzie Dover

Thesis submitted for the Degree of Doctor of Philosophy of the University College London

London Centre for Nanotechnology

UNIVERSITY COLLEGE LONDON

2014

I, Coinneach Dover, confirm that the work presented in this thesis is my own. Where information has been derived from other sources, I confirm that this has been indicated in the thesis.

Abstract

This thesis probes three technologically important metal-oxide systems; Pd nanoparticles supported on the TiO_2(110) surface, acetate on TiO_2(110) and Fe_3O_4(111). The orientation of CO adsorbed to a Pd/TiO_2(110) model catalyst system was probed using X-ray photoemission electron microscopy (XPEEM) and near-edge X-ray absorption fine structure (NEXAFS). The absorbed CO molecules were found to have an off-normal polar orientation, relative to the basal plane of the substrate. The result was interpreted as an average of several sets of CO molecules absorbed and oriented orthogonally to various facets of the Pd nanoparticles, some of the facets themselves orientated with an angular separation from the basal plane. The acetate saturated TiO_2(110) surface was examined using photoelectron spectroscopy (PES) and NEXAFS under UHV conditions as well as under increased pressures of acetic acid. The coverage and orientation of the adsorbed acetic acid were studied. It was found that a second 0.5 ML of acetate, additional to the half-monolayer film observed in UHV, develops under 0.01 Torr of acetic acid pressure. This second layer is thought to be hydrogen bonded to hydroxyl groups that are formed during the absorption of the first layer. Additionally, the 1st half-monolayer is shown to be slightly tilted, this is believed to be the effect of hydroxyls and to influence the tilt of the second layer. Structural characterisation work was carried out on the Fe_3O_4(111) single-crystal surface with low energy electron diffraction. Full characterisation was not possible due to incomplete experimental data, however, a novel version of the analysis software CLEED was developed to accommodate simultaneous mutliple domain analysis.

For my parents, my grandparents, my brothers and my nieces.

Acknowledgements

Thank you to my Supervisor Geoff Thornton for giving me the opportunity to undertake a postgraduate degree and for arranging for me to perform work at the University of Berkeley. Special consideration must go to Drs Christopher Muryn, David Grinter and Chi Ming Yim for their support academically which extended past their prescribed duties and was clearly a manifestation in all cases of a desire to serve and a love of a scientific field in which they are experts. I learned a lot from all of you in different ways which I will apply to my own future in academia.

Outside of the Thornton group, I would like to thank Dr Georg Held at the University of Reading for allowing me to attend his CLEED workshop and for his support in using his excellent CLEED software, Patrick Smears for his assistance and expertise with computing, Dr Eitan Abraham at the University of Heriot-Watt for his considerable support and excellent guidance during both my undergraduate and postgraduate studies and Dr Kenneth Rice and Dr Duncan Forgan at the Royal Observatory for allowing me to undertake a research project that I love.

Finally, I would like to extend a huge thank you to my immediate family and my friends for their support and their kind words.

List of Publications

Scanning Tunneling Microscopy and Molecular Dynamics Study of the Li_2TiO_3(001) Surface

K. Azuma, C. Dover, D,C, Grinter, R. Grua-Crespo N. Almora-Barrios, G. Thornton, T.Oda and S. Tanaka, *The Journal of Physical Chemistry C*, 10 (2013) 5126.

In preparation

Strain Influenced Molecular Bonding to Nanoparticles

C.M. Yim, C.L. Pang, D.R. Hermoso, C. Dover, C.A. Muryn, F. Maccherozzi, S.S. Dhesi, R. Perez and G. Thornton.

Glossary

AES	Auger Electron Spectroscopy
AEY	Auger Electron Yield
AL	Acceleration Lens
ALS	Advanced Light Source
APNEXAFS	Ambient Pressure Near-Edge X-ray Absorption Fine Structure
APPES	Ambient Pressure Photoelectron Spectroscopy
BFP	Back Focal Plane
BGS	Band Gap State
DLS	Diamond Light Source
DP	Dispersive Plane
E_F	Fermi Level
EP	Entrance Plane
FL	Field Lens
FT-RAIRS	Fourier Transform Reflection Absorption Infrared Spectroscopy
HOMO	Highest Occupied molecular Orbitals
IL	Intermediate Lens
I-V	Intensity vs Voltage

LEED	Low Energy Electron Diffraction
LEEM	Low Energy Electron Microscopy
LUMO	Lowest Unoccupied Molecular Orbital
KB	Kirkpatrick-Baez
MCP	Micro Channel Plate
μNEXAFS	Micro Near-Edge X-ray Absorption Fine Structure
μXAS	Micro X-ray Absorption Spectroscopy
μXPS	Micro X-ray Photoelectron Spectroscopy
ML	Monolayer
MO	Molecular Orbital
NEXAFS	Near-Edge X-ray Absorption Fine Structure
PEEM	Photoelectron Emission Microscopy
PES	Photoelectron Spectroscopy
R-factor	Reliability Factor of Pendry
RF	Radio Frequency
RFA	Retarding Field Energy Analyser
RL	Retarding Lens
RT	Room Temperature
PEY	Partial Electron Yield
SMSI	Strong Metal-Support Interaction

SPELEEM	Spectroscopic Photoemission and Low Energy Electron Microscope
STM	Scanning Tunnelling Microscopy
SXTM	Synchrotron X-ray Scanning Tunnelling Microscopy
TEY	Total Electron Yield
TL	Transfer Lens
UHV	Ultra High Vacuum
UV	Ultra Violet
VB	Valence Band
XAS	X-ray Absorption Spectroscopy
XMCD	X-ray Magnetic Circular Dichroism
XMLD	X-ray Magnetic Linear Dichroism
XPEEM	X-ray Photoelectron Emission Microscopy
XPS	X-ray Photoelectron Spectroscopy

Table of Contents

List of Figures

Chapter 1: Introduction

1.1 Surface Science

Experimental surface science, the discipline that focuses on studying the terminating atomic layers of materials became possible in the 1960s following two significant advances in science. Practically, the steadily improving field of vacuum technology had reached a stage where UHV technology (~10^{-9} Torr) had developed to a point where it could be combined with electron and photon sources in commercially available instruments. A sample that is kept in a UHV environment can remain unaffected by contaminants for the order of hours, providing ample time for characterisation by electrons or photons. Furthermore, in the same decade, single crystal samples became more widely available. Fundamentally, it became understood that low energy electrons (50-500 eV) could be used to probe surfaces. The technique of low energy electron diffraction was established already by the 1950s as a mode of assessing the quality of single crystal surfaces. It was known at this time that the directions of the backscattered beams were influenced by the degree of translational symmetry of the surface, which could be different from that of the bulk [1]. By the early 1970s, it was known that the inelastic scattering of low energy electrons via excited valence electrons was an important element of their interaction with solids. As low energy electrons have a short inelastic mean free path (few nm) in materials, it was postulated that the collected electrons must emit or scatter from the outermost layers [1].

The goal of solid state physics is to relate the macroscopic properties of materials to its atomic structure. Surface science is that branch of solid state physics which deals with the interface between a material and the atmosphere. Since the journal '*Surface Science'* was founded in 1964, several more journals have emerged dealing exclusively with surface phenomena and presently, surface science studies are a mainstay in more mainstream journals, such as '*Nature'*. It is now well known that the characterisation of the physical and chemical landscape of surfaces is important for understanding epitaxy [2], physical and chemical reactions at interfaces [3] and chemical bonding [4]. In industry, the study of surfaces has provided new insight in to catalysis [5], semi-conductors [6], plastics [7], corrosion [8] and adhesion [9].

Advances in technology have increased vastly the extent of information that can be collected from surfaces. The available instrumentation can be split into two major categories, spectroscopy and microscopy, which are used to provide markedly different surface characterisations. Surface spectroscopy is used to identify chemical constituents and their relative concentrations and surface microscopy is utilised in the characterisation of the morphology and the crystalline structure [10]. Additionally, more specialist information about local features is becoming available. For example, micro-spot XAS [11] and LEED [12] can provide spectroscopic information on specific domains of multi-phase surfaces as well as individual nanostructures and studies of surfaces under atmospheric pressure conditions can be carried out. These modern innovations serve to bridge the physical gap between laboratory conditions and the practical conditions under which industrially important materials are operated.

1.2 Catalysis

Catalysts accelerate chemical reactions by forming bonds with a set of reactants as they form a product which then detaches, leaving the catalyst unaltered and ready to facilitate the next set of reactants. A catalytic reaction is defined as one where the catalyst participates and is recovered in its original form following the completion of the reaction [13]. In figure 1.1 a potential energy diagram of the un-catalysed and catalysed reaction between molecules A and B are compared to illustrate how a reaction is accelerated by the presence of a catalyst.

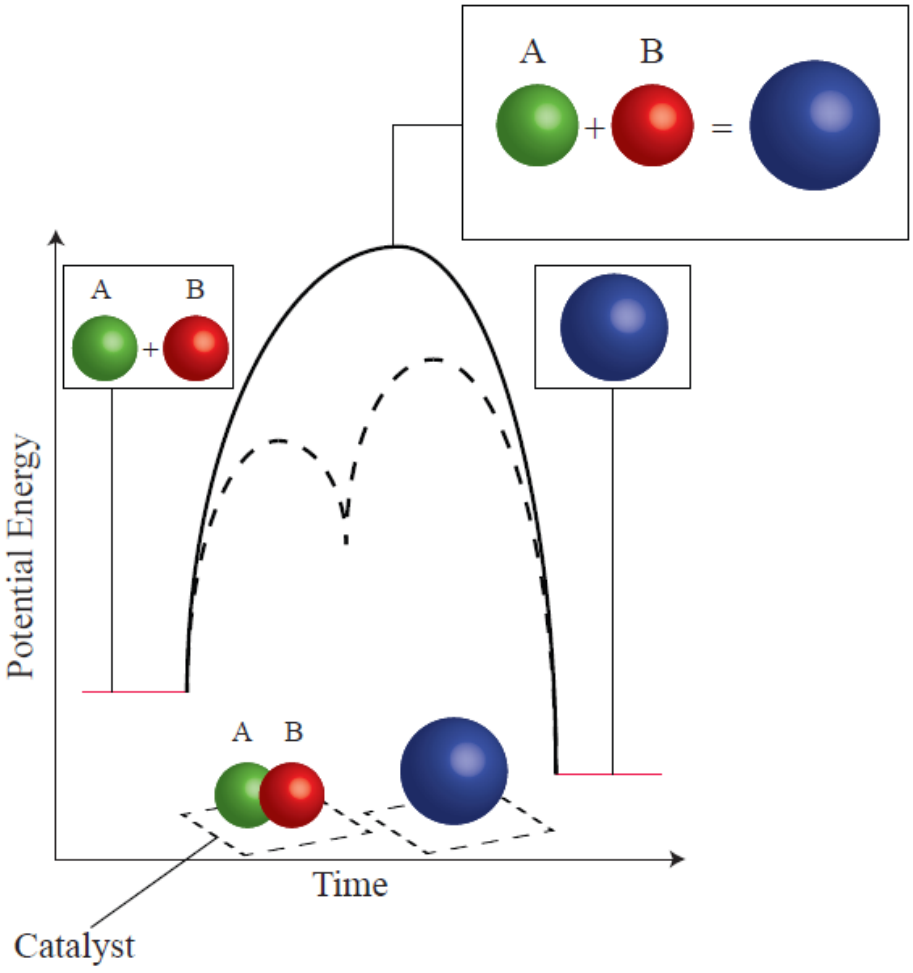

Fig 1.1: *Potential energy diagram of a heterogeneous catalytic reaction. Gaseous reactants and products and a solid catalyst. The uncatalysed reaction must overcome a considerable potential energy barrier. The barriers are much lower via the catalytic route.*

The diagram above illustrates that the catalytic path, while more complex, is energetically favourable. The potential energy barrier is lower for the catalysed reaction, i.e. the activation energy is far lower. Catalysis works both forwards and backwards, as the catalyst accelerates the bonding, it will hasten the decomposition to the same extent. Catalysis is a delicate process and for the reaction in figure 1.1, if A and B bond weakly to the catalyst, the overall reaction can be hindered rather than accelerated. Furthermore, the reaction rate will also be hindered should A, B, both A and B or their product bond too strongly to the surface. In this case, the catalyst is said to be poisoned [13].

In heterogeneous catalysis, reactions between gaseous molecules or molecules in solution are catalysed by a solid. Unless the catalyst is porous, in general the reactants will not penetrate the outermost atomic layer and the catalytic reaction will occur at the surface. To utilise precious metals, which often have powerful catalytic properties, in an economical manner, it is commonplace for catalysts to take the form of metallic nanoparticles, supported on an inert substrate. Heterogeneous catalysts of this nature are ubiquitous in the chemical and petro-chemistry industries [14,15].

1.3 Metal Oxides

In the ambient, almost all metal surfaces are oxidised [16]. Furthermore, metal oxides have an array of related interesting optical [17], magnetic [18] and electronic properties [19] that are applicable to industrial processes. Some metal oxides are industrially important semi-conductors [20], others are insulators [21], while some display metallic behaviour [22], some are sufficiently inert to function as corrosion protective coatings [23] and others are chemically

active as catalysts [24]. They are at the centre of many established and emergent techniques and in some cases, reactions at their surface or at their interface with an adjacent material is key to device function [25,26]. Furthermore, some metal oxides have most unique properties, such as yttrium barium copper oxide ($YBa_2Cu_3O_{7-x}$), which has the highest known critical temperature for superconductivity and was the first to be found with superconducting properties above the boiling point of liquid nitrogen [27]. Understanding the geometric and electronic landscape of metal oxide surfaces and the interaction of such surfaces with adsorbed molecules, nanoparticles and thin films is significant to a multitude of technological fields.

The surfaces of metal oxides are intrinsically complex. A single chemical composition can exist in several structural phases. The complexity is enhanced by the presence of various types of defects that can significantly affect the physical properties. Metal oxides that have a bandgap of ~3 eV and are semiconductors; TiO_2 [28], ZnO [29] and SnO_2 [30] have been extensively characterised using single crystal samples, cleaved to expose a single crystallographic termination [16]. Many significant metal oxides are insulators, rendering important surface science techniques that require a conducting surface obsolete [31]. In this case ultrathin films, a few monolayers in thickness, are synthesised on the surface to facilitate investigation.

1.4 Titanium Dioxide

Since work by Fujishima and Honda that demonstrated the photodecomposition of water by TiO_2(110) electrodes in the absence of an external bias [32], the photocatalytic properties of titanium dioxide have been extensively researched [33]. When ultraviolet radiation irradiates TiO_2 an electron-hole pair can form which may subsequently move towards the surface where

reactions with adsorbed water and oxygen can create radical species. These free radicals can decompose complex organic molecules, in some cases to CO_2 and H_2O [32]. This is the most investigated property of TiO_2 as it has a multitude of industrial applications [33]. Photo-assisted biodegradation is utilised in water purification [34], disinfection [35] and in self-cleaning and protective coatings [36,37].

Titanium dioxide is a semi-conductor and can change its conductivity in the presence of an adsorbate [38]. This property is applied to gas sensing [39] and TiO_2 can detect the partial pressure of oxygen over a large range of temperatures that are commonplace in the engines of automobiles. Therefore TiO_2 is used in car engines as an oxygen sensor to monitor the air/fuel mix [40]. TiO_2 also has a high refractive index and is widely used for colouring foods [41], paints [33], cosmetics [42] and pharmaceuticals [33]. Nano-scale thin TiO_2 films are utilised in electro-chromic devices that control the light transmission and reflection in windows and mirrors [43].

TiO_2 has many stable phases at different temperatures and thus reducing it by annealing is relatively straight-forward. This process produces n-type doping in TiO_2, significantly increasing the conductivity and, as a result, TiO_2 lends itself well to experimentation. Four distinct titanium dioxide minerals occur in nature; Akaogite [44], Anatase [45], Brookite [45] and Rutile [46]. The (110) termination of rutile is the most thermodynamically stable and extensively investigated [33] and as a consequence among the more completely characterised metal oxide facets. A model of the bulk-terminated TiO_2(110) surface is presented below in figure 1.2. Along the [001] direction are alternate rows of five-fold and six-fold coordinated Ti atoms. The five-fold coordinated Ti atoms have one dangling bond pointing out of the surface

and bridging oxygen atoms at the surface are bonded to six-fold coordinated Ti rows. Oxygen atoms within the main surface plane are three-fold coordinated [33].

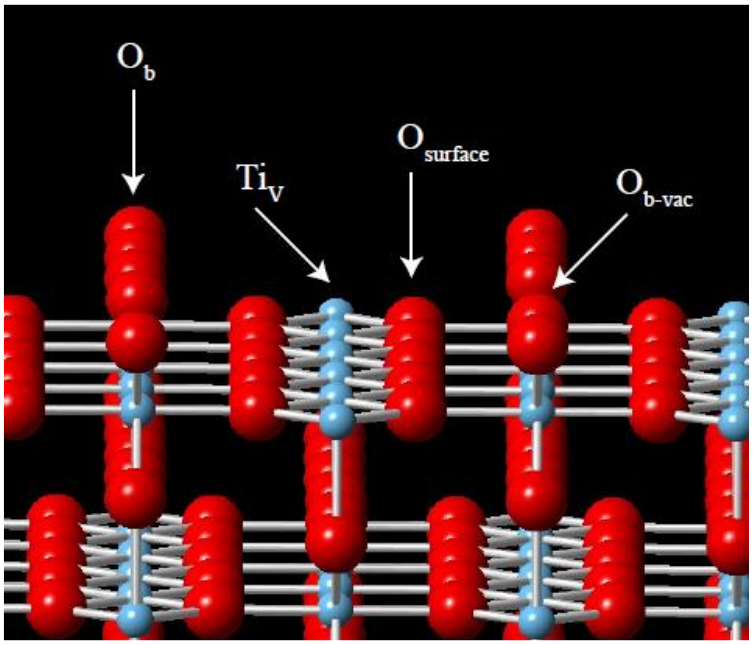

Fig 1.2: *Ball and stick model of rutile TiO_2 orientated to expose the (110) termination. Oxygen atoms are coloured red and smaller, blue spheres represent titanium. Three-fold coordinated oxygen atoms localised in the surface plane are labelled $O_{surface}$ and bridging oxygen atoms, bonded to six-fold coordinated Ti atoms, are labelled O_b. $O_{b\text{-}vac}$ sites are those where O_b atoms have been removed from the surface. Penta-coordinated Ti atoms are labelled Ti_V.*

Bridging oxygen atoms are two-fold coordinated and due to their coordinative under-saturation, they can be removed easily by annealing to create point defects which affect the reactivity of the surface significantly. The extent of these defects can be controlled and thus application-specific tailoring can be carried out. Figure 1.3 shows a typical STM image of the rutile TiO_2(110) surface where a small percentage of bridging oxygen atoms are missing. Oxygen vacancies appear as bright spots against the dark oxygen rows. Water dissociates at oxygen vacancies and two hydroxyl (OH) groups are formed. Both the bridging oxygen vacancy and hydroxyl features are indicated on figure 1.3.

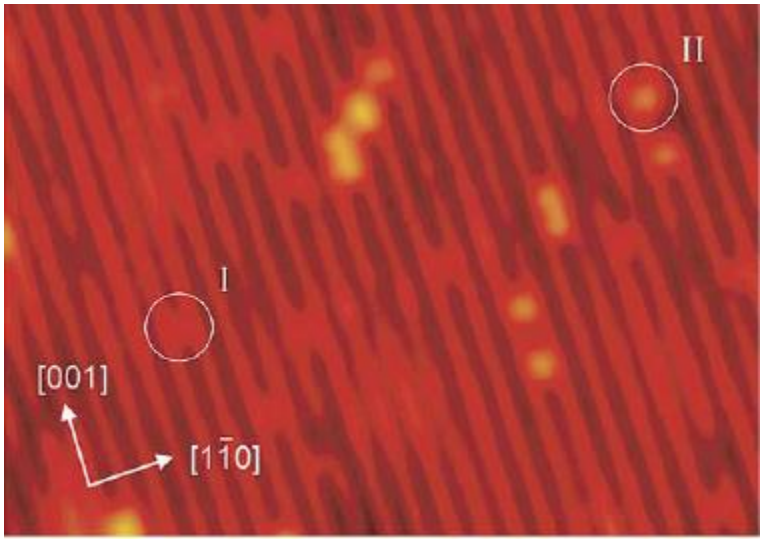

Fig 1.3: *STM image of TiO_2(110) with bright and dark rows assigned to titanium and oxygen respectively. Oxygen vacancies (I) and hydroxyl groups (II) appear at varying levels of brightness on bridging oxygen rows* [47]**.**

1.5 Iron Oxide

Iron oxides are among the most technologically useful transition metal oxides. They are compounds which are common in nature and readily synthesised in the laboratory [48]. Iron oxides are used extensively as a colouring pigment and as a magnetic pigment in electronic recording equipment [48,49]. They are also utilised in the catalysis of industrially important reactions such as the synthesis of ammonia [50], the water gas shift reaction [51], Fischer-Tropsch synthesis [52], dehydrogenation of ethylbenzene to styrene [53] and vapour phase oxidation of alcohols to aldehydes and ketones [54]. Iron has two variable oxidation states, Fe^{3+} and Fe^{2+} and forms three natural oxides; FeO (wüstite), Fe_3O_4 (magnetite) and α-Fe_2O_3 (hematite) [48]. And further oxides can be artificially synthesised; β-Fe_2O_3, ε-Fe_2O_3 and γ-Fe_3O_4 (maghemite). The specific phases are distinguished by a combination of the crystal structure and oxidation state and have unique chemical and catalytic properties [52]. Regarding the oxides synthesised under laboratory conditions; β-Fe_2O_3 can be formed through the dehydroxylation of β-FeOOH under high-vacuum at ~ 450 K [48]. The compound ε-Fe_2O_3 is

extant in a disordered, pure form as well as ordered form, intermediate between hematite and maghemite and can be prepared in various ways [48]. Finally, maghemite (γ-Fe_3O_4) can be prepared by heating other iron oxides, usually in the presence of organic matter [48]. Wüstite (FeO) contains divalent Fe ions only [48]. It has a rocksalt-type structure and is an important intermediate in the reduction of iron ores [48]. Hematite (α-Fe_2O_3) has a corundum structure and transformations of other iron oxides to hematite is quite common due to its stability [48]. Magnetite (Fe_3O_4) is a black, ferromagnetic mineral containing both Fe^{2+} and Fe^{3+} ions [48]. Together with titanomagnetite, it is responsible for the magnetic properties of rocks.

Fe_3O_4 crystallises in an inverse spinel structure, $[Fe^{3+}]_{tet}[Fe^{2+},Fe^{3+}]_{oct}O_4^{2-}$ where Fe^{2+} ions occupy octahedral sites and Fe^{3+} ions occupy octahedral and tetrahedral sites. The bulk structure of Fe_3O_4(111) consists of close packed oxygen layers separated by differently configured iron atoms. Hence, more than one surface termination can be exposed by cleavage through the (111) orientation. Three possible surface terminations of Fe_3O_4(111) have been identified by STM and they are identified in the schematic of Fe_3O_4 presented below in figure 1.4 [55].

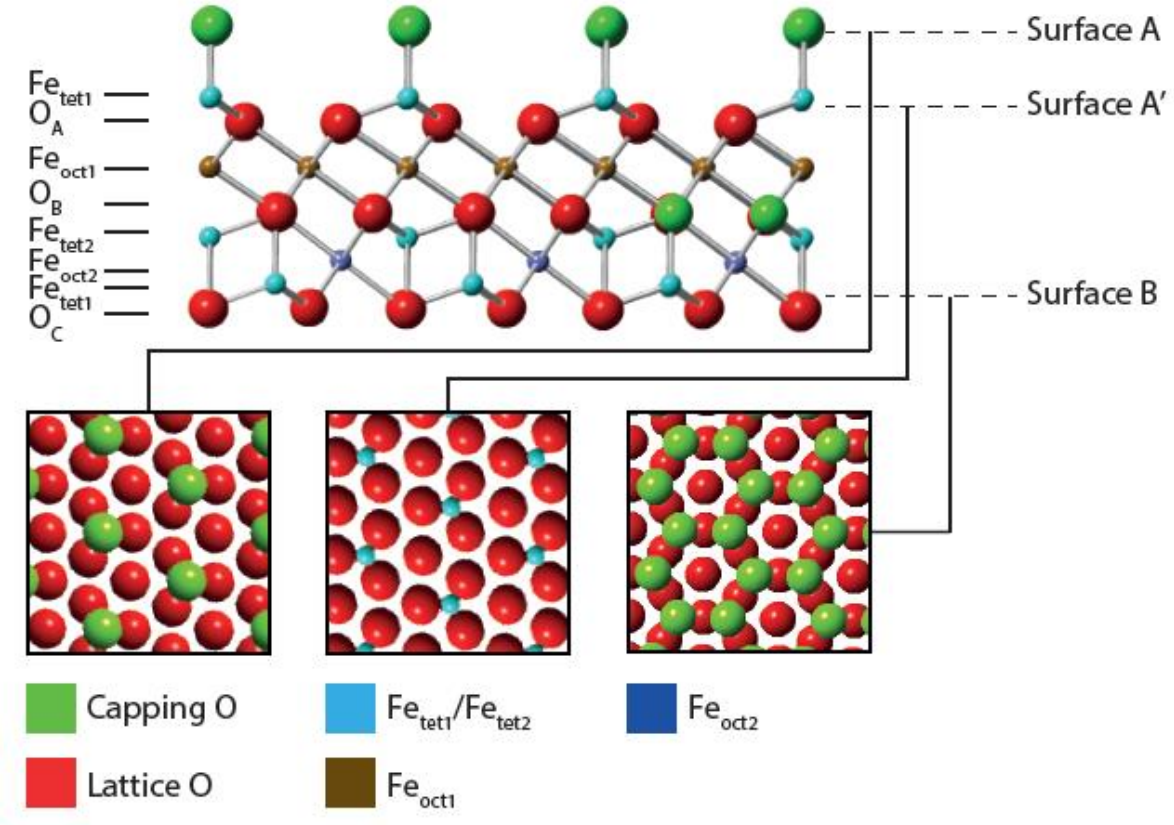

Fig 1.4: *Bulk structure of magnetite (Fe_3O_4), orientated to emphasise layers of atoms parallel to the (111) plane.*

The problem of applying surface science techniques that require a conducting surface to operate has motivated the extensive study of epitaxial iron oxide thin films. Fe-oxide thin films deposited on a variety of metal crystal substrates, including Pt(111) [56] and Ru(0001), have been studied [57]. Depending on the growth conditions, particularly the O_2 pressure, oxidation temperature and Fe coverage, thin films of FeO(111), Fe_3O_4(111) , and α-Fe_2O_3(0001) [54] can be prepared on a single crystal surfaces. Photoemission studies have suggested that these films are electronically equivalent to their bulk counterparts [58].

1.6 Dye-Sensitised Solar Cells (DSSCs)

Dye-sensitised solar cells (DSSCs) have attracted considerable scientific interest since being identified as a promising low-cost commercial third-generation photovoltaic device, building on second generation semi-conductor thin film solar panels [59]. Since their inception by O'Regan and Gratzel in the early 1990s [60], scientific research in this area has been focused primarily on improving efficiency and the simplification of manufacture while optimising durability and longevity [60]. As discussed in the previous section, TiO_2 is an established material in the field of solar power generation. It absorbs in the UV region and is transparent to visible light. In DSSCs, dye molecules that are adsorbed to the surface serve to increase the spectral range of light that can be converted to industrially useful electrical energy [60].

A schematic of a typical DSSC is presented in figure 1.5. Central to the cell is a nanocrystalline wide band-gap semiconductor (usually TiO_2) thin film that operates as an electrode, which is coated with light absorbing, charge-transferring dye. The free volume is occupied by an electrolyte containing a redox pair (in this example, I^- and I_3^-). When the solar cell is irradiated with photons, electrons in the dye molecules' highest occupied molecular orbitals (HOMO) are excited to the conduction band of the supporting metal oxide. This interaction, namely the injection of an electron from the dye to its metal oxide substrate, causes the photosensitising dye to become oxidised. The original state of the dye is restored by the donation of an electron from the electrolyte (in this example, an iodide/ triiiodide couple) and this prevents the recapture of the electron donated to the metal oxide by the dye. The iodide is regenerated in turn by reduction of triiodide at the counter electrode. The circuit is completed by the migration of the electron excited from the dye through the external load as electrical energy.

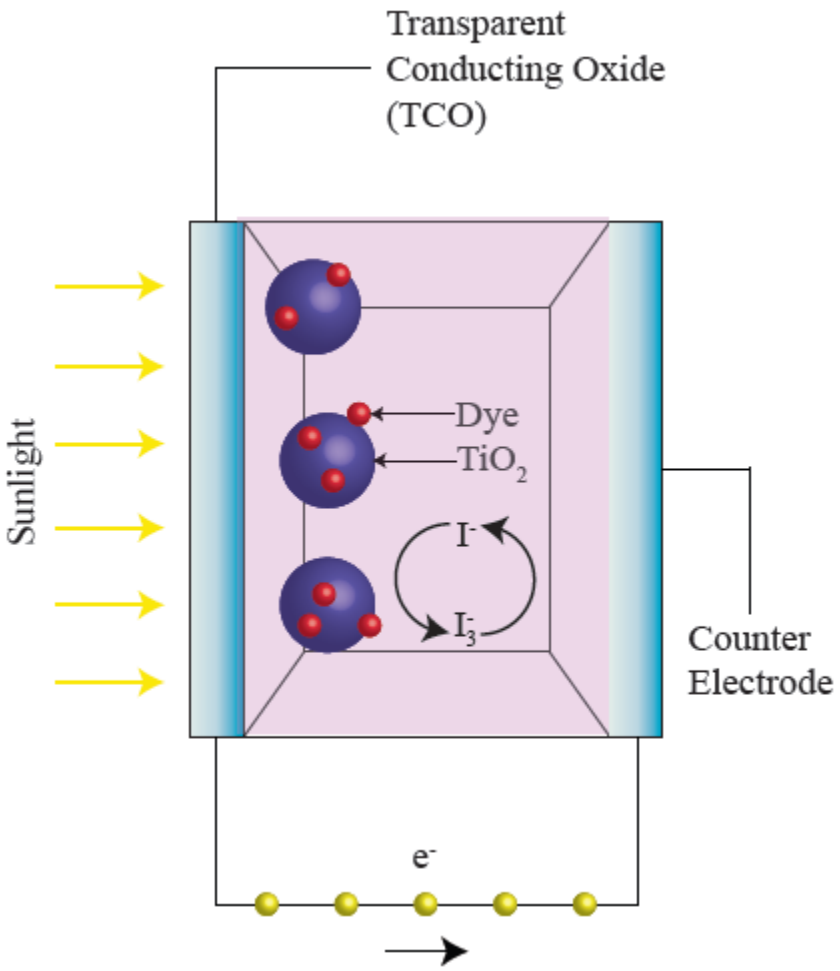

Fig 1.5: *Schematic of dye-sensitised solar cell and its key chemical components.*

It is essential that the photosensitising dye contains carbonyl (C=O) or hydroxyl (-OH) groups in order that it can anchor strongly to the TiO_2 substrate via the surface Ti sites. The carboxyl moiety contains both C=O and OH groups. The orientation of these anchoring groups are connected to the separation between the dye and the metal oxide, which in turn strongly influences the efficiency of the electron transfer between them [61].

References

[1] C.B. Duke, *Proceedings of the National Academy of Sciences*, **100** (2003) 3858.

[2] J. Narayan, *Metallurgical and Materials Transactions A: Physical Metallurgy and Materials*, **36** (2005) 5.

[3] N. Daniilidus and H.Haeffner, *Annual Review of Condensed Matter Physics*, **4** (2013) 83.

[4] J.T. Yates, *Surface Science*, **299** (1994) 731.

[5] P. Gallezot, S. Tretjak, Y. Christidis, G. Mattioda, A. Schouteeten, Y.W. Chung and T.S. Sriram, *Catalysis Letters*, **13** (1992) 305.

[6] T. Thundat, L.A. Nagahara and S.M. Lindsay, *Journal of Vacuum Science and Technology A Vacuum Surfaces and Films*, **8** (1990) 539.

[7] L.M. Bodecchi, M. Cocchi, M. Malagoli, M. Manfredini and A. Marchetti, *Analytic Chimica Acta*, **554** (2005) 207.

[8] E. Szocs, G. Vastag, A. Shaban, G. Konczos and E. Kalman, *Journal of Applied Electrochemistry*, **29** (1999) 1339.

[9] A. Banerjea, J.R. Smith and J. Ferrante, *Journal of Physics Condensed Matter*, **2** (1990) 8841.

[10] A. Zhao, S.J. Tan, B. Li, B.Wang, J.L. Wang and J.G. Hou, *Physical Chemistry Chemical Physics*, **15** (2013) 12428.

[11] S. Pascarelli, O. Mathon, M. Munoz, T. Mairs and J. Susini, *Journal of Synchrotron Radiation*, **13** (2006) 351.

[12] S. Agnoli, T.O. Mentes, M.A. Nino, A. Locatelli and G. Granozzi, *Physical Chemistry Chemical Physics*, **11** (2009) 3727.

[13] I. Chorkendorff and J.W. Niemantsverdriet, *Concepts of Modern Catalysis and Kinetics 2nd Ed.* (2003) Wiley.

[14] C. R. Henry, *Surface Science Reports*, **31** (1998) 231.

[15] I. Z. Jones, R. A. Bennett and M. Bowker, *Surface Science*, **439** (1999) 235.

[16] H.J. Freund, H. Kuhlenbeck and V. Staemmler, *Reports on Progress in Physics*, **59** (1996) 283.

[17] J.L. Musfeldt, *Functional Metal Oxide Nanostructures*, **149** (2012) 87.

[18] M. Gruyters, *Journal of Magnetism and Magnetic Materials*, **248** (2002) 248.

[19] A.Behnam, N.A. Radhakrishna, Z. Wu and A. Ural, *Applied Physics Letters*, **97** (2010) 233105.

[20] B. Sapoval and C. Hermann, *Physics of Semiconductors 1st Ed.* (2003) Springer.

[21] J.B. Torrance and P. Lacorre, *Physica C*, **182** (1991) 351.

[22] V.M. Bermudez, *Nature Materials*, **2** (2003) 218.

[23] W.K. Lu, R.L. Elsenbaumer and B. Wessling, *Synthetic Metals*, **71** (1995) 2163.

[24] C. Lahousse, A. Bernier, P. Grange, B. Delmon, P. Papaefthiminou, T. Ioannides and X. Verykios, *Journal of Catalysis*, **178** (1998) 214.

[25] Y.H. Kim, J.S. Heo, T.H. Kim, S. Park, M.H. Yoon, J. Kim, M.S. Oh, G.R. Yi, Y.Y. Noh and S.K. Park, *Nature*, **489** (2012) 128.

[26] G. Shen, P.C. Che, K. Ryu and C. Zhou, *Journal of Materials Chemistry*, **19** (2009) 828.

[27] A. Manthiram, J.S. Swinnea, Z.T. Sui, H. Steinfink and J.B. Goodenough, *Journal of the American Chemical Society*, **109** (1987) 6667.

[28] C.L. Pang, R. Lindsay, G. Thornton, *Chemical Reviews*, **113** (2013) 3887.

[29] U. Ozgur, Y.I. Alivov, C. Liu, A. Teke, M.A. Reshchikov, S. Dogan, V. Avrutin, S.J. Cho and H. Morkoc, *Journal of Applied Physics*, **98** (2005) 41301.

[30] M. Batzill and U. Diebold, *Progress in Surface Science*, **79** (2005) 47.

[31] S. Ramanathan, *Thin Film Metal-Oxides: Fundamentals and Applications in Electronics and Energy 1st Ed.* (2010) Springer.

[32] A. Fujishima and K. Honda, *Nature*, **238** (1972) 23.

[33] U. Diebold, *Surface Science Reports*, **48** (2003) 53.

[34] D. Suryaman and K. Hasegawa, *Journal of Hazardous Materials*, **183** (2010) 490.

[35] P.C. Maness, S. Smolinski and W.A. Jacoby, *Applied and Environmental Microbiology*, **65** (1999) 4094.

[36] Y. Paz, Z.Luo, L. Rabenburg and A. Heller, *Journal of Materials Research*, **10** (1995) 1455.

[37] I. Poulios, P. Spathis and P. Tsoumparis, *Journal of Environmental Science and Health*, **34** (1995) 1455.

[38] G. Sheveglieri, *Gas Sensors*, (1992) Dorrdrecht.

[39] P.K. Dutta, A. Ginwalla, B. Hogg, B.R. Patton, B. Chwieroth, Z. Liang, P. Gouma, M. Mills, S. Akbar, *Journal of Physical Chemistry*, **103** (1999) 4412.

[40] Y. Xu, K. Yao, X. Zhou and Q. Cao, *Sensors and Actuators*, **13** (1993) 492.

[41] L.G. Phillips and D.M. Barbano, *Journal of Dairy Science*, **80** (1997) 2726.

[42] J. Hewitt, *Cosmetics and Toiletries*, **114** (1999) 59.

[43] P. Bonhote, E. Gogniat, M. Gratzel and P.V. Ashrit, *Thin Solid Films*, **350** (1999) 269.

[44] P. Gillet and A. El Goresy, *Annual Review of Earth and Planetary Sciences*, **41** (2013) 257.

[45] G.V. Samsonov, *The Oxide Handbook 2nd Ed*. (1982) New York.

[46] F.A. Grant, *Reviews of Modern Physics*, **31** (1959) 646.

[47] S. Wendt, R. Schaub, J. Matthiesen, E.K. Vestergaard, E. Wahlstrom , M.D. Rasmussen, P. Thostrup, L.M. Molina, E. Laegsgaard, I. Stensgaard, B. Hammer and F. Besenbacher, *Surface Science*, **598** (2005) 226.

[48] R.M. Cornell and U. Schwertmann, *The Iron Oxides 2nd Ed.* (2003) Wiley.

[49] J.C. Mallinson, *The Foundations of Magnetic Recording 2nd Ed.* (1993) New York.

[50] N.D. Spencer, R.C. Schoonmaker, G.A. Somorjai, *Journal of Catalysis*, **74** 1982 129.

[51] G.C. Chinchen, R.H. Logan and M.S. Spencer, *Applied Catalysis*, **12** (1984) 69.

[52] R.A. Dictor and A.T. Bell, *Journal of Catalysis*, **97** (1986) 121.

[53] W. Weiss, D. Zscherpel and R. Schlogl, *Catalysis Letters*, **52** (1998) 215.

[54] X.Deng, J.Lee and C. Matranga, *Surface Science*, **604** (2010) 627.

[55] R.S. Cutting, C.A. Muryn, G. Thornton and D.J. Vaughan, *Geochimica et Cosmochimica Acta*, **70** (2006) 3593.

[56] M. Ritter, W. Ranke and W. Weiss, *Physical Review B*, **57** (1998) 7240.

[57] G. Ketteler and W. Ranke, *Journal of Physical Chemistry B*, **107** (2003) 4320.

[58] T. Schedel-Niedrig, W. Weiss and R. Schlogl, *Physical Review B*, **52** (1995) 17449.

[59] M. Grätzel, *Journal of Photochemistry and Photobiology C*, **4** (2003) 145.

[60] B. O'Regan, M. Grätzel, *Nature*, **335** (1991) 737.

[61] A.S. Hart, C.B. KC, H.B. Gobeze, L.R. Sequeira and F. D'Souza, *Applied Materials and Interfaces*, **5** (2013) 5314.

Chapter 2: Theoretical Background of Instrumentation

2.1 Synchrotron Radiation

Circular particle accelerators that move elementary particles around them were initially developed for the study of the subatomic structure of matter. In such installations, the orbiting charged particles were accelerated to close to the speed of light and as a result attained very high energy. The collisions between these highly energetic particles were scrutinised for the formation of novel subatomic particles. The electromagnetic radiation emitted while the particles were accelerated is referred to as synchrotron radiation and has many properties that are useful to experimental physics. It is available over a large region of the electromagnetic spectrum and is highly tuneable, brilliant and polarised. Synchrotron radiation was initially recovered parasitically from these early 1st generation sources. 2nd generation sources dedicated solely to the production and harnessing of synchrotron radiation using bending magnets were then developed before a third generation emerged where most of the radiation is extracted from so called insertion devices (undulators or wigglers) [1].

A schematic of the Diamond Light Source [2] (A 3rd generation source) is presented in figure 2.1 to illustrate the key components involved in the production of synchrotron light. Electrons are generated in an electron gun before being accelerated to high speeds by three particle accelerators. These are the linear accelerator (or linac), the booster synchrotron and the storage

ring. In the linac, initial acceleration of the particles is carried out using radio frequency (RF) cavities into the booster synchrotron. The booster synchrotron is comprised of two semi-circles, joined by two straight sections. In the curved sections the electrons are accelerated by bending magnets and in the straight section, by a further RF voltage. Once the electrons are sufficiently energetic, they are injected into the storage ring, which is a polygon comprised of straight sections, angled together with bending magnets. As the electrons pass by each bending magnet, they lose energy in the form of synchrotron radiation, which is channelled into the attached beamlines.

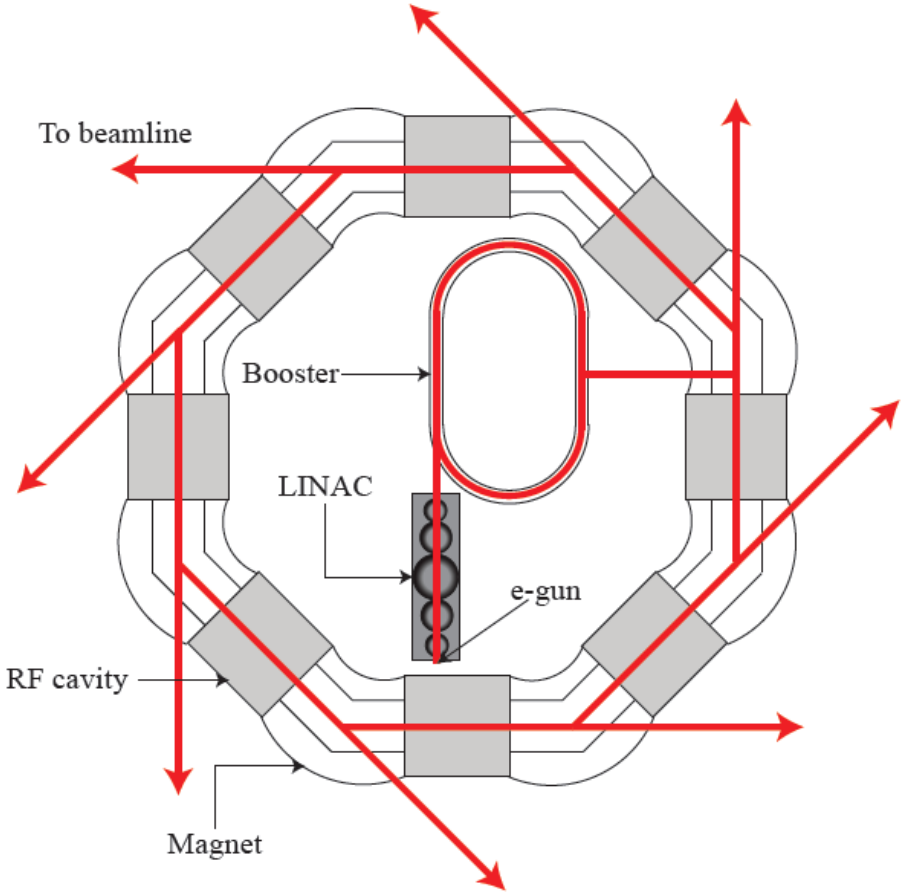

Fig 2.1: *Schematic of typical 3rd generation synchrotron source* [2].

The power radiated from an electron accelerated by the field, $\mathbf{E}_0$ is given by:

$$P = \frac{e^4}{6\pi\varepsilon_0 m^2 c^3} \cdot \mathbf{E}_0^2 \tag{2.1}$$

Where e is the electronic charge, ε_0 is the dielectric constant, m is the mass of an electron and c is the speed of light in a vacuum. The change in momentum of the particle due to acceleration is given by:

$$\frac{d\mathbf{p}}{dt} = e\mathbf{E}_0 \tag{2.2}$$

Therefore, 2.1 can be written as:

$$P = \frac{e^2}{6\pi\varepsilon_0 m^2 c^3}\left(\frac{d\mathbf{p}}{dt} \cdot \frac{d\mathbf{p}}{dt}\right) \tag{2.3}$$

This is known as the *Larmor* result for the total radiated power due to the instantaneous acceleration of a non-relativistic charged particle. It is independent of the nature of the field through which the particle is accelerated (i.e. magnetic or electric). Synchrotron radiation is generated in the static magnetic fields of bending magnets and undulators along the circumference of the storage ring. To describe the relativistic acceleration of electrons in the storage ring, the *Larmor* result can be cast in a Lorentz-invarient (reference frame-independent) form. Compared with 2.3, dt is replaced by the *proper time element*, $d\tau$ and $\mathbf{p}$ with the four-momentum vector $p_\mu = (\mathbf{p}, i\xi/c)$:

$$P = \frac{e^2}{6\pi\varepsilon_0 m^2 c^3} \sum_{\mu=1}^{4} \left(\frac{dp_\mu}{d\tau}\right)^2 \tag{2.4(i)}$$

$$= \frac{e^2}{6\pi\varepsilon_0 m^2 c^3} \left[\frac{d\mathbf{p}}{d\tau} \cdot \frac{d\mathbf{p}}{d\tau} - \frac{1}{c^2}\left(\frac{d\xi}{d\tau}\right)^2\right] \tag{2.4(ii)}$$

Where $\mathbf{p}$ is the momentum of the particle and ξ is its energy.

One can then obtain an expression for the power radiated when a bending magnet exerts a uniform magnetic field upon an electron in the storage ring. Through the action of the Lorentz force, the direction of the momentum of the electron is changed while its energy is not. The lattermost term in 2.4(ii) is therefore zero. Corresponding with figure 2.2., the electron's circular orbit around the magnet has a radius R. The change of momentum per unit time is:

$$\frac{d\mathbf{p}}{dt} = \mathbf{p}\frac{v}{R} \tag{2.5}$$

Where the physical quantities are measured from the reference frame of a stationary observer. Defining $\beta = v/c$ and the *relativistic factor* $\gamma = 1/(1-\beta^2)^{\frac{1}{2}}$, then $v = \beta c$, $\mathbf{p} = \gamma m \beta c$ and $dt = \gamma d\tau$ in 2.5. Substitution into 2.3 yields:

$$P = \frac{e^2 c}{6\pi\varepsilon_0}\frac{\gamma^4\beta^4}{R^2} \simeq \frac{e^2 c}{6\pi\varepsilon_0}\frac{\xi^4}{\xi_0^4}\frac{1}{R^2} \tag{2.6}$$

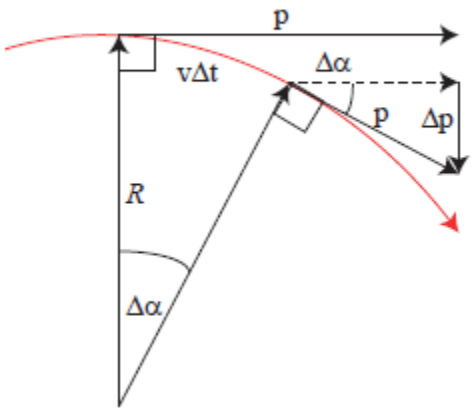

Fig 2.2: *Segment of circular orbit of an electron through a bending magnet. It follows that* $\frac{v\Delta t}{R} = \frac{\Delta p}{p}$.

In the final step the following substitutions were made; $\beta \to 1$ and $\gamma = \xi/\xi_0$ where $\xi_0 = mc^2 = 0.511\ MeV$, is the rest mass of the electron. Bending magnets in synchrotrons are able to cause single electrons to radiate a power of the order of kW per metre.

A non-relativistic electron radiates according to a $\sin\alpha$ distribution, where α is the angular separation between the direction in which the electron is accelerated and the direction from which it is observed. Figure 2.3 shows this schematically, the image at the top represents radiative emission from a non-relativistically accelerated charge and at the bottom the emission from a relativistically accelerated charge and it is evident there is a stark difference between the two. The relativistically accelerated charged particle is strongly peaked in the forward direction.

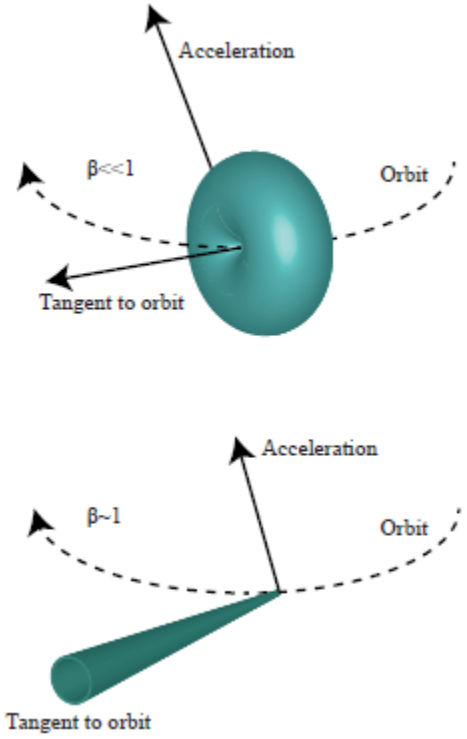

Fig 2.3*: Angular distribution of the intensity radiated by a radially accelerated electron. Top; The non-relativistic case where the electron radiates according to a sin α distribution and bottom; the relativistic case where a sharp cone of radiation is emitted* [1].

The opening angle of the cone of radiation arising in the relativistic case can be derived using Lorentz transformations. Corresponding with figure 2.4, if S is the laboratory frame of reference and S' is a reference frame that moves along the y-direction with velocity βc (the speed of propagation of the electron along this axis.). The four-vector $p'_\mu = (\mathbf{p}', i\xi'/c)$ in inertial frame S' is found by performing a Lorentz-transformation of $p_\mu = (\mathbf{p}, i\xi/c)$, the momentum of the same electron measured from the rest-frame, S.

$$p'_x = p_x \quad (2.7(i))$$

$$p'_y = \gamma(p_y - \beta\xi/c) \quad (2.7(ii))$$

$$p'_z = p_z \quad (2.7(iii))$$

$$\xi'/c = \gamma(\xi/c - \beta\, p_y) \quad (2.7(iv))$$

Additionally, $\sum_\mu p_\mu\, p_\mu$ is Lorentz-invariant.

A photon with momentum $p_{photon} = \hbar\omega$, emitted in the *y*-*z* plane of *S* with an angular separation of θ with the *y*-axis (figure 2.4) is described by the four-vector $p_\mu = (0, p_{photon}\cos\theta, p_{photon}\sin\theta,\ i\hbar\omega/c)$. In the reference frame *S'* this four-vector is described by $p'_\mu = (0, p'_{photon}\cos\theta',\ p'_{photon}\sin\theta',\ i\hbar\omega'/c)$.

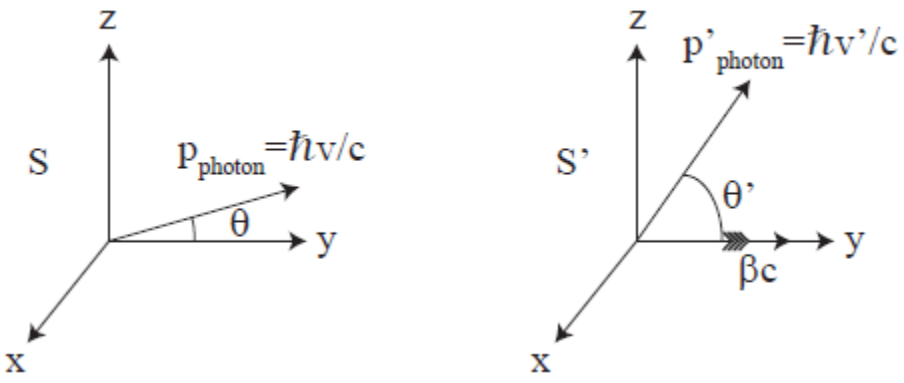

Fig 2.4: *Geometry of photon emission observed from two different reference frames. S; stationary reference frame and S'; frame moving with the forward direction of the electron from which the photon is emitted.*

The photon emission angle in the co-moving frame, θ' can be transformed to its equivalent in the laboratory frame:

$$\tan\theta = \frac{P_z}{P_y} = \frac{p'_{photon}\sin\theta'}{\gamma(p'_{photon}\cos\theta' + \beta p'_{photon})} = \frac{\sin\theta'}{\gamma(\cos\theta' + \beta)} \tag{2.8}$$

A photon emitted perpendicular to the direction of propagation of the electron (θ'=90) will be observed in the laboratory frame as being emitted by an angle:

$$\tan\theta \simeq \frac{1}{\gamma} \tag{2.9}$$

Where β is assumed to be unity for a highly relativistic electron. The opening angle Ψ of the forward emission cone of the radiation is given by:

$$\Psi = \frac{1}{\gamma} = \frac{\xi_0}{\xi} \tag{2.10}$$

Synchrotron radiation is thus highly collimated and incident on the sample with a very small spot size [1].

Undulators

Intense, wavelength-selected synchrotron radiation and its higher harmonics can be generated by an undulator (figure 2.5). In its basic form, an undulator comprises a series of permanent magnets with alternating upwards and downwards pointing dipole moments. As an electron

traverses the undulator, it experiences the Lorentz force and performs an oscillatory motion in the horizontal plane.

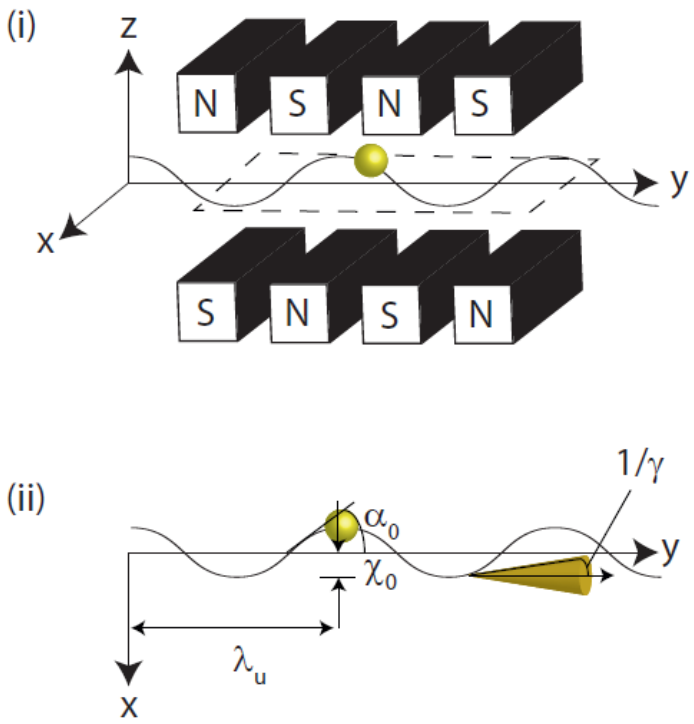

Fig 2.5: *(i) Trajectory of an electron through an undulator and (ii) top-down view of the system. The electron radiates in the direction of forward motion at each of the magnet poles* [1].

In the laboratory frame the electron moves with velocity βc along the *y*-axis. The undulator period when considered from this reference frame is λ_u. From the perspective of the relativistic electron, the period of the magnets is Lorentz contracted to λ_u/γ.

$$\lambda \simeq \lambda_u(1 - \beta \cos\theta) \tag{2.11}$$

Where θ is the angle of the emitted photon with respect to the *y*-axis. Expanding the cosine function to second order and substituting into 2.11 gives:

$$\lambda \simeq \lambda_u \left[1 - \left(1 - \frac{1}{2\gamma^2}\right)\left(1 - \frac{\theta^2}{2}\right)\right] \tag{2.12}$$

Neglecting the term of order $O(\theta^2/\gamma^2)$, the fundamental wavelength of the undulator radiation is given by:

$$\lambda \simeq \frac{\lambda_u}{2\gamma^2}(1 + \theta^2\gamma^2) \tag{2.13}$$

For photons emitted along the *y*-axis, θ=0° and $\lambda \simeq \frac{\lambda_u}{2\gamma^2}$. Radiation at this wavelength is strongly peaked due to the coherent superposition of wavefronts emitted at magnet poles being a single period λ_u apart.

The wavelength of a harmonic *m*, λ_m is determined by the number of undulator periods *N*. The relative bandwidth for the m^{th} harmonic is given by:

$$\frac{\Delta\lambda_m}{\lambda_m} = \frac{1}{mN} \tag{2.14}$$

As each wavelength comprising the bandwidth is relative to its angle off the axis defined by the electronic propagation, θ. The wavelength spread leads to an angular spread, $\Delta\theta$ in the emitted undulator radiation. The angle-dependent wavelength $\lambda_m(\Delta\theta)$ of the m^{th} harmonic is given by:

$$\lambda_m(\Delta\theta) = \lambda_m(0) + \frac{\lambda_u(\Delta\theta)^2}{2m} \tag{2.15}$$

Where:

$$\lambda_m(0) = \frac{\lambda_u}{2\gamma^2 m}\left(1 + \frac{1}{2}K^2\right) \tag{2.16}$$

And,

$$\Delta\lambda_m = \lambda_m(\Delta\theta) - \lambda_m(0) = \frac{\lambda_u(\Delta\theta)^2}{2m} \tag{2.17}$$

K is the deflection parameter, defined as, $K = \alpha_o\gamma$. This dimensionless parameter is the ratio of the orbital deflection angle to the half-angle of the radiation cone.

By combining 2.14 with 2.17, the angular width is given by:

$$\Delta\theta = \sqrt{\frac{2\lambda_m(0)}{L}} \tag{2.18}$$

Where $L = N\lambda_u$ is the total length of the undulator. Eq. 2.18 can be rewritten:

$$\Delta\theta = \frac{1}{\gamma}\sqrt{\frac{1 + K^2/2}{mN}} \tag{2.19}$$

The angular width of the cone is $\sim 1/(\gamma\sqrt{N})$ for small *K*. Much smaller than the vertical opening angle of the radiation cone from a bending magnet. The narrow cone of radiation emerging from an undulator can be shown to be rotationally symmetric. The total intensity of the light produced by the undulator scales with N^2. These properties make undulator radiation incomparably brilliant with the added advantage of being polarised [1].

Monochromators

A narrow band within the radiation spectrum centred on a specific wavelength can be selected by exploiting Bragg reflection from a single crystal or a periodic diffraction grating, consisting of a large number of parallel and closely spaced grooves on an optically flat surface. A schematic of a crystal monochromator is presented in figure 2.6 and inset, the geometry of Bragg diffraction from a periodic atomic lattice is described.

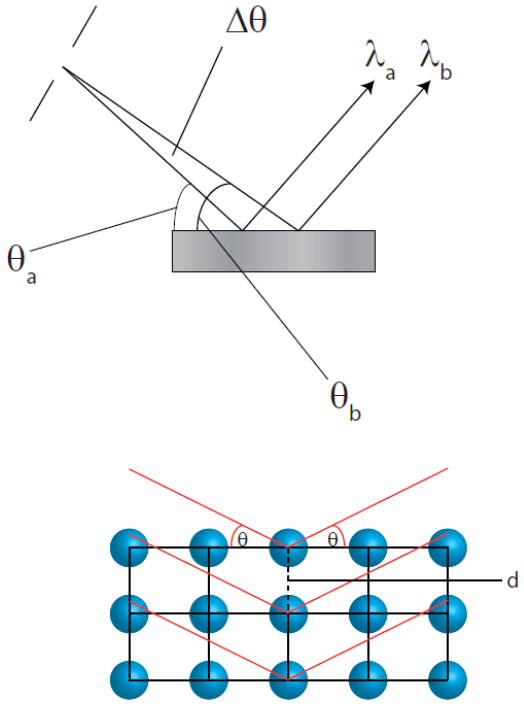

Fig 2.6: *Schematic of single crystal monochromator and Bragg diffraction geometry from a single crystal lattice.*

Bragg's law of diffraction for coherent scattering from a lattice is:

$$n\lambda = 2d \sin\theta \tag{2.20}$$

Where d represents the spacing between planes in the periodic lattice, λ is the wavelength of the incident light, θ is the angle that the incident beam makes with the surface and n is any positive integer. Rays with discrete wavelengths are Bragg reflected at distinct angles. Therefore, once brilliant light from the undulator encounters the monochromator, the grating

can be rotated to select the wavelength of the light that is reflected towards the sample. Synchrotron radiation is thus highly tunable [1].

2.2 Photoelectron and Auger Spectroscopies

Light, or electrons incident on solids, liquids or gases can result in the excitation of atoms to a resonant state or lead to ionisation via the emission of an electron. Ionisation of the inner shell of an atom creates core-hole quasi-bound states that overlap with the next higher charge state of the system. The primary ionisation event is often followed by expulsion (shake-off) or excitation (shake-up) of outer electrons. Both photoelectron spectroscopy (PES) and Auger electron spectroscopy (AES) centre on scattering processes where the initial state involves photons or electrons impacting on atomic, molecular or solid-state targets and the final state consisting of ejected photons, electrons or fragments that contain valuable information pertaining to the chemical composition and the nature of the bonding in the examined system [3].

Photoemission as a result of X-ray excitation was discovered by Hertz in 1887 during an experiment with the intention of the verification of the equations of Maxwell. Einstein characterised the photoelectric effect in 1905 [4] using the then novel laws of quantum mechanics. In 1925, Auger noticed two pairs of electronic tracks when observing an X-ray irradiated cloud chamber filled with an inert gas [5]. The tracks had an identical origin in space and the length of one was dependent on the energy of the incident X-rays while the length of the other on the material from which the trail arose. This was attributed to the dual ionisation of atoms by Auger and a theoretical explanation was provided by Wentzel in 1927 [6].

Wentzel proposed the two-step process; incident radiation with energy E_i, ionises the system in the inner shell. The energy of the inner-shell, *S*, relative to the vacuum level, is symbolised by E_S. The emitted electron travels with a kinetic energy:

$$E_P = E_i + E_S \tag{2.21}$$

The electron represents a constituent of the measured yield in photoelectron spectroscopy and also, the trail in Auger's cloud chamber whose length was dependent on the incident X-ray energy. The system can decay through a radiative or a non-radiative process in the aftermath. In the radiative process, which occurs if the energy of the X-rays acting on the material is greater than E_S, a photon of energy $\omega = E_R - E_S$ is emitted. In the non-radiative or *Auger* process (figure 2.7), an electron drops out of outer-shell *R* to fill inner-shell *S* and another electron is emitted from outer-shell *R'* with energy:

$$E_{AUGER} = E_R + E_{R'} - E_S \tag{2.22}$$

From the analysis of the energy, intensity and shape of peaks emergent in photoelectron spectra (Eq 2.21) and Auger electron spectra (Eq 2.22), the chemical species and the chemical bonds on a surface as well as significant information related to the electronic structure.

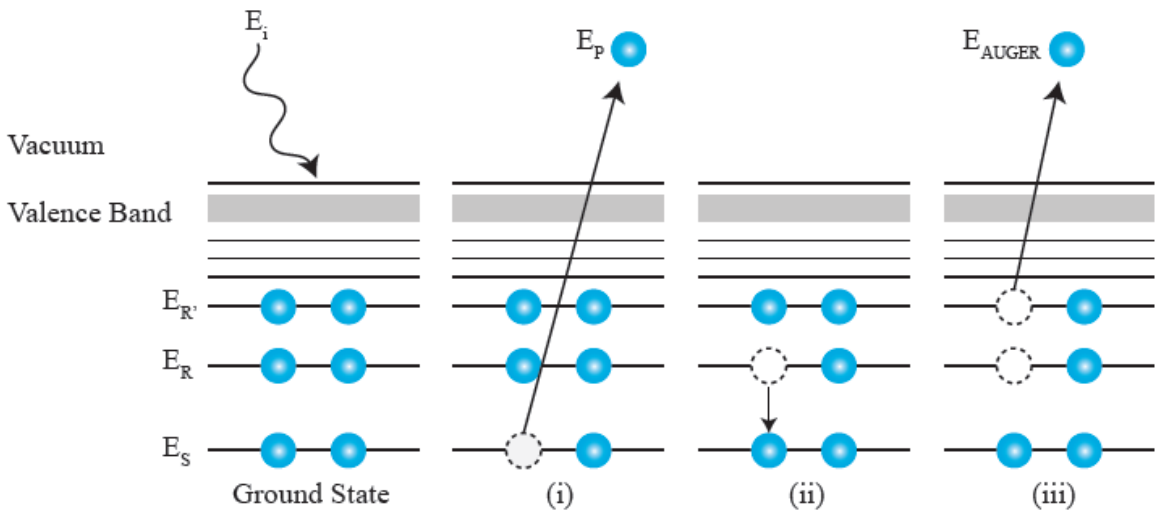

Fig 2.7: *Schematic of the Auger process; initially, photons or electrons of energy E_i irradiate an atom in the ground state and in response, a core electron is emitted (i) from E_S. Subsequently, the core-hole is filled via an electron moving from energy level E_R to E_S (ii) and then to stabilise the system, an Auger electron is emitted (iii).*

2.3 Low Energy Electron Diffraction (LEED)

Davisson and Gerner conducted the first LEED experiment in April of 1925 following an accident while investigating the angular distribution of electron scattering by a nickel sample. The sample became heavily oxidised and was subsequently reduced and abnormally sharp maxima were observed in the intensity distribution [7]. Davisson and Gerner realised that these maxima represented an interference pattern, the reduction of the nickel sample had produced repeating crystalline patterns. This served as experimental verification of the wave nature of electron, postulated by De Broglie in 1923. De Broglie proposed that electrons have wavelengths that are proportional to their momentum [8], $m_e v$:

$$\lambda_e = \frac{h}{m_e v} \tag{2.23}$$

Where *h* is Planck's constant. An electron propagating with an energy of the order of 100 eV have wavelengths that are comparable to typical interatomic distances in solid-state materials. Moreover, electrons of such energies have small mean free paths in solids and report only information regarding the topmost layers to the detector. Low energy electron diffraction data can deliver information about the structures of ordered, crystalline solids.

Multiple scattering plays a role in the diffraction of electrons from solid surfaces and often time consuming computational analysis, requiring full quantum mechanical scattering calculations, is needed. While the detailed analysis of low energy electron diffraction to elucidate the surface structure is complicated and arduous, the basic physical principles of the experiment are very simple. A collimated mono-energetic beam of electrons is directed towards a single-crystal sample surface and the resulting diffraction pattern of elastically back-scattered electrons is recorded using a position-sensitive detector. The angular intensity distribution due to the interference of back-scattered electrons from a periodic atomic surface is described by Bragg's law [9].

Figure 2.8 shows schematically, the "rear view" LEED setup which is the most commonly utilised configuration. Electrons are emitted and accelerated through potential V_0, by the electron gun from behind the hemispherical LEED optics. The sample sits at the centre of the hemisphere so that all back-diffracted electrons travel towards the screen on radial trajectories.

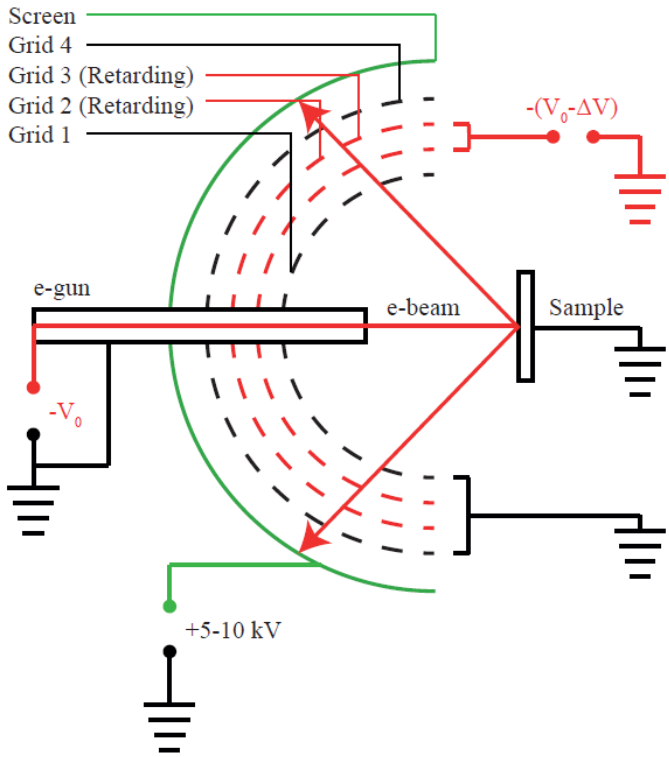

Fig 2.8: *Schematic of typical LEED instrument.*

En-route to the screen the electrons encounter the retarding field energy analyser (RFA). The RFA is comprised of three or four hemispherical grids that are concentric with the screen. Grid 1 (nearest of the grids to the sample) is grounded in order to provide a field-free region between the sample and the grid. Grid 2 and grid 3 are the suppressor grids (In a three grid RFA, this is just one grid.) and a negative potential $-(V_0-\Delta V)$ is applied to them in order to repel electrons that have backscattered in an energetically inelastic manner from the sample and have lost $>\Delta V$ of their original kinetic energy. This results in only elastically scattered electrons and those suffering only a small reduction in kinetic energy reaching the screen, ensuring that the image on the screen is accurately representative of the atomic lattice. The final grid (nearest of the grids to the screen) is also grounded to minimise the interference of the large potential applied to the screen with the RFA. The screen is held at a high potential (of the order of kilovolts) to

provide the back-scattered electrons with enough energy to leave a significant visible signature on the fluorescent screen [10].

Due to the small penetration depth of low energy electrons, the diffraction pattern arises from a small number of the sample's outer layers. The relevant scattering sites are therefore only periodic in the two dimensions parallel to the surface. The surface lattice can be described by two vectors $\mathbf{a_1}$ and $\mathbf{a_2}$.

$$R = m_1 a_1 + m_2 a_2 \tag{2.24}$$

With integer numbers m_1 and m_2. Figure 2.9 shows schematic representations of common square, rectangular and hexagonal atomic arrays occurring at solid surfaces and their corresponding lattice vectors.

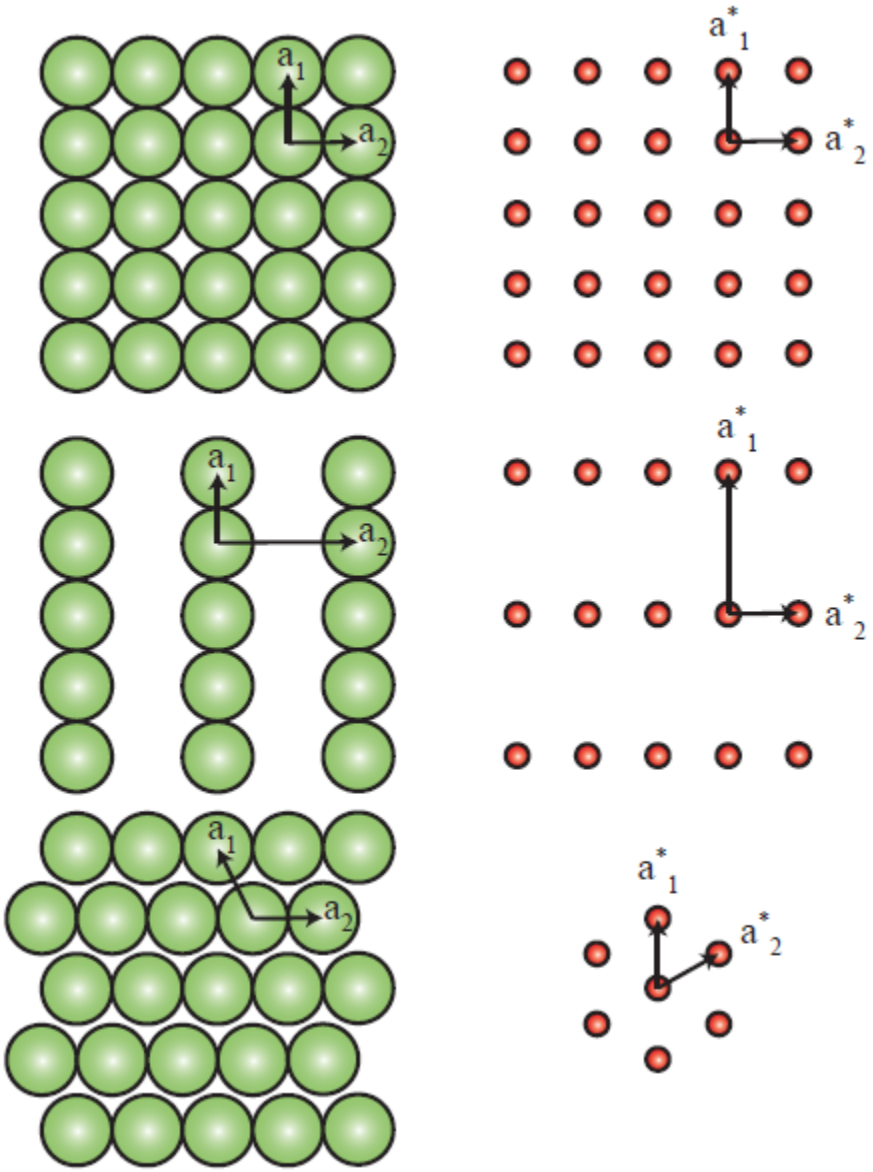

Fig 2.9: *Left: arrangements of atoms in the (100) (square), (110) (rectangular) and (111) (hexagonal) surfaces of a simple face centred cubic crystal lattice and their associated lattice vectors. Right: Corresponding reciprocal lattices and their lattice vectors.*

The key to the surface specificity of LEED is the large interaction cross-section of low energy electrons. It is this intrinsic property of low energy electrons that makes detailed structural characterisation of surfaces computationally complicated because multiple scattering events are common. The scattering potential relevant to LEED is non-local and should include

electrostatic contributions from all atomic nuclei and electrons, exchange-correlation effects and be self-consistent. Such calculations are computationally inefficient and thus, the potential used in LEED calculations that are written in to computer code is simplified by employing a local approximation within the "muffin-tin" model [11]. The muffin-tin model is represented schematically in fig 2.10, below. The potential is divided into two distinct regions; within non-overlapping spheres centred on atomic sites representing ion cores which are responsible for the electron scattering and a constant value is ascribed to the regions in-between.

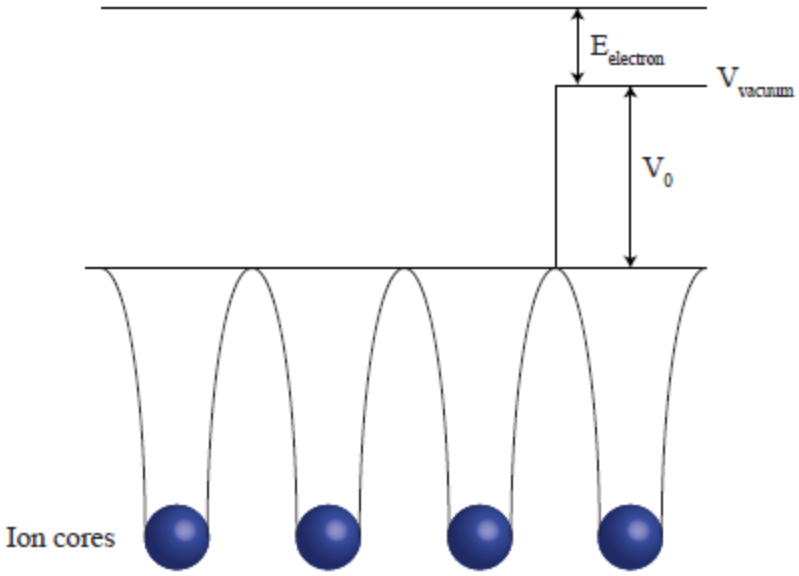

Fig 2.10: *Schematic depicting the muffin tin potential of a repeating crystalline structure running from left to right. Ion cores are encased in a spherically symmetrical potential and adjacent cores do not overlap. The potential is set as constant to simplify LEED analysis. And electron of energy $E_{electron}$ relative to the vacuum level will gain energy equal to V_0 as it crosses the surface/ vacuum interface.*

The scattering factor,f, represents the scattering power of an individual atom. In the case of low-energy electrons, the scattering factor is complex and causes each scattered wave to be

phase shifted relative to the incident wave. An incident electron can go through multiple scattering events, each event introducing a phase shift. The scattering factor in LEED is typically written as a partial wave of the form [12,13]:

$$f(\theta) = \frac{1}{2ik}\sum_{l=0}(2l+1)|\exp(2i\delta_l) - 1|P_l(\cos(\theta)) \tag{2.25}$$

Where, k is the magnitude of the electron wave vector, l is angular momentum, δ_l is the scattering phase shift and P_l are Legendre polynomials. Phase shifts are specific to the atomic species of the scatterer and the electron wavevector and must be considered when performing structural analysis. Radial solutions of the Shrödinger equation, inside and outside of the ion core are used to calculate the phase shifts resulting from individual atomic species comprising a material. The logarithmic derivatives on either side of the spherical muffin-tin boundary, r_{mt} [14,15] are equated. If the solution inside the muffin-tin is $R_l(r_m)$ and $L_l = \frac{R_l'(r_m)}{R_l(r_m)}$, the phase shifts satisfy:

$$\exp(2i\delta_l) = \frac{L_l h_{l1}(kr_{mt}) - h_{l2}(kr_{mt})}{h_{l1}'(kr_{mt}) - L_l h_{l1}(kr_{mt})} \tag{2.26}$$

Where h_{l1} and h_{l2} are spherical Hankel functions of the first and second kind. Inelastic scattering and electron absorption can be accounted for by introducing an imaginary component to the muffin-tin potential without changing equations 2.25 and 2.26, except that k becomes complex. The outgoing wave in this scenario is damped by the amount $\exp(-2Im\delta_t)$.

Atomic vibrations similarly affect the overall diffracted beam intensity and are quantified through the Debye-Waller factor, $\exp(-2M)$ where:

$$M = |Q|^2\langle(\Delta r)^2\rangle \tag{2.27}$$

Δr represents the extent of atomic deviation and $|Q|^2$ is the 3D momentum transfer of the examined diffraction beam.

As mentioned previously, LEED I-V analysis is complicated by multiple scattering interactions. As a result computational programs used for structural analysis based on LEED data undertake an iterative trial and error approach. Theoretical I-V curves are generated for a proposed structure and compared with experimental curves. The quality of the agreement between theory and experiment is determined by a reliability factor (R-factor). On the basis of the R-factor(s), a new structure is developed by the program. This process is carried out until the best possible R-factor is obtained. Two software packages were employed in this study. Firstly, phase shifts were generated using the van Hove/ Barbieri phase shift package and secondly, the main LEED I-V calculations were carried out using *CLEED* [15]. The R-factor of Pendry [16] is used in this case (eq 2.28(i)), for each beam, g over the energy range, E_i:

$$R_P = \sum_{g,i}(Y_{cal} - Y_{exp})^2 / \sum_{g,i}(Y_{cal}^2 + Y_{exp}^2) \tag{2.28(i)}$$

Where:

$$Y = L/[1 + (LV_{0i})^2] \quad (2.28(ii))$$

Where:

$$L = (\frac{\partial I}{\partial E})/I \quad (2.28(iii))$$

And V_{oi} is the imaginary part of the inner potential. The van Hove/ Barbieri phase shift package can calculate phase shifts for any structure that are experienced by an electron in the energy range 0-300 eV and for $l = 0, \dots, n$. Initially, a free-atom calculation using the self-consistent, relativistic Dirac-Fock equation is carried out to generate a radial charge density for each of the *N* atoms in the structure being simulated. Then, a muffin-tin potential is computed for the 3 dimensional bulk structure [17]. In this step the atomic charge densities of the elements comprising the structure under examination are superimposed and the muffin-tin zero is determined. In the final stage, phase shifts are determined using the relativistic Dirac equation.

CLEED consists of three individual programs that work together to perform LEED I-V analysis. These programs are based around routines developed by Van Hove and Tong [13,14]. The program *Nsym* inputs a trial structure and returns simulated I-V curves. The program *Crfac*, calculates the Pendry [16] R-factor between the simulated and experimental curves. The r-factor can take a value between 0 and 1. The value 0 represents a perfect correlation between theory and experiment whereas the value 1 represents the opposite of this. Furthermore, the Pendry R-factor is predominantly sensitive to the positions of peaks. When *Crfac* calculates the r-factor, it rigidly shifts the calculated curves within a ±10 eV range. This is because real component of the muffin-tin potential increases the energy of the incident electrons by an

amount it crosses the vacuum-surface interface that is rarely known *a priori*. To account for the large uncertainty, the *Crfac* program shifts the calculated I-V curves within this range to reach a minimum R-factor. The third program, *Search*, compares the relative R-factors of various trial structures and proposes a new trial structure to try and minimise the R-factor [18].

To perform a full structural calculation, *CLEED* requires input files describing the relative positions of atoms in the bulk structure and in the surface structure as well as their associated phase shifts, calculated by the van Hove/ Barbieri phase shift package. Additionally, an input file relating each simulated LEED spot to its experimental equivalent is required. The positions of the atoms in the input file describing the surface are changed by *Search* before this trial structure is compared with the experimental curves. The positions of atoms in the bulk structure are not adjusted by *Search*.

2.4 Near-edge X-ray Absorption Spectroscopy (NEXAFS)

Near-edge X-ray absorption spectroscopy (NEXAFS) probes the absorption of electromagnetic radiation via the excitation of core electrons to unoccupied bound or continuum states. When a material is irradiated with monochromatic X-rays, the energies of which are varied around an absorption edge, distinct features appear in the absorption spectrum. In the soft X-ray range (<2000eV), photo-absorption is a common phenomenon and results in a core hole following the emission of a photoelectron, the filling of which results in either the emission of a fluorescent photon or an Auger electron. Both emitted particles carry information about the

initial core hole and are hence representative of the absorption cross section. For the endeavour of surface sensitive studies, it is prudent to undertake the collection of electrons rather than fluorescent photons because of the relatively low kinetic energy of electrons and their corresponding small mean free path through materials [19].

The NEXAFS spectrum is a plot of the photo-absorption cross section as a function of incident photon energy near the absorption edge of a given molecule. Generally, the absorption cross section resembles a step function. This step function results from the excitation of a core electron to a continuum or quasi-continuum of final states. The origin of features in a typical NEXAFS spectrum are shown schematically in fig 2.11.

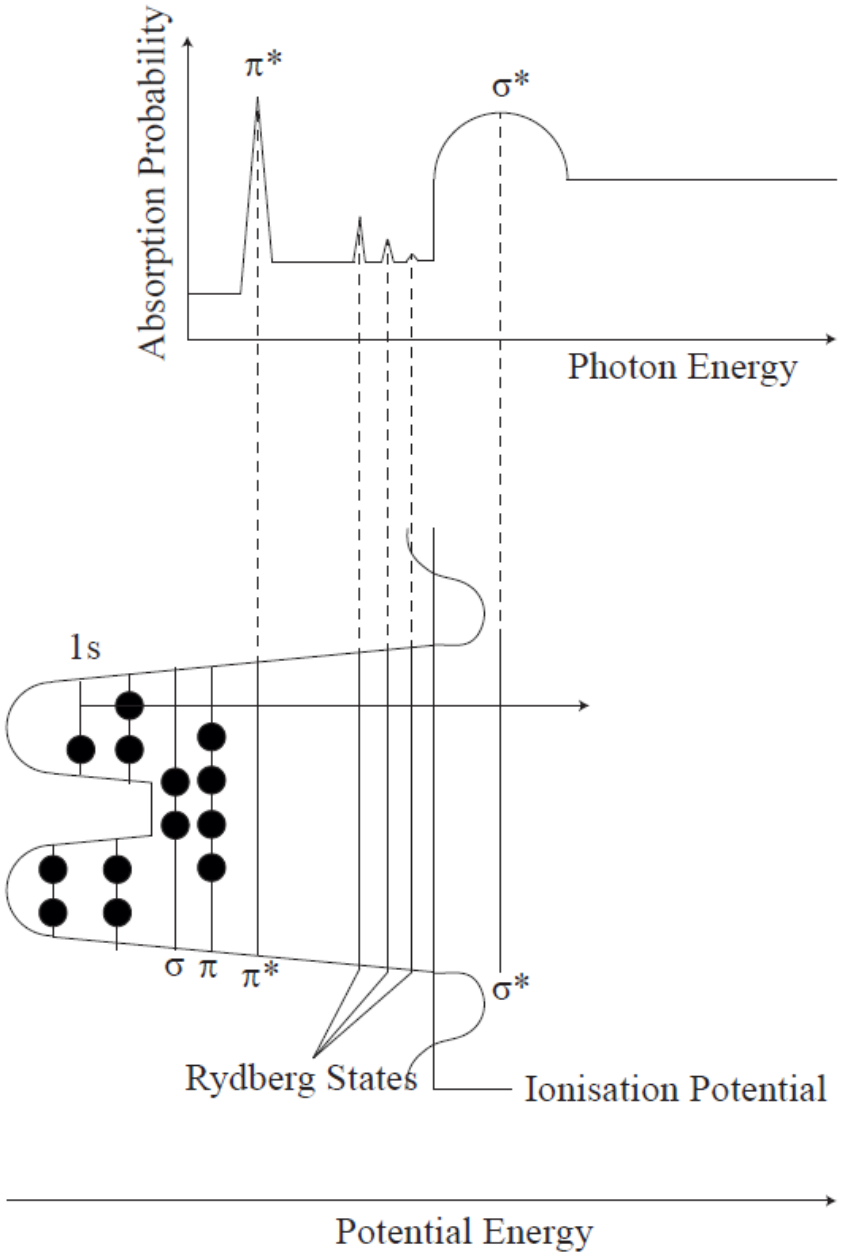

Fig 2.11: *Schematic of potential (bottom) and corresponding NEXAFS features arising from diatomic molecular group* [20].

In the region of the ionisation threshold, resonances appear on step-like features when the incident energy matches the difference in energy between the initial state of the core electron and an unoccupied anti-bonding molecular state (given symmetry dependent label π* or σ*). It is typical that the energetically lowest unoccupied molecular orbital formed with a π-bond is

the π*-orbital, with σ*-orbitals usually found above the vacuum level. The π* resonance (or the 1s → π* transmission yield) arises only when π-bonding (a double or triple bond) is present.

The width of the resonances arising from transmission of a core electron to a π- or σ- anti-bonding molecular orbital is determined by the resolution of the technology (producing a Gaussian line-shape), the lifetime of the excited state (producing a Lorentzian line-shape) and by the vibrational motion of the molecule, which results in non-symmetrical broadening of the resonance. The lifetime of a π*-resonance is determined by the decay of a core hole and thus π* peaks tend to be relatively narrow. Broader resonances occur where core electrons are excited to σ-anti-bonding orbitals. As a consequence of an overlap of these states with continuum states, there is an increased probability of electron decay to the continuum.

Rydberg orbitals are observed normally between the π*-resonance and the ionisation potential. In the condensed phase or when probing strongly chemisorbed molecules, Rydberg resonances are smeared out because of the large spatial extent of the molecules which have most of their orbital density at their periphery. Multi-electron features, such as ‘shake-up’ structures can also appear in NEXAFS spectra. Additional to information regarding the electronic structure, the spatial orientation of an individual molecular orbital and the molecule to which they belong defined by a polar and azimuthal angular separation relative to an appropriate origin, can be determined. For this purpose, polarisable synchrotron radiation is employed. Synchrotron radiation from a bending magnet is close to perfectly linearly polarised in the direction of the storage ring.

A quantum mechanical interpretation of the excitation of a single electron in the dipole approximation, referred to as Fermi's golden rule, relates the initial electronic state, Ψ_i and the final electronic state, Ψ_f to the absorption cross-section, σ_x:

$$\sigma_x \propto |< \Psi_i | e.p | \Psi_f > | \rho_f(E) \tag{2.29}$$

Where e is the unit electric field vector, p is the dipole transition operator and $\rho_f(E)$ is the density of final states.

Chemical bonds and their associated orbitals have distinct directional vectors that correspond with the maximum orbital amplitude of the excited atom. Therefore, the total transmission yield observed in NEXAFS measurements is dependent on the relative orientation of the electric vector and the examined orbital. σ*-orbitals are directed along the physical bond direction, while π*-orbitals are always normal to the bond direction.

For the excitation of a 1s initial electronic state by a linearly polarised beam of electromagnetic radiation to a final state orbital $\boldsymbol{O}$ with associated directional matrix element $< \Psi_f | p | \Psi_{1s} >$. The 1s → $\boldsymbol{O}$ transition intensity is then:

$$I \propto \left| e < \Psi_f \right| p | \Psi_{1s} > |^2 \propto |eO|^2 \propto \cos^2 \delta \tag{2.30}$$

Where δ is the angle between the electric vector associated with the incident X-ray beam, $\boldsymbol{E}$, and the direction of the final state orbital, $\boldsymbol{O}$. Thus, the maximum total transition intensity occurs when the direction of the electric vector of the incident beam is parallel to the direction of the examined unfilled anti-bonding orbital and the minimum occurs when they are orthogonal. To extract quantitative information about the bonding orientation, spectra must be recorded at different angles of incidence and then normalised to the pre-edge region and the absorption step-edge.

Stohr and Outka developed techniques to determine the orientation of molecules adsorbed to surfaces based on the angular dependence of the recorded intensity of 1s transitions to unfilled σ* and π* molecular-orbital final states. Molecules have two separate classifications, depending on whether the final state orbital is specifically directed (the 'vector' case) or if energetically degenerate orbitals span a plane (the 'plane' case). The schematics in figure 2.12 show the relative spatial orientations of σ *- and π*-orbitals in single, double and triple molecular bonds.

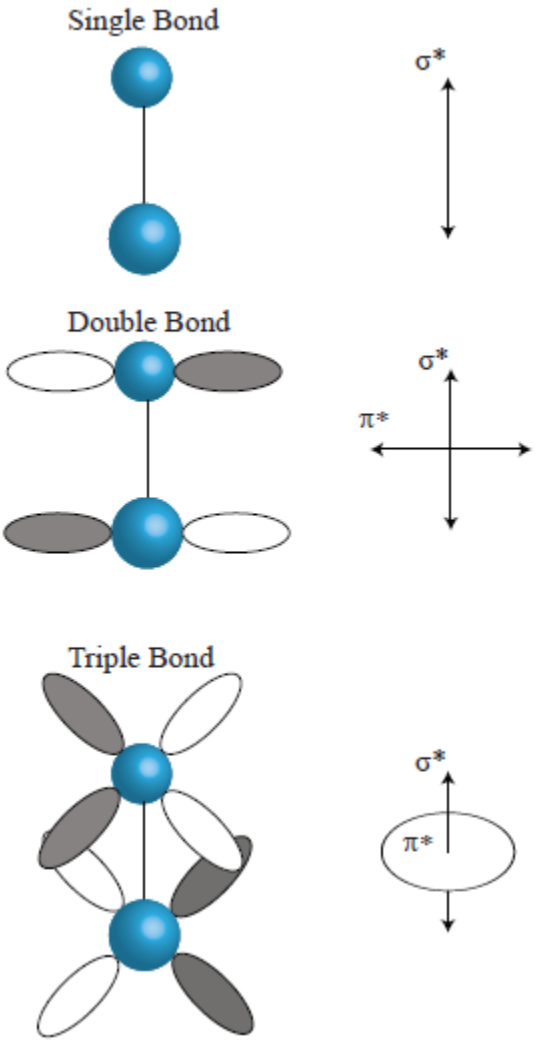

Fig 2.12: *Schematic representation of the spatial orientation of σ*- and π*- orbitals corresponding to single, double or triple covalent bonds. Molecules are classed as vector-type, where the orbitals are specifically orientated or plane-type, where degenerate orbitals form a plane* [19].

A schematic diagram describing a linearly polarised incident beam interacting with a vector orbital, ***O*** is presented in figure 2.13. The direction of the orbital is defined by two angles; the tilt of the molecule, α, is the polar angular separation away from the direction normal to the sample surface, ***n*** and the twist angle is the azimuthal angle out of the direction of propagation of the incident beam, ϕ.

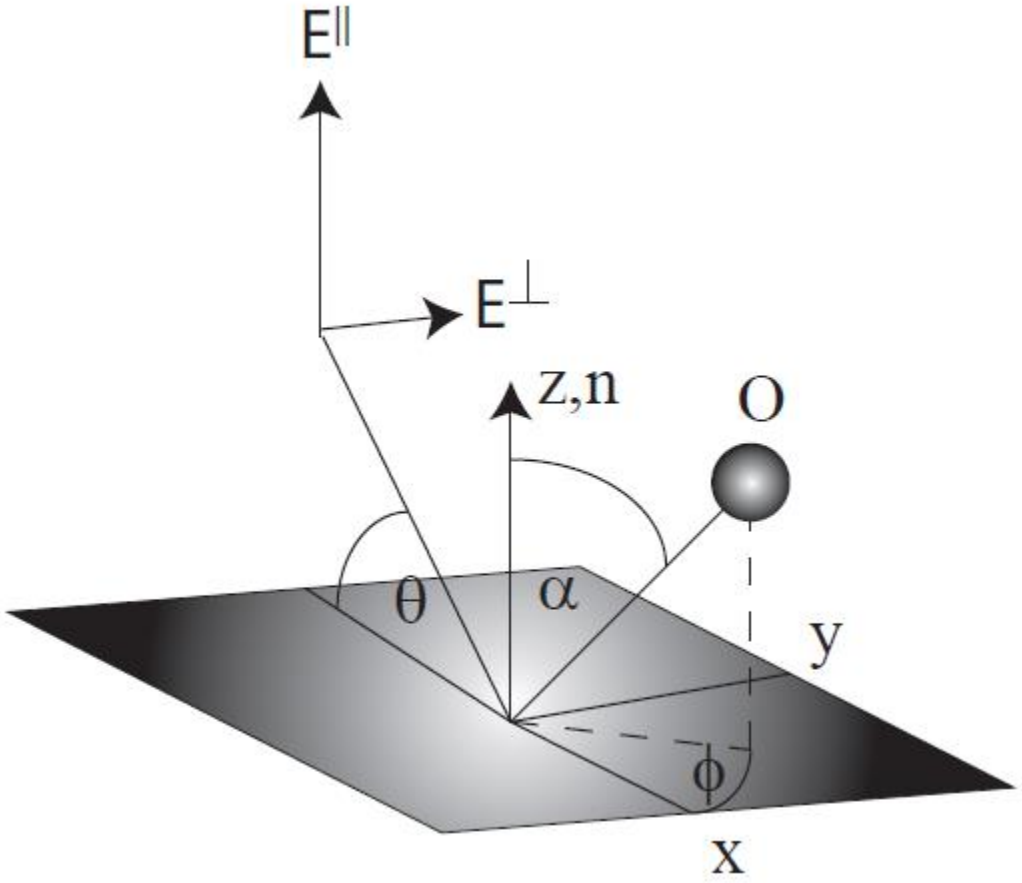

Fig 2.13: *Coordinate system describing the geometry of a molecular orbital relative to a substrate surface. The orientation of the vector orbital,* ***O****, is characterised by a polar angle, α and an azimuthal angle, ϕ. The beam is incident in the (x,z) orbit plane of the storage ring which contains the major electric field vector component* $E^{\parallel}$ *that is incident on the surface at angle θ. The weaker component is incident along the y axis on the surface plane. The surface normal* ***n*** *is the z-direction which is also the axis of azimuthal rotation of the sample.*

The chosen coordinate system in figure 2.13, above, is the coordinate system (x,y,z) of the incident radiation. The X-rays are incident on the sample in the (x,z) plane which is parallel to the storage ring. The majority component $E^{\parallel}$ of the electric field vector E of the synchrotron beam lies in this plane and it is tilted out of the surface normal by θ due to the angle of incidence of the beam. The minority component, $E^{\perp}$ is incident along the y-axis [19].

The total transition intensity is given by the following equation:

$$I = C[PI^{\parallel} + (1 - P)I^{\perp}] \tag{2.31}$$

Where P is the polarisation factor, which describes the proportion of the incident light which is contained in the major component and it is defined as:

$$P = \frac{|E^{\parallel}|^2}{|E^{\parallel}|^2 + |E^{\perp}|^2} \tag{2.32}$$

And $I^{\parallel}$ and $I^{\perp}$ are the measured intensity component corresponding to illumination by $E^{\parallel}$ and $E^{\perp}$. For the vector case, $I^{\parallel}$ is:

$$I_V^{\parallel} = A(\cos^2\theta\cos^2\alpha + \sin^2\theta\sin^2\alpha\cos^2\phi + 2\sin^2\alpha\cos^2\alpha\sin^2\theta\cos^2\theta\cos^2\phi) \tag{2.33(i)}$$

And $I^{\perp}$:

$$I = A\sin^2\alpha\sin^2\phi \tag{2.33(ii)}$$

Where A and C are arbitrary constants. The geometry of the plane case is not shown as it is similar to the vector case with the exception that the polar angular displacement is initially

defined as the angle between the vector normal to the surface and the vector normal to the plane formed by the energetically degenerate orbitals. For the plane case $I^{\parallel}$ is described by:

$$I_P^{\parallel} = B(1 - \cos^2\theta\cos^2\gamma - \sin^2\theta\sin^2\gamma\cos^2\phi - 2\sin\gamma\cos\gamma\sin\theta\cos\theta\cos\phi) \quad (2.34(i))$$

And $I^{\perp}$ by:

$$I_P^{\perp} = B(1 - \sin^2\gamma\sin^2\phi) \quad (2.34(ii))$$

The symmetry of the substrate to which the examined molecules are adsorbed can eliminate some of the azimuthal dependence because the surface symmetry develops equivalent adsorbate domains. For example, for a molecule adsorbed to a substrate with twofold symmetry, such as the TiO_2(110) substrate, one set of molecular coordinates (α,ϕ) or (γ,ϕ) will have an equivalent which represents a 180° rotation. For twofold or higher substrate symmetry, the term containing $\cos\phi$ is averaged out and the individual intensity components in the vector case are given by:

$$I_V^{\parallel} = A(\cos^2\theta\cos^2\alpha + \sin^2\theta\sin^2\alpha\cos^2\phi) \quad (2.35(i))$$

And,

$$I_V^{\perp} = A\sin^2\alpha\sin^2\phi \quad (2.35(ii))$$

And in the plane case:

$$I_P^{\parallel} = B(1 - \cos^2\theta\cos^2\alpha - \sin^2\theta\sin^2\alpha\cos^2\phi) \quad (2.36(i))$$

And,

$$I_P^{\perp} = \mathrm{B}(1 - \sin^2\alpha\sin^2\phi) \quad (2.36(ii))$$

For a substrate with threefold or higher symmetry, the $\cos^2\phi$ term averages to ½. For the vector case:

$$I_V^{\parallel} = A(\cos^2\theta\cos^2\alpha + \tfrac{1}{2}\sin^2\theta\sin^2\alpha) \quad (2.37(i))$$

And,

$$I_V^{\perp} = \frac{A}{2}\sin^2\alpha \quad (2.37(ii))$$

And for the plane case:

$$I_P^{\parallel} = B(1 - \cos^2\theta\cos^2\alpha - \tfrac{1}{2}\sin^2\theta\sin^2\alpha) \quad (2.38(i))$$

And,

$$I_P^{\perp} = \frac{\mathrm{B}}{2}(1 + \sin^2 \alpha) \qquad (2.38(ii))$$

2.5 X-ray Photoelectron Emission Microscopy (XPEEM)

In the early 1930s, Brüche showed that the surface of a heated planar electron-emitting cathode could be imaged in an electrostatic two aperture lens system. He subsequently demonstrated, using a simple magnetic lens, that electrons excited from a sample by a UV radiation source and accelerated to high energy could be utilised for imaging. PEEM was not broadly employed until the 1980s, alongside the development of the emerging field of surface science and various breakthroughs in various associated fields such as the development of ultra-high vacuum, the technological advancement of its constituent devices and the advancement of synchrotron technology [21].

Presently, XPEEM devices at synchrotrons exploit brilliant, energy-tuneable radiation. XPEEM is a powerful tool for real-space chemical mapping and as a chemical-spectro-microscope has found application in the study of metals, semiconductors, magnetic films, polymers and biomaterials [22-30]. Specific to the field of surface science, the spatial chemical sensitivity of the instrument can be used to map the evolution of nanoparticle/ thin film growth in-situ [31].

The operation modes of photoelectron microscopes are distinguished by their illuminating photon source and the collection mode of the photoelectrons. Using low energy photons such as those from an Hg lamp, PEEM without true spectroscopic capabilities (i.e. over a small energy window) can be carried out. Secondary electrons arising almost entirely from indirect scattering of Auger electrons dominate the photocurrent in this case. The size of the photo-electron yield (and thus the extent of the 'brightness' observed in an XPEEM image) is connected with the bulk properties of a material which influence the excitation probability and mean free path of excited electrons and the work function. In PEEM images of composite materials then, contrast is observed between chemically or structurally different materials with the same work function, or chemically or structurally different materials with different work functions or surface terminations of single material with different work functions. As well as spatial-chemical identification of materials or domains, catalytic reactions can be observed in-situ by exploiting the change in the work function induced by an adsorbate. While the non-spectroscopic mode is the most technologically straight-forward, the information available is limited, particularly regarding multi-component systems (i.e. with various reaction steps or substrates). For a more in-depth understanding of complicated chemical systems then, it is prudent to employ higher photon energies to induce element specific photoemission [32].

Using X-rays, chemically sensitive XPEEM can work in XAS or XPS mode. XAS mode requires a tuneable synchrotron source, but not an energy filter. For a given material, when the energy of the incident photons is below the threshold of core electron emission, photoemission does not occur and this translates to a dark area on the XPEEM screen. When the energy of the X-rays is higher than that of the core level of the material on which they are incident, core level emission occurs along with an increased yield of secondary electrons (via secondary processes) and this corresponds to a bright area on the XPEEM screen. The total electron yield (TEY) is

determined by the element specific adsorption coefficient and consequently by tuning the photon energy to the appropriate value materials can be chemically identified, spatially. In XPS mode, a constant incident energy is utilised while the resultant photoelectrons are energy filtered to match the core level of interest [33].

In XAS imaging mode, an X-ray beam is incident at a grazing angle across the sample (~15°, typically due to the short optimum working distance between the sample and the objective lens that is required, as with an optical microscope.), the objective lens creates a diffraction pattern in its back focal plane (BFP) which is then imaged by the transfer lens (TL) in to the field lens (FL). These lenses work in conjunction to form a second intermediate image antecedent to the intermediate lens (IL). This lens images this information through an aperture with a limited angular acceptance (FPI) to reduce aberrations into lens P1 and on to the entrance plane EP2, (located in the retarding lens (RL)) of a 180° energy analyser. The analyser retards the electrons to 5% of their original energy before their reacceleration to their initial energy via the acceleration lens (AL) to their original energy. The lenses comprising the analyser section (L1, HP, L2, AL) image the electrons on to the dispersive plane of the analyser (DP). The electrons then pass through an energy-selection aperture on to the imaging plane (IP). This image is then magnified by the projector optics onto the image detecting device [34]. It is XAS mode only that is utilised in the studies carried out in later chapters (fig 2.14).

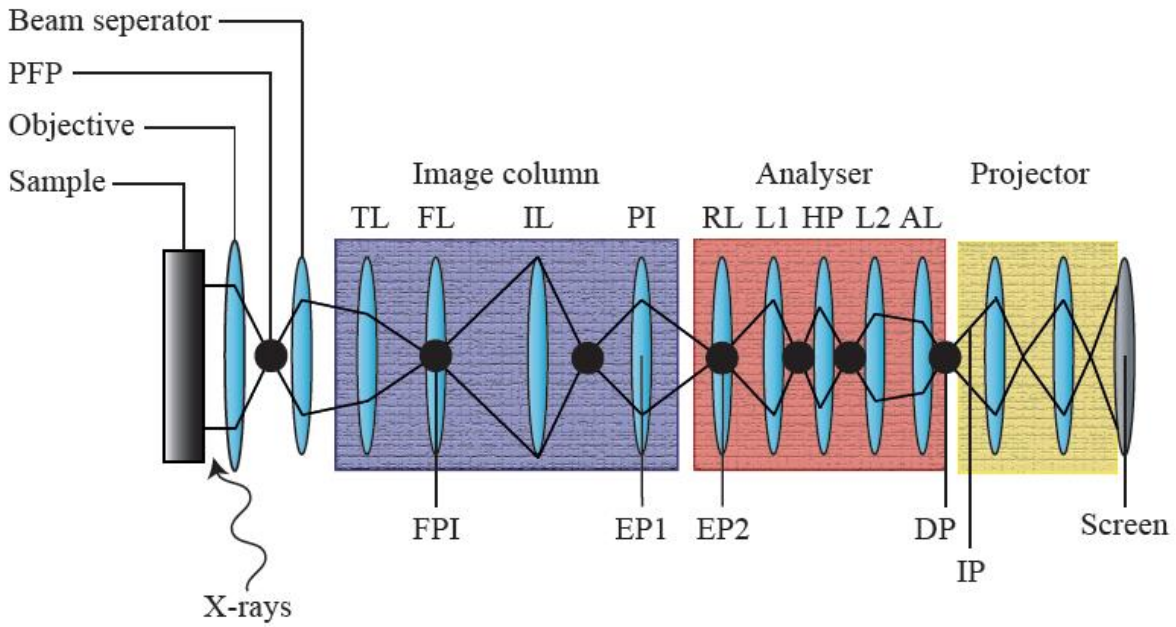

Fig 2.14: *Schematic of electron beam propagation through PEEM microscope with optical configuration for XPEEM mode* [34].

The general case for current PEEM experiments is that low-energy UV to soft X-ray photons are used as the light source. Photons of this energy generate low energy photoelectrons (20-300 eV is typical) which means that the information recorded is surface specific. The surface sensitivity can be augmented by employing a retarding field prior to the photoelectrons encountering the electron analyser, this is partial electron yield (PEY) mode. By filtering out electrons with the lowest kinetic energies, information arising from the outermost layers of the system only are gathered. When studying adsorbates on surfaces, the signal to background ratio acquired via PEY mode is superior to that corresponding to total electron yield (TEY) mode. Auger electron yield (AEY) mode, where inelastic Auger electrons are collected requires an electron energy analyser but has superior surface sensitivity to even PEY mode [33].

XPEEM operating in XAS or XPS mode, can also be used to obtain μXAS or μXPS data. Each pixel of an XPEEM image contains spatially resolved spectroscopy data and by extracting this data from the same area of a series of XPEEM images, XAS or XPS spectra can be synthesised from micro-areas of a surface, this allows spectroscopy to be carried out specifically on nanostructures.

2.6 Low Energy Electron Microscopy (LEEM)

Around half a century ago, available UHV technology reached a stage of advancement that facilitated the technological development of electron microscopy. The project to develop a machine that could image surfaces using slow reflected electrons was begun in the Michelson laboratory in California in 1962 [34] by Bauer's group but not developed fully until the mid-eighties [35].

LEEM is a type of cathode lens microscopy, which means that it belongs to that group of microscopes that utilises the sample as a cathode element. Electrons generated from an electron gun are directed towards the optical trajectory of the objective lens. The incident and back-scattered electrons pass simultaneously through the objective lens, which acts on them together, in opposite directions (figure 2.15). The incident beam is focused to a plane wave or parallel beam by the objective lens, while also decelerated to the low energy region. The impact energy of the incident electrons is dependent on the variable voltage between the sample and the cathode contained in the electron gun. The reflected electrons are accelerated and focused by the objective lens. The periodic uniformity of a crystalline plane confines reflection to Bragg angles and electrons emitted at the same angle interfere constructively. The beam splitter

deflects the backscattered electrons towards the imaging column where the image in the back-focal-plane is reproduced by a secondary diffraction plane at the front of the column. An image is formed by a contrast aperture in the secondary diffraction plane and the imaging column optics facilitate the magnification of this image onto a multi-channel plate or phosphor screen. The LEED pattern from the sample can be viewed by removing the contrast aperture [36].

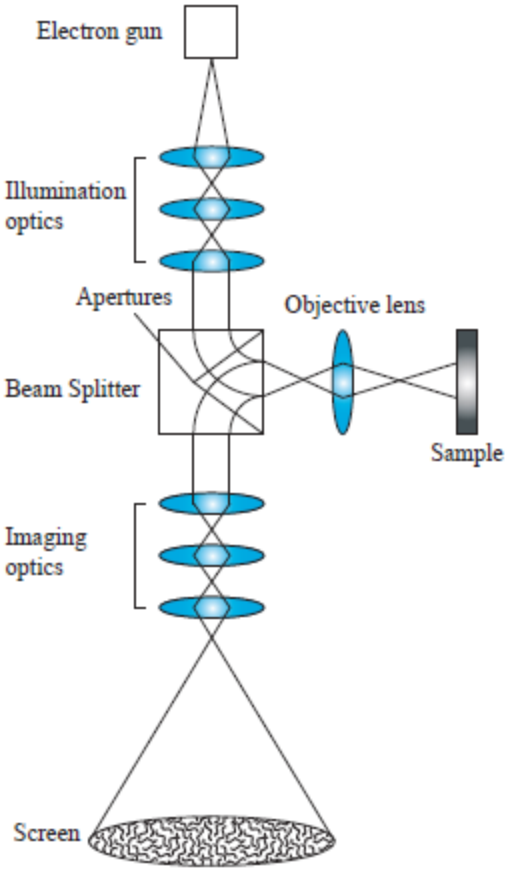

Fig 2.15: *Schematic of conventional LEEM system.*

The low impact energy of electrons incident in the LEEM experiment mean that individual atomic layers can be resolved with high contrast and minimal radiation damage. The surface sensitivity of the technique combined with the non-scanning nature of the data acquisition (i.e each pixel of the image is generated simultaneously) means that LEEM has found application

in in-situ studies of thin-film growth, structure and dynamic processes [37-41]. LEEM images can identify surface features by displaying contrast at atomic steps and between materials with different reflection coefficients. Conventional LEEM instrumentation can resolve surface features down to a few nanometres. The resolution is mainly limited by chromatic aberrations that arise from the energy dependence of the objective lens [36]. Technology based theoretical and practical studies carried out with the intention of improving the resolution of LEEM are focused on the design of the objective lens [36,41] or the addition of further lenses [42].

References

[1] H. Wiedemann, *Synchrotron Radiation 1st Ed.* (2003) Springer.

[2] www.Diamond.ac.uk.

[3] S. Taioli, S. Simonucci, L. Calliari and M. Dapor, *Physics Reports*, **493** (2010) 237.

[4] A. Einstein, *Annalen der Physik,* **17** (1905) 132.

[5] P. Auger, P. Ehrenfest, R. Maze, J. Daudin and R.A. Frèon, *Reviews of Modern Physics*, **11** (1939) 288.

[6] G. Wentzel, *Zeitschrift für Physik*, **43** (1927) 521.

[7] C. Davisson and L. H. Germer, *Physical Review*, **30** (1927) 705.

[8] L. De Broglie, *Nature*, **112** (1923) 540.

[9] G.Attard and C.Barnes, *Surfaces* (1998) Oxford University Press.

[10] E.M. McCash, *Surface Chemistry* (2007) Oxford University Press.

[11] J. C. Slater, *Physical Review*, **51** (1937) 846.

[12] D. P. Woodruff and T. A. Delchar, *Modern Techniques of Surface Science 2nd Ed.* (1994) Cambridge University Press.

[13] M. A. van Hove, W. H. Weinberg, and C.-M. Chan, *Low Energy Electron Diffraction:*

Experiment, Theory and Surface Structure Determination (1986) Springer-Verlag.

[14] M. A. van Hove and S. Y. Tong, *Surface Crystallography by LEED* (1979) Springer-Verlag.

[15] G. Held and W. Braun, *Cambridge LEED Package*, private communication.

[16] L. F. Mattheiss, *Physical Review*, **133** (1964) 1399.

[17] J. B. Pendry, *Journal of Physics C: Solid State Physics*, **13** (1980) 1937.

[18] G. Held, *CLEED manual*, private communication.

[19] J. Stohr and D.A. Outka, *Physical Review B*, **36** (1987) 7891.

[20] G. Hähner, *Chemical Society Reviews*, **35** (2006) 1244.

[21] E.Bauer, *Journal of Electron Spectroscopy and Related Phenomena*, **185** (2012) 314.

[22] T.Schmidt, U.Groh, R.Fink and E.Umbach, *Surface Review and Letters*, **9** (2002) 223.

[23] E. Bauer, *Journal of Physics: Condensed Matter*, **13** (2001) 11391.

[24] T. Kinoshita, *Journal of Electron Spectroscopy and Related Phenomena*, **124** (2002) 175.

[25] Y. Hwu, W. L. Tsai, B. Lai, J. H. Je, G. H. Fecher, M. Bertolo, and G. Margaritondo, *Surface Science*, **188** (2001) 480.

[26] K. Müller, Y. Bürkov and D. Schmeisser, *Thin Solid Films*, **307** (2003) 431.

[27] S. Aggarwal, A. P. Monga, S. R. Perusse, R. Ramesh, V. Ballarotto, E. D. Williams, B.R. Chalamala, Y. Wei and R. H. Reuss, *Science*, **2235** (2000) 287.

[28] M. Kim, M. Bertram, M. Pollmann, A. von Oertzen, A. S. Mikhailov, H.H. Rotermund, and G. Ertl, *Science*, **1357** (2000) 292.

[29] M. R. Freeman and B. C. Choi, *Science*, **1484** (2001) 294.

[30] T. Schmidt, U. Groh, R. Fink, E. Umbah, O. Schaff, W. Engel, B. Richter, H. Kuhlenbech, R. Schlogl, H.-J. Fruend, A.M. Bradshaw, D. Preikszas, P. Hartel, R. Spehr, H. Rose, G. Lilienkamp, E. Bauer and G. Benner, *Surface Review and Letters*, **9** (2002) 223.

[31] S.Günther, B.Kaulich, L.Gregoratti and M.Kiskinova, *Progress in Surface Science*, **70** (2002) 187.

[32] E Bauer, *Journal of Physics: Condensed Matter*, **13** (2001) 11391.

[33] G. Hähner, *Chemical Society Reviews*, **35** (2006) 1244.

[34] E. Bauer, *Proceedings of the Fifth International Congress on Electron Microscopy* (1962) Academic Press.

[35] W. Telieps and E. Bauer, *Ultramicroscopy*, **17** (1985) 57.

[36] M.S. Altman, *Journal of Physics: Condensed Matter*, **22** (2010) 084017.

[37] E. Bauer, *Reports on Progress in Physics*, **57** (1994) 895.

[38] E. Bauer, *Surface Review Letters*, **5** (1998) 1275.

[39] R.M. Tromp, *IBM Journal of Research and Development*, **44** (2000) 503.

[40] R.J. Phaneuf and A.K. Schmid, *Physics Today*, **56** (2003) 50.

[41] Chmelik J, Veneklasen L and Marx G, *Optik*, **83** (1989) 155.

[42] G.F. Rempfer, D.M. Desloge, W.P. Skoczylas and O.H. Griffith, *Microscopy and Microanalysis*, **3** (1997) 14.

Chapter 3: Instrumentation

3.1 Beamline 11.0.2 at the Advanced Light Source

A schematic of the main beamline components is presented in figure 3.1. The beamline utilises photons from an undulator with a 5 cm period. The Advanced Light Source (ALS) operates at an energy of 1.9 GeV and beamline 11.0.2 is able to provide photons that are in the energy range 75-2150 eV. After emerging from the undulator, the photons are focused vertically by a sagittal cylinder mirror onto the pre-mirror of an SX700 style plane-grating monochromator. The light from the monochromator is stigmatically focused by either of two toroidal focus mirrors onto either the SXTM or the spectroscopy branch line. The beam is directed towards a specific branch line by positioning the spectroscopy mirror either in or out of the path of the beam. The exit slits are used to either illuminate the zone plate of the SXTM, or a pair of Kirkpatrick-Baez (KB) mirrors in the spectroscopy branchline. These mirrors can focus the radius of the spot of light on the sample down to 7 µm × 10 µm [1].

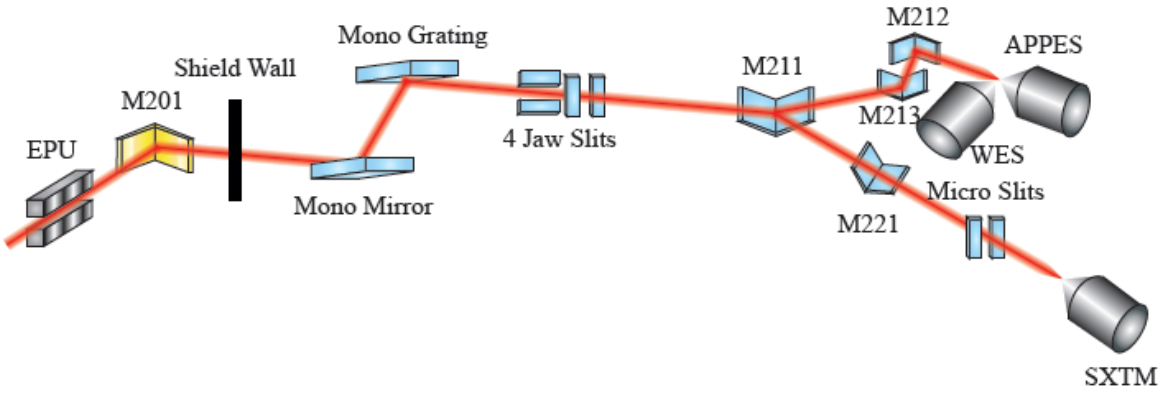

Fig 3.1: *Schematic layout of the MES beamline (11.0.2) at the Advanced Light Source* [1].

The beamline houses three dedicated endstations; the SXTM is permanently installed in-situ at its dedicated branch line. The two spectroscopy chambers (ambient pressure photoelectron and wet spectroscopy endstations) share the spectroscopy branchline and are moved and out of the path of the beam on air bearings. The endstations can be switched within 30 minutes and the vacuum need not be broken. Additionally, external user endstations can be mounted on a separate platform and swung in to the path of the beam (the 'on-beam' position).

The ambient pressure photoemission spectrometer allows samples to be held under pressures of up to 10 Torr during spectroscopic investigation. A schematic of the endstation is presented in figure 3.2. Incident X-rays from the beam line are admitted to the ambient pressure chamber through a 100 nm thick, square silicon nitride widow (1 mm^2). The sample is situated a short distance (~0.5 mm) from an aperture with a diameter of 0.3 mm. This aperture is the entrance to the differentially pumped lens system and its short distance from the sample is essential to the functionality of the instrument due to the short mean free path of electrons at higher pressures. The electrons that are excited from the sample pass through the aperture into the first differential pumping stage and are focused onto a second aperture that is the entrance to the second differential pumping stage where they are focused onto a third aperture. The electrons pass through four differential pumping stages in total prior to their entrance into a final lens stage where they are focused onto the entrance slit of a hemispherical analyser. A situation can be maintained where pressure inside the hemispherical analyser is 8 orders of magnitude lower than that of the ambient pressure chamber [2].

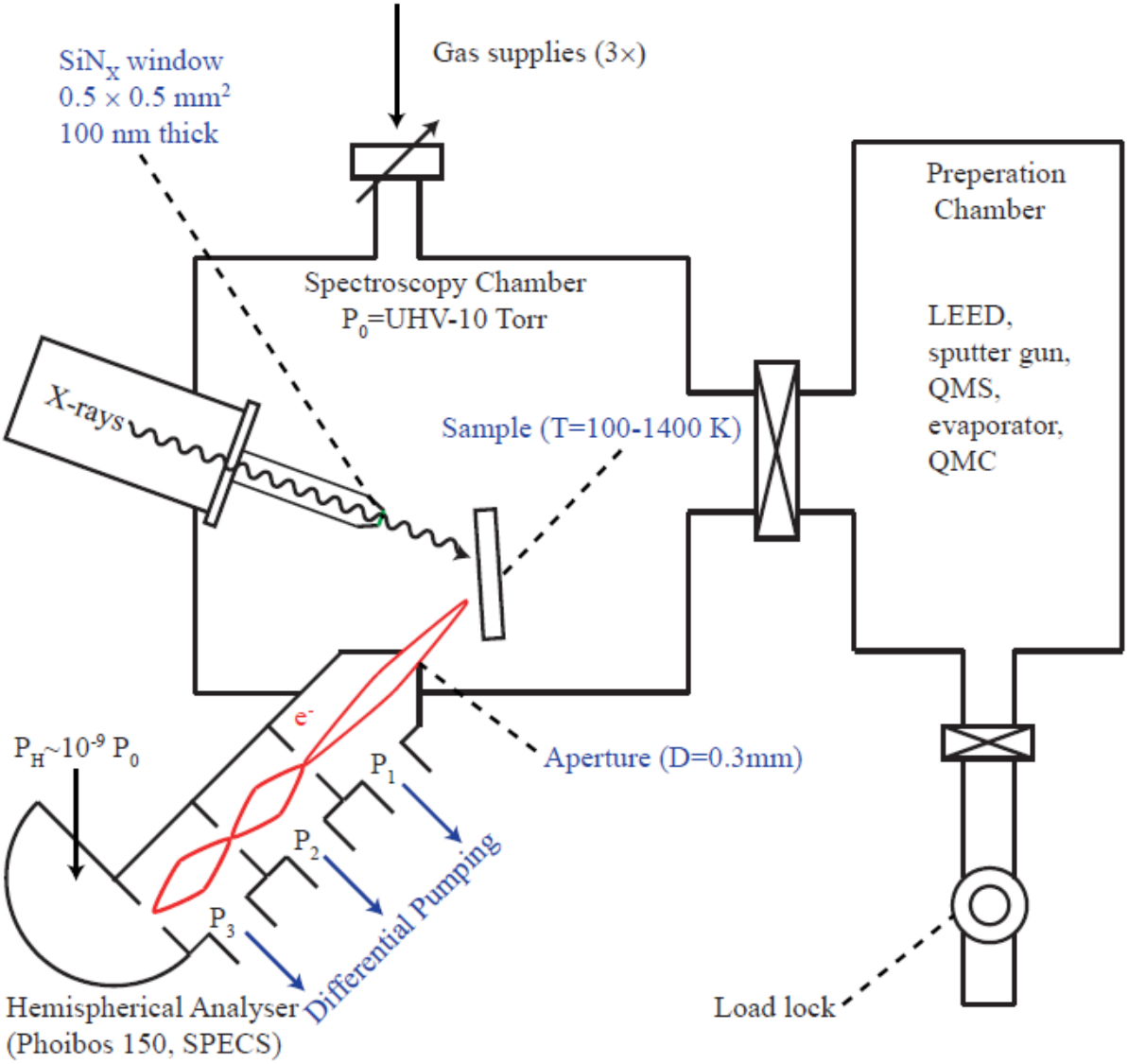

Fig 3.2: *Schematic layout of the APPES endstation* [3].

Additional to the ambient pressure chamber of the ambient pressure PES endstation is the preparation chamber, which is equipped with a sputter gun, a plasma source and a heater based plasma cleaning facility. There is also a combined LEED/AES instrument for the characterisation of samples and a gate valve connection to a load-lock chamber so that samples can be quickly transferred in and out of the system. The preparation chamber in beamline 11.0.2 at the ALS is held under ultra-high vacuum (UHV) conditions. When a sample is held under a

pressure of $<1\times10^{-9}$ Torr, it is said to be under UHV conditions. Samples become contaminated quickly in the ambient and the relative exposure can be quantified as a function of pressure. The exposure can be measured in units of Langmuirs, L:

$$L = P \times t \tag{3.1}$$

$$1L = 1 \times 10^{-6} Torr \cdot s$$

1L represents the exposure of a surface to 1 monolayer of adsorbate. In the ambient, 1L of exposure takes 10^{-6} seconds to occur but under 1×10^{-10} Torr of pressure it takes roughly 3 hours for the same surface to be exposed to the same extent of adsorbate. UHV is achieved by differential pumping combined with ion pumping and periodic titanium sublimation pumping [3].

The limit of the potential pressure differential between the environments to which the sample and the measurement apparatus are exposed can be increased by extending the length of the differentially pumped region or by shrinking the diameter of the aperture through which excited electrons pass into the lens system. The main functional components of the initial two stages of the four stage differential pumping lens system are represented in figure 3.3. Electrons excited from the sample enter the system through the small entrance aperture. The sample and the entrance aperture are grounded. The lenses encountered by a photoelectron as it passes through the system are referred to as the control, the skimmer, the condenser and the quadropole lenses. Four lenses comprise the quadropole lens system for deflection control. These lenses and the hemispherical analyser (not shown) are software controlled via a PC running LABVIEW [4].

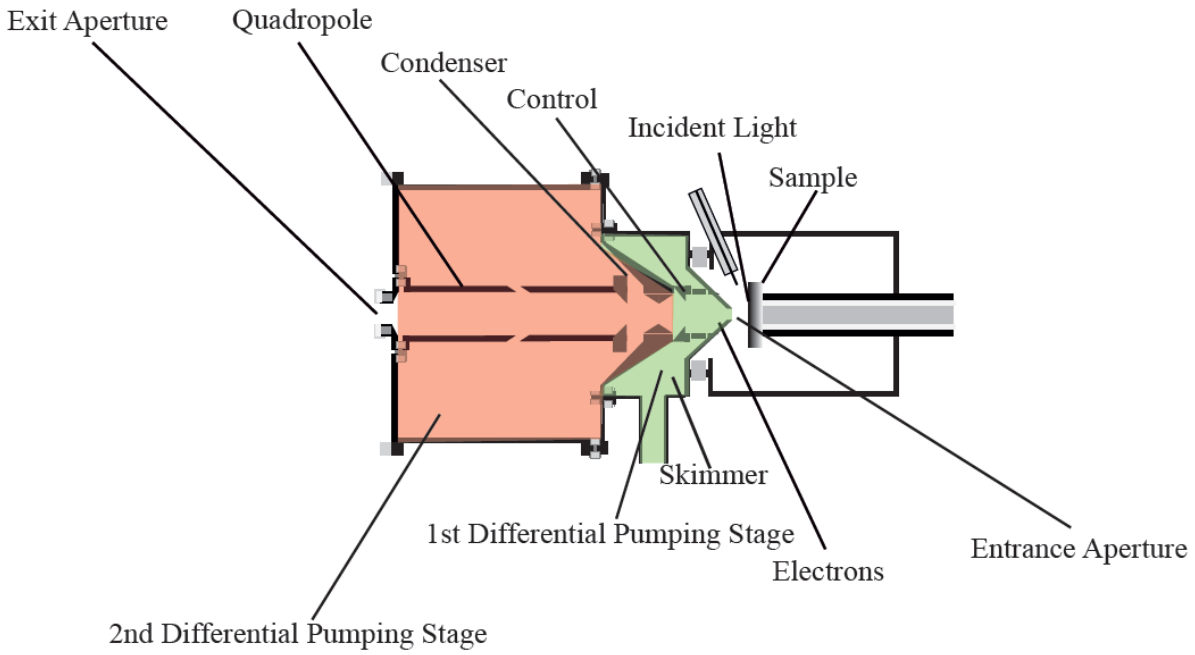

Fig 3.3: *Schematic describing the first two sections of the differential pumping system* [3].

The entrance aperture, control and skimmer electrodes form a three element lens to focus electrons into entrance of the second differential pumping stage and the skimmer, condenser and the quadropole form a four element lens, along with the exit aperture (the entrance to the third differential pumping stage, which is not shown) to focus the electrons onto the latter.

3.2 Beamline I06 at the Diamond Light Source

The Nanoscience beamline (I06) at the Diamond Light Source (DLS) produces variable circular and linear polarised radiation over the energy range 80-2100 eV. Circularly polarised light is available between 106-1300 eV, which is sufficient for probing the first row transition metal *L*-edges, the lighter rare-earth *M*-edges and C, N and O *K*-edges. The linearly polarised

light available from beamline I06 extends to 80-2100 eV, which encompasses the Si *L*-edges and the majority of the rare-earth *M*-edges.

Figure 3.4 shows a schematic representation of the main components of the beamline. Two 2.11m APPLE II undulators, both with a period of 64 mm, that are coupled via a magnetic phase shifter, provide left and right circularly polarised light and s and p linearly polarised light. A cylindrical mirror (M1) is located 24 m from the centre of the straight section of the storage ring. M1 is made from SiC and coated with Au and side cooled with water. This mirror absorbs most of the unwanted power from the insertion devices and collimates the beam in the vertical direction. This allows control of the fixed focus constant and the beamline can thus be optimised for either spectral resolution, harmonic rejection or transmission. The monochromator is a combination of a 450 mm side-cooled SiC plane mirror, half-coated with Au (M2) and three side-cooled Si plane gratings with line densities of 150, 400 and 1200 lines/mm. The 400 lines/mm grating is used over the energy range 210-2100 eV with a calibrated efficiency of 20% at 700 eV, decreasing to 16% at 1800 eV. The branchline toroidal mirror can be moved in and out of the path of beam as it emerges from the monochromator. If M6 is moved into the path of the beam, then the beam is focused towards the exit slits of the branchline. If it is kept out of the path of the beamline, it encounters a different toroidal mirror that focuses it onto the exit slits of the PEEM. The beamline is equipped with a high level of motorised diagnostics including X-ray beam position monitors in the front end. Si diodes can be inserted before and after each optic to measure beamline flux and drain current measurements from mirrors for energy calibration [5].

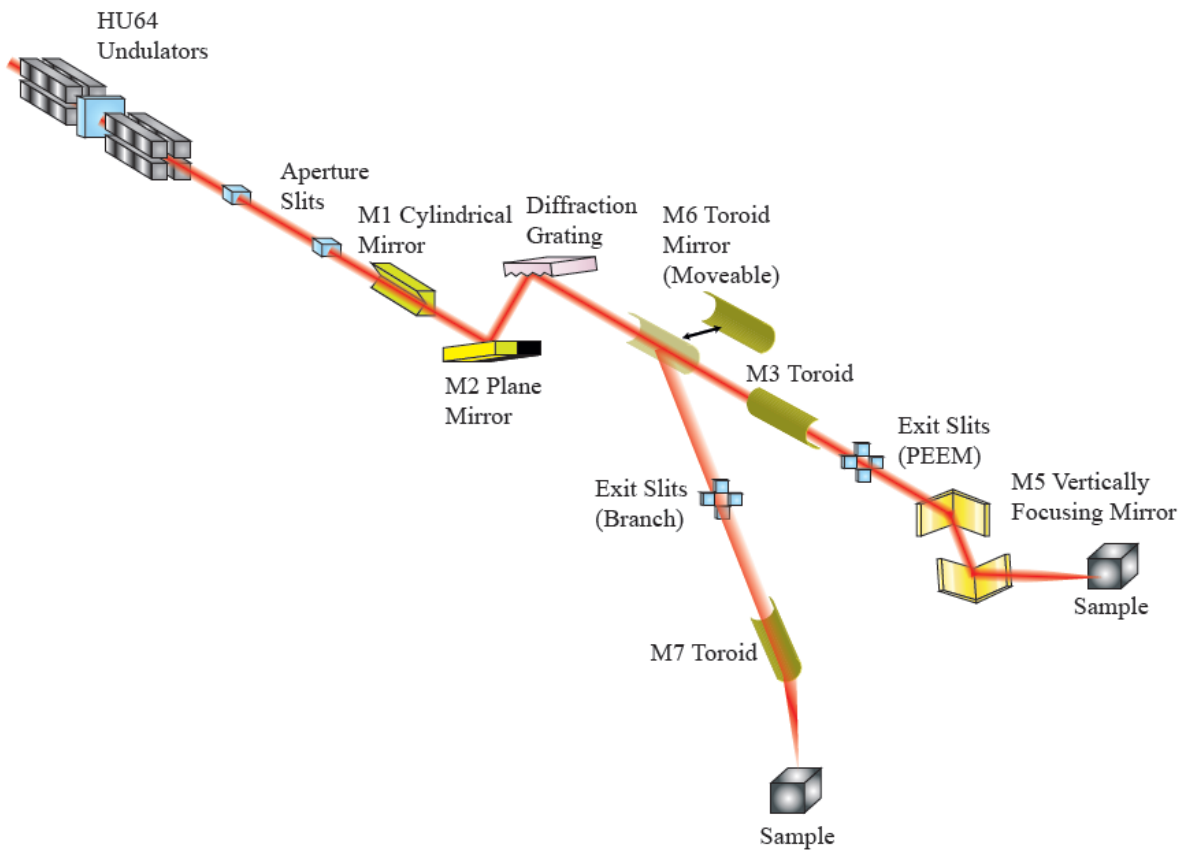

Fig 3.4: *Schematic of main components of beamline I06 at the DLS* [5].

Figure 3.5 is a top-down schematic of the PEEM endstation. It is an Elmitec LEEM III spectroscopic photoemission and low energy electron microscope (SPELEEM). Photoemission and X-ray absorption measurements can be performed at a spatial resolution of ~100 nm with a typical photon energy (hν) resolution of ~70 meV at 450 eV and during XPEEM imaging. The PEEM endstation is also equipped with scanning tunnelling microscopy and is separated from a preparation chamber by a gate valve. The preparation chamber is equipped with a sputter gun as well as a heater for sample preparation. Rudimentary characterisation of samples following preparation can be made using the LEED and AES facilities in the same chamber. A load lock is available for easy exchange of samples in and out of the preparation chamber. Evaporators can be attached to the preparation chamber.

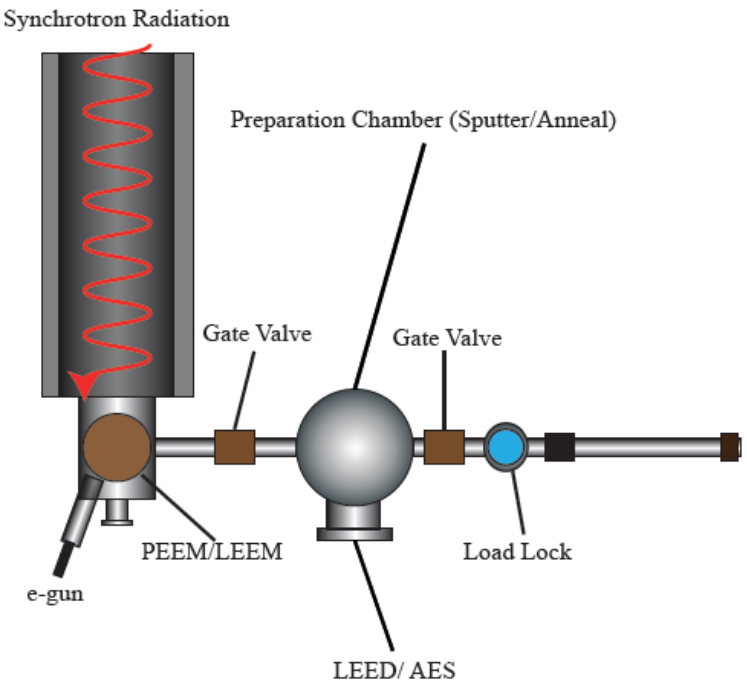

Fig 3.5: *The PEEM endstation at beamline I06.*

The basic design of the SPELEEM is shown in figure 3.6. The SPELEEM comprises a main chamber that is connected to the preparation chamber (not shown, the two chambers are separated by a gate valve), an illumination column, a magnetic beam separator with a deflection angle of 60°, a hemispherical energy analyser and a connection to the beamline. There is also an electron gun with three condensor lenses (C1,C2 and C3) that has a high electron flux (LB_6 cathode) and a UV lamp (Hg, 4.8 eV).

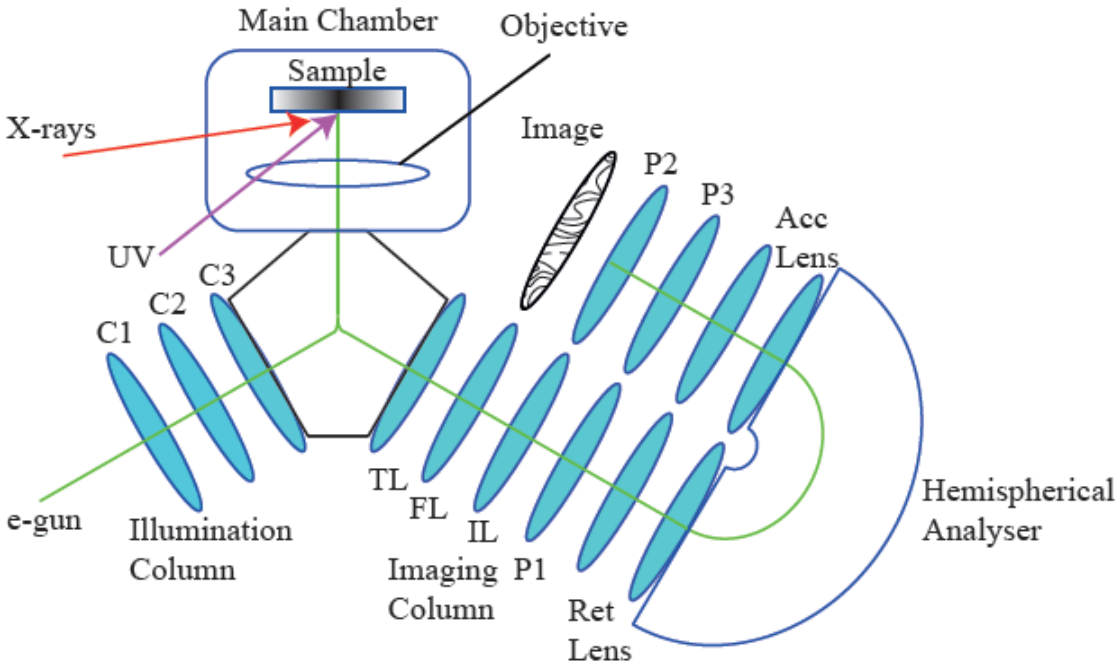

Fig 3.6: *Schematic diagram of SPELEEM. Adapted from* [6]

When the sample interacts with UV light, X-rays or low energy electrons, the photoemitted or reflected electrons that emerge from the surface form a magnified image in the image plane and a diffraction pattern in the back focal plane of the objective lens. The electrons (at this stage, forming a reciprocal interpretation of a real space image of the surface), are transferred to the imaging column by the transfer lens (TL) where they are magnified by the field lens (FL) and the intermediate lens (IL) before being projected by the IL and the first projective lens (P1), through the energy retarding lenses (ret lens) into the energy analyser. The energy-selected electrons that emerge from the energy analyser are accelerated (acc lens) and projected (P2 and P3) onto a micro-channel plate (MCP) with a phosphorous screen [7].

References

[1] H. Bluhm, K. Andersson, T. Araki, K. Benzerara, G.E. Brown, J.J. Dynes, S. Ghosal, M.K. Gilles, H.Ch. Hansen, J.C. Hemminger, A.P. Hitchcock, G. Ketteler, A.L.D. Kilcoyne, E. Kneedler, J.R. Lawrence, G.G. Leppard, J. Majzlam, B.S. Mun, S.C.B. Mynem, A. Nilsson, H. Ogasawara, D.F. Ogletree, K. Pecher, M. Salmeron, D.K. Shuh, B. Tonner, T. Tyliszczak, T. Warwick and T.H. Yoon, *Journal of Electron Spectroscopy and Related Phenomena*, **150** (2006) 86.

[2] M. Salmeron and R. Schlogl, *Surface Science Reports*, **63** (2008) 169.

[3] E.M. McCash, *Surface Chemistry 1st Ed.* (2001) Oxford University Press.

[4] D.F. Ogletree, H. Bluhm, G. Lebedev, C.S. Fadley, Z. Hussain and M. Salmeron, *Review of Scientific Instruments*, **73** (2002) 3872.

[5] S.S. Dhesi, S.A. Cavill, A. Potenza, H. Marchetto, R.A. Mott, P. Steadman, A. Peach, E.L. Shepherd, X. Ren, U.H. Wagner and R. Reininger, *AIP Conference Proceedings*, **1234** (2010) 311.

[6] https://www.maxlab.lu.se/node/799.

[7] Th. Schmidt, S. Heun. J. Slezak, J. Lilienkamp and E. Bauer, *Surface Review and Letters*, **5** (1998) 1287.

Chapter 4: XPEEM and NEXAFS Study of the CO/Pd(111)/TiO_2(110) Model Catalyst System

4.1 Introduction

Modern industrial catalysts are often composed of metal nanoparticles dispersed on a metal oxide substrate. The size and coverage of the nanoparticles are tailored for optimum reactivity and selectivity [1]. Catalysts in industry have reached a level of complexity where single crystals are insufficient analogues. Experiments performed on such samples cannot account for two very important characteristics of practical catalysts; firstly, the dependence of the reactivity and selectivity of the system on the size and shape of the nanoparticles [2], and secondly, the interface between the nanoparticles and the metal oxide support [3]. This can modify the electronic properties of the nanoparticles or in some cases encapsulate them in the form of the strong metal–support interaction (SMSI) [4-6].

Supported model catalysts, metal nanoparticles deposited on well-characterised metal oxide-single crystals [7-9], can be developed that are excellent equivalents of practical catalysts. Applying the techniques of surface science to these systems allows precise characterisation of the morphology and electronic structure. Pd/TiO_2 catalysts are widely utilised in industry,

primarily in three-way automobile catalysis as a major component in CO and hydrocarbon oxidation and nitrogen oxide reduction [10].

When Pd is deposited on TiO_2(110) at room temperature (RT), clusters tend to form at step-edges [11]. It is apparent that the preferred nucleation site is influenced by the defect concentration as a more uniform distribution is observed on a highly defective substrate surface [12]. STM studies have revealed that the growth mechanism for Pd on TiO_2(110) is Volmer-Weber like [13]; Pd atoms on the surface of the substrate coalesce to form 3D islands before merging to form a thin film at a critical coverage. The predominant termination of the nanoparticles is the (111) facet and this follows the general trend for noble metals grown on TiO_2(110) [13]. Further STM studies carried out on nanoparticulate systems have shown that Pd nanocrystals are morphologically pseudo–hexagonal on the TiO_2(110) surface [14]. Humphrey et al [15] were able to show that the anisotropy of the TiO_2(110) surface allows directional growth of Pd nano-rods. In their experiment, 1.4 ML of Pd was deposited on a TiO_2(110) substrate at 700 K and following annealing to 723 K, the nanoparticles were elongated along the [001] direction to remarkable aspect ratios (5 x 1000 nm^2).

The bonding of CO to metallic surfaces is subtle and complicated. CO bonds via three-fold hollow sites on Pd(111) but favours atop sites on the chemically similar Pt(111) [16]. At higher coverage, the interactions between adsorbed molecules adds another dimension of complexity. At 0.33 ML coverage and below, the formation of islands occurs as a result of attraction between CO molecules [17]. Between 0.33 and 0.75 ML, repulsive forces between the molecules weaken bonding to the surface [18].

$Pd/TiO_2(110)$ is a potentially important catalyst that is becoming better understood but its physically complex nature means that further study is required to provide a complete understanding of the system. In this chapter, I present a study of CO adsorption on a $Pd/TiO_2(110)$ model catalyst system that employs a number of surface science techniques including AES, XPEEM and μ-NEXAFS to probe the nucleation and orientation.

4.2 Experimental

All measurements were carried out on beamline I06 at the Diamond Light Source [19] (See Chapter 3). This soft X-ray beamline provides circularly and linearly polarised light over a wide energy range (80 – 2100 eV). The polarisation of the light is controlled by means of an undulator. Circularly polarised light is available over the energy region 106-1300 eV and this facilitates studies of the first row transition metal L-edges, the lighter rare-earths and the C, N and O K-edges. Linearly polarised light is available over the wider energy band 80-2100 eV and this covers the Si L-edges and the rare earth M-edges. The beamline is most commonly used for experiments that investigate the magnetic state, the morphology and the chemical composition of materials using PEEM. By combining the spatial resolution of PEEM with the capability of NEXAFS to reveal the bonding orientation of molecules on surfaces, it is possible to study how CO adsorbs on a single Pd nanostructure supported on $TiO_2(110)$.

The end station is an Elmitec LEEM III spectroscopic photoemission and low energy electron microscope (SPELEEM) (Described in detail in chapter 3). The spatial resolution of the microscope is < 8 nm when an electron source is utilised. Using soft X-rays, a resolution of 30-50 nm can be achieved on an ideal surface. The preparation chamber is equipped with a sputter

gun and heater for sample cleaning and LEED and AES are available for sample characterisation.

A rutile TiO_2(110) sample *(Pi-Kem)* was prepared by cycles of Ar^+ sputtering and annealing to 1000 K until a (1×1) low energy electron diffraction (LEED) pattern was observed and no contaminants were detected during Auger electron spectroscopy (AES) measurements. Pd was dosed by metal vapour deposition (MVD) on TiO_2(110) with the sample held at 900 K. The deposition source consists of Pd rods contained in a molybdenum (Mo) crucible that is heated by electron bombardment. The presence of well-defined Pd nanoparticles was verified with LEED, AES and XPEEM. Research grade CO was dosed by backfilling the analysis chamber via a precision leak value. The purity of CO was checked using Quadropole Mass Spectrometry (QMS).

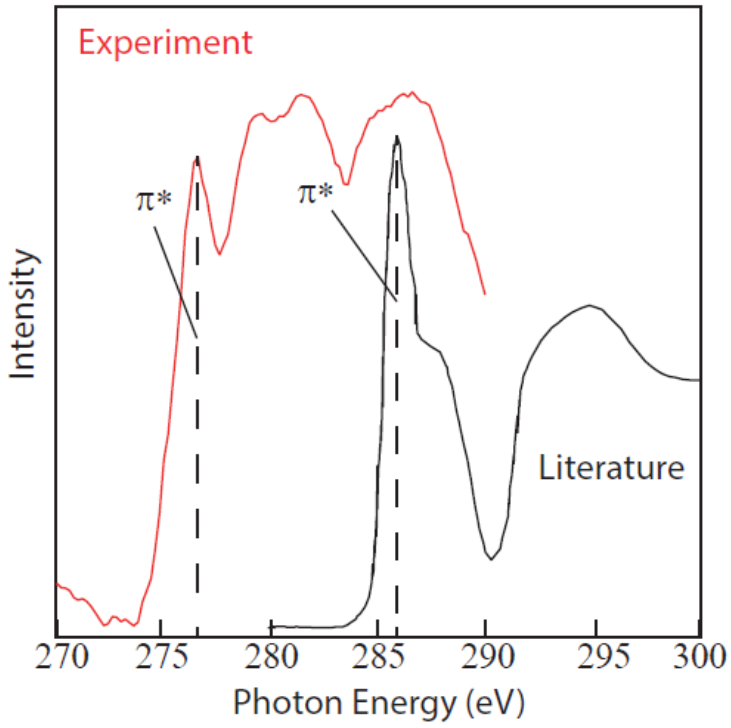

Fig 4.1: *Comparison of NEXAFS spectra of graphite from Beamline I06 (red) with a published spectrum (black)* [20] *as a means of calibrating experimentally observed resonances to the correct incident photon energy.*

Calibration of the photon energy was achieved by performing carbon K-edge NEXAFS measurements on a graphite sample and comparing the position of the associated π* resonance peak with that in the literature [20]. As shown above in figure 4.1, the π* resonance peak measured in Beamline I06 occurred at a nominal energy of 276.6 eV, 9.3 eV lower than the published value [20]. This means that during the experiment the *actual* photon energy was related to the *nominal* value as below:

$$h\nu(actual) = h\nu(nominal) + 9.3eV \quad (4.1)$$

All XPEEM images and NEXAFS spectra presented in this chapter are calibrated in accordance with these findings. The experimental and literature spectra in figure 4.1 were normalized to each other using the height of the rising π* peak of graphite.

4.3 XPEEM Imaging of Pd/TiO_2(110)

Pd was deposited onto the TiO_2(110)-(1×1) substrate held at 900 K and a faint Pd(111) LEED pattern was observed, superimposed on the TiO_2(110)-(1×1) LEED pattern arising from diffraction from the substrate due to the formation of well-defined nanoparticles (Figure 4.2).

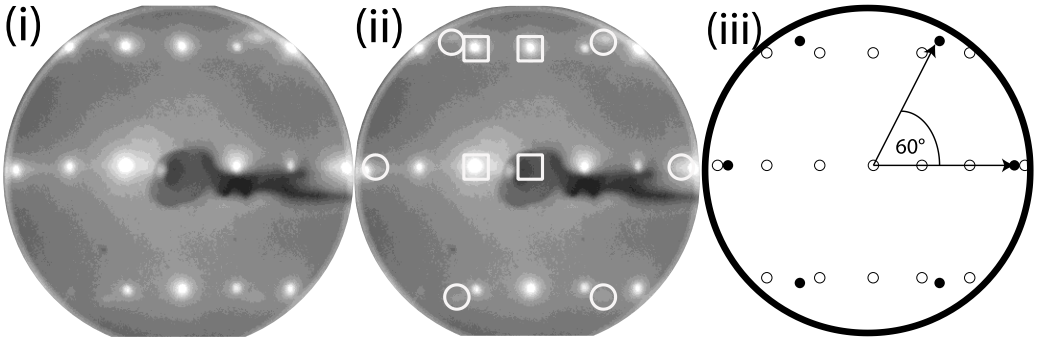

Fig 4.2: *(i) Pd(111)/TiO_2(110) imaged with LEED at 140 eV.(ii) Contributions from TiO_2(110)-(1 ×1) are highlighted with squares and Pd(111) LEED spots are highlighted with circles. A schematic of the pattern is presented in (iii) with TiO_2(110) spots represented by white circles and Pd(111) spots represented by black circles.*

The lattice spacing on the (111) top-facet of the Pd nanoparticles was calculated as follows; first, by comparing the distance between the diffraction spots arising from the TiO_2(110) substrate with the corresponding distance in real space [21], we found a correlation between the measurements taken in LEED and the real space values. Based on this and also taking into account the difference in the unit cell geometry between the (111) face of the Pd nanostructures and the TiO_2(110) substrate, the interatomic distance on the (111) top-facet was calculated to be 2.74 ± 0.07 Å, in good agreement with the bulk value of 2.75 Å for Pd.

The presence of Pd nanoparticles with appropriate dimensions was confirmed in XPEEM. The surface was imaged in secondary electron yield mode while the photon energy was ramped in increments of 2 eV from 320 eV to 430 eV (calibrated to the π* peak position of graphite). The exposure time for each image was only 5 seconds to minimize damage to the sample by the intense light produced by the beamline. Little intensity was observed from the surface when the incident energy was set to 320 eV, below the Pd $M_{4,5}$-edge (~329 eV). The Pd $M_{4,5}$-edge X-ray absorption cross section profile (figure 4.3) demonstrates that around 329 eV there

should be an onset of a broad rising edge as secondary electrons are emitted from the sample as a result of X-ray absorption by Pd nanostructures [22].

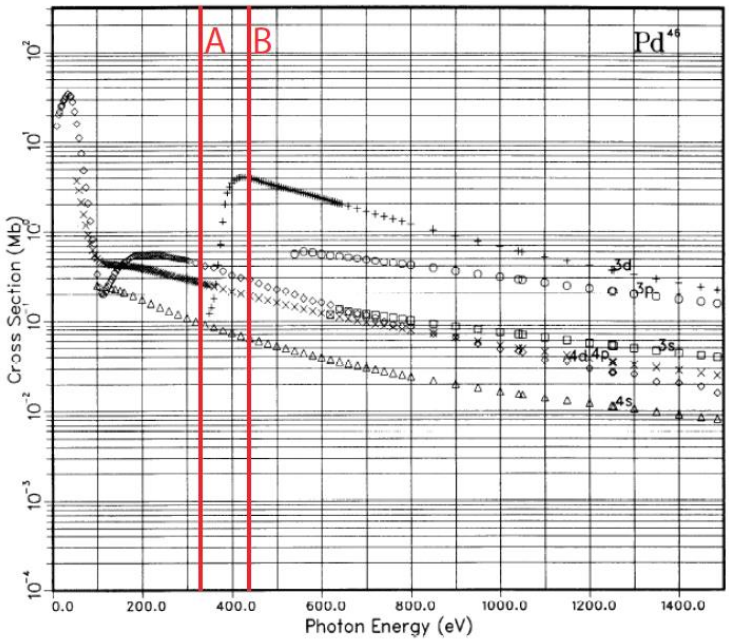

Fig 4.3: *X-ray photoelectron absorption cross section of the Pd $M_{4,5}$-edge. The red lines A and B enclose the energy region over which XPEEM measurements of Pd/TiO_2(110) were carried out as well as the rising Pd $M_{4,5}$-edge. Adapted from Ref* [22].

An XPEEM image is a real space representation of secondary electron photoemission from a sample [23]. Two secondary electron yield XPEEM images of Pd/TiO_2(110) are presented in figure 4.4. In figure 4.4 (i), an X-ray beam with hv = 320 eV was used to illuminate the sample. No contrast is apparent between the substrate and the nano-islands. The same area of the sample imaged at hv = 430 eV is displayed in figure 4.4 (ii). A profound contrast is evident between bright features and a dark background. The incident beam is energetic enough to cause excitation from Pd atoms on the surface but is below the Ti $L_{2,3}$-edge (453 eV) and the O K-edge (543 eV) [24]. As little intensity is observable from areas in-between these bright features, it is evident that Pd nanoparticles are present on the surface.

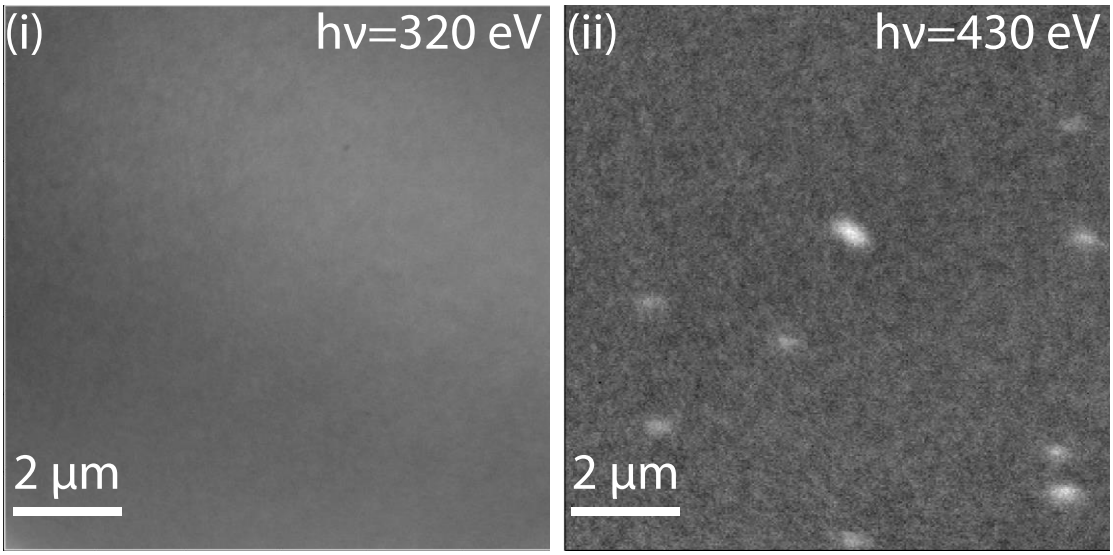

Fig 4.4: *10×10 µm^2, 20 µm FOV secondary electron yield XPEEM images of an identical area of Pd/TiO$_2$(110). This was imaged at (i) 320 eV, just below the Pd M$_{4,5}$-edge, with no contrast being evident between the nanoparticles and the substrate. At (ii) 430 eV, above the Pd M$_{4,5}$-edge, a large contrast between the nanoparticles and the substrate is obvious.*

Figure 4.5 shows a secondary electron emission XPEEM image of Pd/TiO$_2$(110). The energy of the incident beam is 430 eV and at this energy, as in the image above in figure 4.4 (ii), features attributed to Pd nanoparticles appear clearly against the dark substrate background. The field of view of this image is 10 µm and imaging at higher resolution allows a more detailed scrutiny of the surface and the Pd nanostructures, which are known to be pseudo-hexagonal from previous STM work [25]. The bright features have a diameter of 200 ± 50 nm and the intensity contribution from areas between the bright features is minimal in these higher resolution images provides further evidence that the majority of Pd deposited on the surface is contained in the islands. The spatial resolution in this case is 50 nm and it is difficult to discern if some smaller spots can be attributed to Pd islands or background.

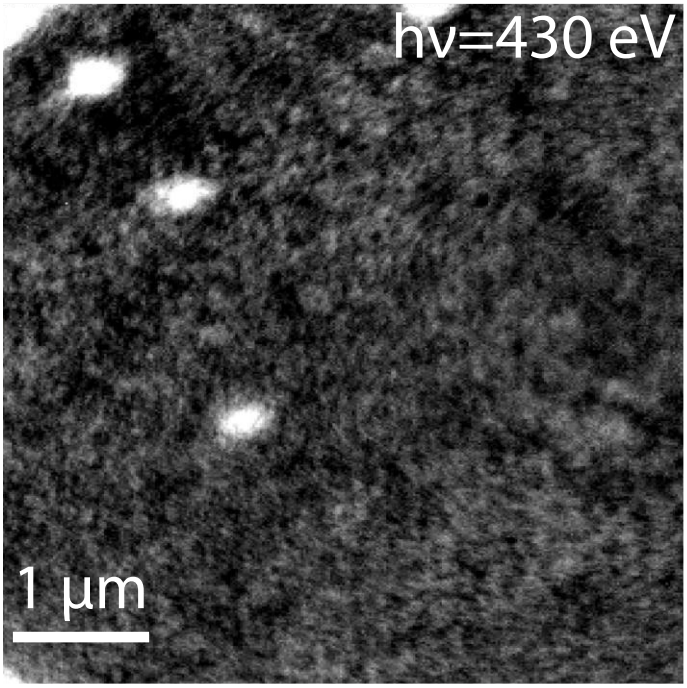

Fig 4.5: *5 × 5 μm², Pd/TiO₂(110) imaged in XPEEM operating in secondary electron yield mode. Imaging carried out using an incident energy of 430 eV and a 10 μm FOV. Clearly defined bright features pertaining to Pd nanoparticles indicates that the majority of Pd on the surface is contained in the nanostructures.*

4.4 XPEEM and μ-NEXAFS of CO/Pd/TiO_2(110)

Once it was confirmed that Pd had been successfully deposited on the surface and had formed well-defined nanoparticles, the surface was exposed to 120 L CO at RT. As CO does not adsorb on TiO_2(110) at 300 K [26], it was expected that CO would adsorb to the nanoparticles only. The signature from CO was expected to be present in XPEEM images recorded just above the carbon K-edge.

XPEEM images of the system in the range of the C K-edge after CO dosing (not shown) did not reveal any discernable bright features. Nevertheless, each pixel of an XPEEM image contains the intensity of the secondary electron yield for a given incident energy and spatially

resolved NEXAFS spectra can be built up if the intensity from a feature is plotted against the incident energy using a series of images. The data analysis software *Wavemetrics* IGOR PRO was utilized for this procedure. The steps undertaken in the analysis procedure are highlighted in figure 4.6. Figure 4.6 (i) shows CO/Pd/TiO_2(110) imaged using XPEEM with the incident energy of the X-ray beam set to 430 eV. From this image, the position of the nanoparticles could easily be identified visually. Regions of interest were selected in IGOR PRO that enclosed the nanoparticles as in figure 4.6(ii). A mask wave was created from these regions of interest that blocked out any information not contained within them. This mask wave was then superimposed onto a series of images of the same area of the sample taken in the range of the C K-edge. From this series of images, C K-edge μ-NEXAFS spectra of the nanoparticles and the substrate were generated.

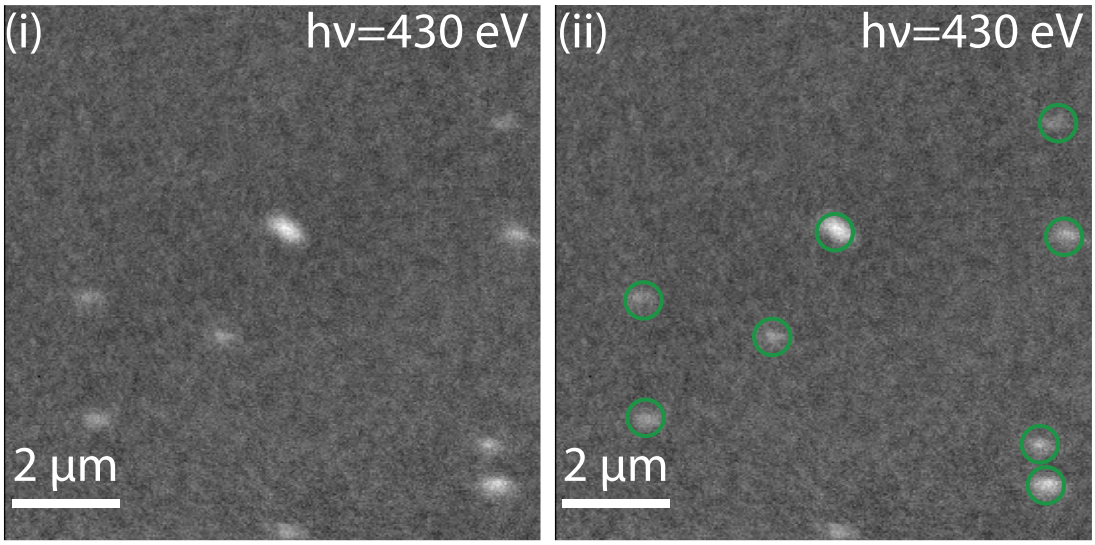

Fig 4.6: *(i) 20 μm FOV secondary electron emission XPEEM image of Pd/TiO_2 (110) imaged at 430 eV just above the Pd $M_{4,5}$-edge. Bright features correspond to Pd nanoparticles. (ii) The same image with nanoparticles selected as ROIs highlighted with green circles.*

Figure 4.7 (i) shows carbon K-edge spectra recorded from the TiO_2(110) surface, before and after CO dosing. It is evident after normalization that CO has not been adsorbed to the substrate

as the spectra share the same features thus it is sufficient to use substrate spectra from dosed images as background, as was carried-out. A spectrum collected from on top of a nanoparticle is compared with a spectrum collected from the substrate after dosing CO in figure 4.7 (ii). Spectra collected from on top of nanoparticles have a well-pronounced π*-resonance at 287.5 eV.

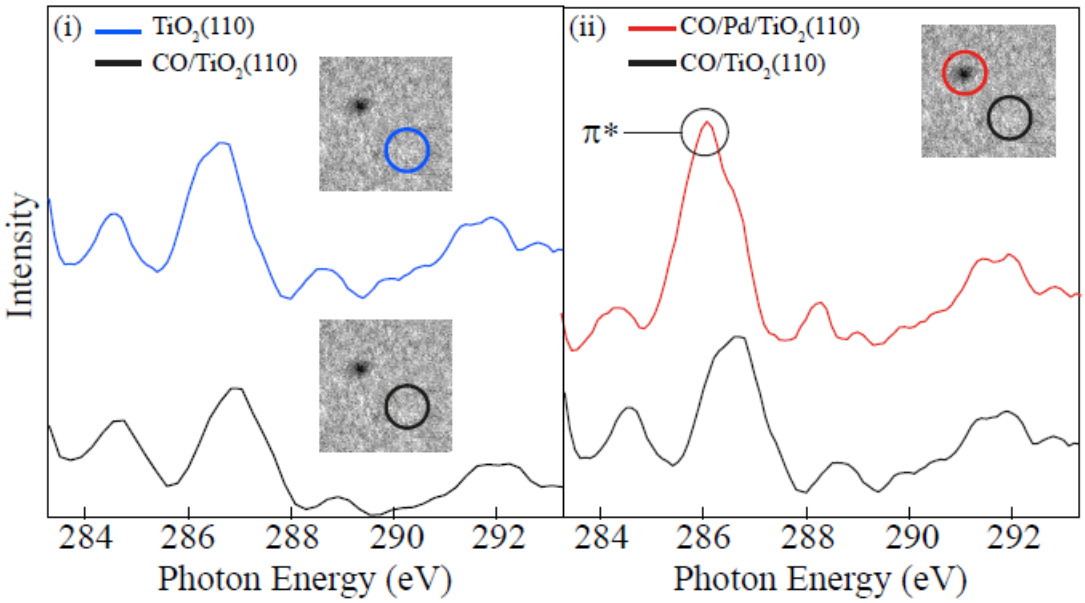

Fig 4.7: *Comparison of C K-edge μ-NEXAFS of different areas of CO/Pd/TiO_2(110) recorded with the E-vector perpendicular to the surface normal. (i) C K-edge μ-NEXAFS spectra taken from an area of the as-prepared TiO_2(110) surface, indicated by the XPEEM image inset, before (blue) and after (black) dosing CO. Both spectra share features, indicating CO has not adsorbed to the substrate. (ii) C K-edge μ-NEXAFS spectra of CO/Pd/TiO_2(110) taken from on top of a nanoparticle (black) and from an area of the substrate (red). The enhanced signal at around 286 eV suggests CO has bonded to the Pd nanocrystals.*

Structure from the beamline (background) contained in spectra collected from the substrate in the region of the π* resonance can create the false appearance of a resonance. Beamline structure was removed from spectra collected from Pd nanoparticles after CO deposition by subtracting spectra from the substrate where it was known no resonances would occur in this

energy range. The normalisation of C K-edge spectra was complicated by the commonplace problem of carbon contamination of the beamline optics that had accumulated over their lifetime. This led to a large dip in the intensity of the signal as the incident energy approached that of the C K-edge resonance. This dip is highlighted in the C K-edge spectrum from the TiO_2(110) substrate taken in the energy range 280-300 eV prior to dosing, which is shown in figure 4.8. The intensity of the incoming beam is reduced by over 75% when the photon energy is tuned to the range of the C K-edge.

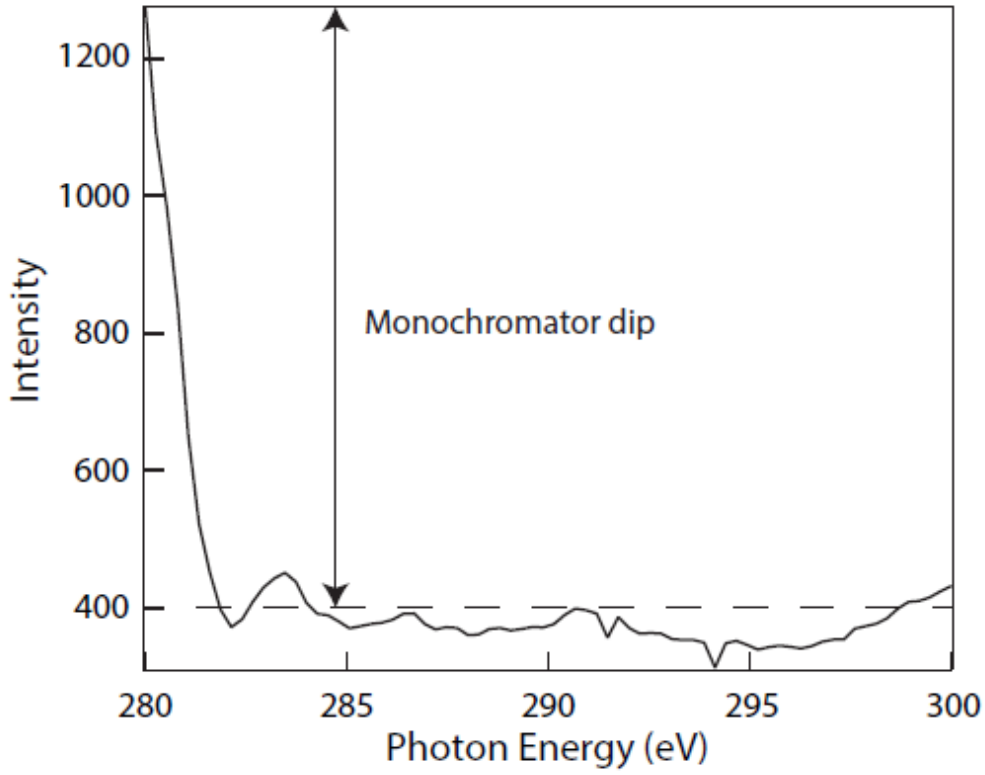

Fig 4.8: *C K-edge NEXAFS spectrum from TiO_2(110) substrate, revealing a large drop in intensity as the photon energy approaches the C K-edge.*

Image processing was carried out on XPEEM images collected at the C K-edge in an attempt to observe a contrast between the C K-edge emission from CO molecules bound to Pd nanoislands and the background. An image processing technique was developed that was

carried out on images captured above the Pd $M_{4,5}$-edge so that the degree of already visible contrast could be improved. This technique was then applied to images collected just above the C K-edge.

A spatially resolved 3D plot of an XPEEM image of Pd/TiO_2(110) imaged at 430 eV is presented in figure 4.9. The 3-dimensional spatial representation of intensity arising as a result of illumination of the system shows that the background levels vary dramatically across the surface, revealing that the experiment was limited by the spatial variation in efficiency of the micro-channel plate (MCP). The surface of the MCP encountered by photoelectrons emitted from the sample is a flat screen that is densely populated by tubes of the order of microns in diameter (micro-channels). Each of these tubes is a constant-dynode electron multiplier. Due to the extent of their use over their lifetime, some micro-channels are damaged and the efficiency is non-uniform across the MCP.

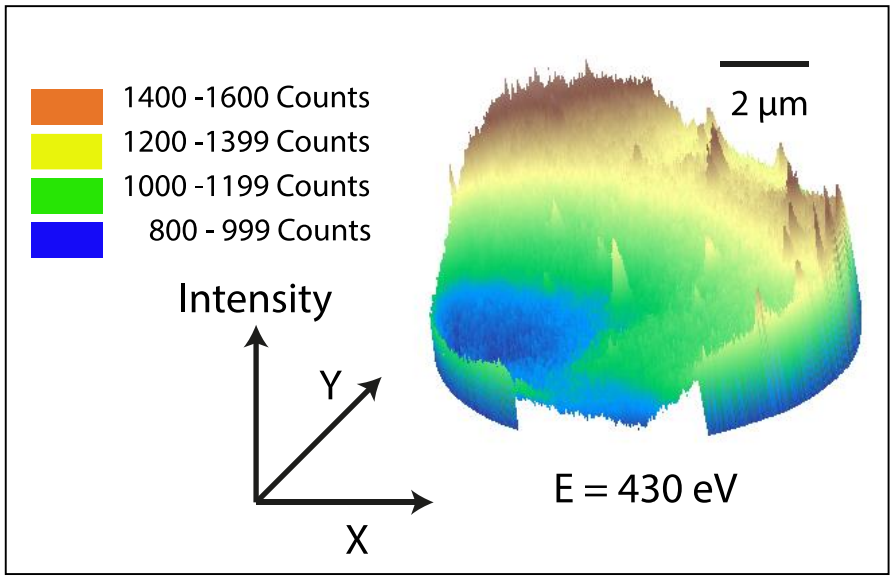

Fig 4.9: *3D graphical representation of spatially resolved intensity of 20 µm field of view, secondary electron yield XPEEM image of Pd nanoparticles dispersed across TiO_2(110) substrate surface. The varied efficiency across the channel plate can clearly be seen as well as spikes in intensity, which are attributed to secondary electron emission from Pd nanostructures.*

Images where bright protrusions attributed to Pd nanoparticles were presented against uniform background were manufactured in the following manner; the Gaussian smoothing function [27] stated below, was utilised:

$$G(r) = \frac{1}{2\pi\sigma^2} e^{-\frac{r^2}{2\sigma^2}} \quad (4.2)$$

G(r) is the intensity of the Gaussian profile at a radial distance of *r* from the origin (a given pixel) chosen during smoothening, and σ is the Gaussian width. When applied to an image in the *x* and *y* directions, a surface is produced which represents a 2D Gaussian distribution. Values from this distribution are used to build a convolution matrix that is applied to each pixel of original image. Each pixel's value is set to a weighted average based on its surroundings.

Setting *r* to a large value (1000 in this case) removes the fine features from these images. Intensity from the nanoparticles and white noise are smeared out leaving a shape that is essentially a representation of the relative channel plate efficiency in response to electrons generated from the sample at a given photon energy. Subtraction of this 'background' from the image from which it was manufactured constructs images such as presented in figure 4.10 where the system is imaged at the Pd $M_{4,5}$-edge. The absorption yield from the Pd nanoparticles at the Pd $M_{4,5}$ - edge appear in this image as spikes, well-defined against an even backdrop.

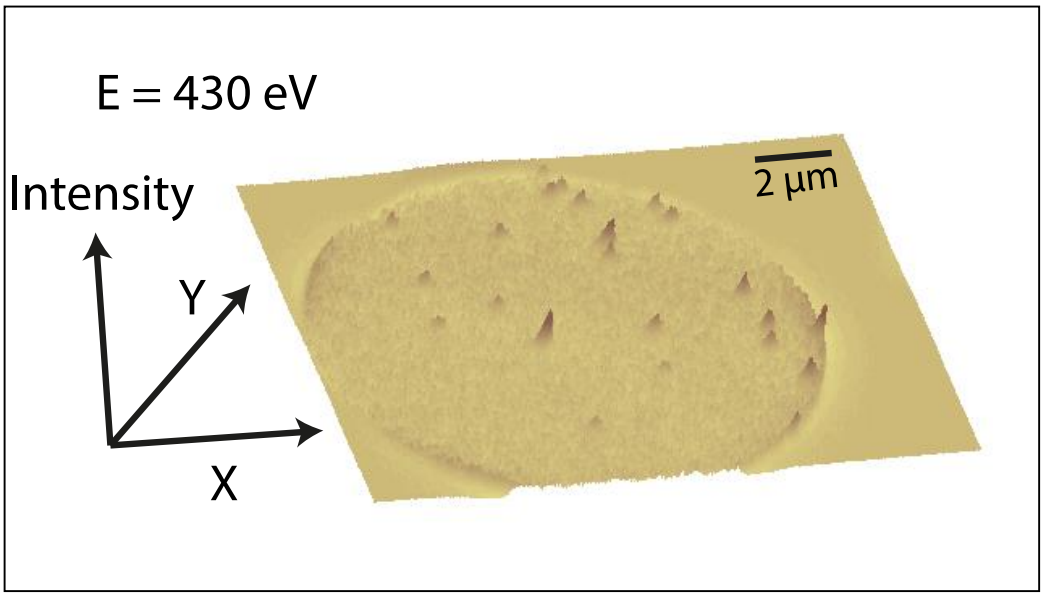

Fig 4.10: *3D graphical representation of a secondary electron yield XPEEM image, taken with an incident photon energy 430 eV, of Pd/TiO_2(110) with intensity spikes attributed to Pd nanoparticles against a uniform background from the channel plate.*

The application of this image processing technique to C K-edge images of CO/Pd/TiO_2(110) was combined with pixel binning, the process of combining the data in a group of pixels into a single pixel. This procedure improves intensity to the detriment of the spatial resolution. The CO signature cannot be beheld in C K-edge XPEEM images of CO/Pd/TiO_2(110) (not shown). This is due, most likely, to the weakened intensity of the incident beam when approaching the C K-edge.

Further µ-NEXAFS studies of the surface to probe the orientation of the π* bond of CO on Pd nanostructures were carried out. Figure 4.11 shows an area of the sample imaged above the Pd $M_{4,5}$-edge at 430 eV. Areas of spatially resolved secondary electron emission from nanoparticles show up brightly against the substrate. This area of the sample was imaged in the vicinity of the C K-edge as the electric vector was rotated. Due to limitations associated with

performing spectroscopy measurements at the C K-edge and the poor signal level, normalisation was complicated.

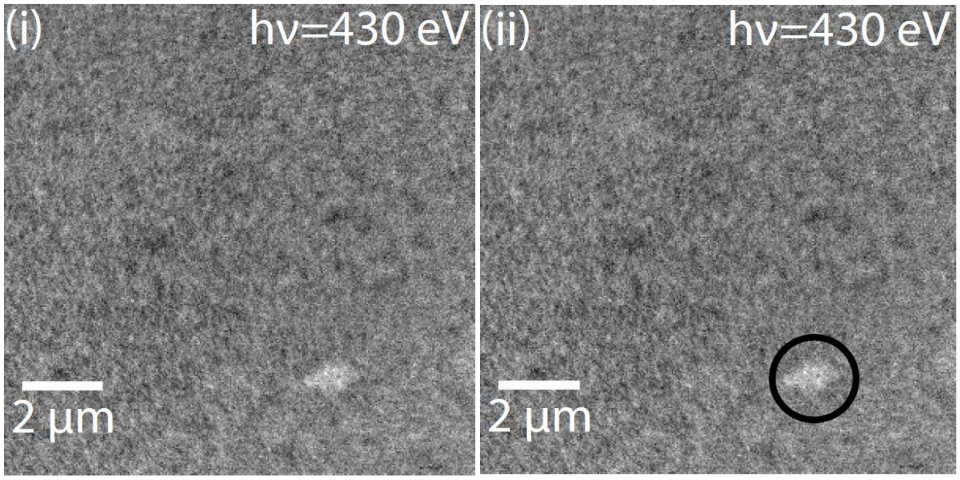

Fig 4.11: *(i) Pd $M_{4,5}$-edge XPEEM image of CO/Pd/TiO_2 recorded at 430 eV showing a bright feature identified as a Pd nanoparticle and (ii) the same image with the nanoparticle highlighted by a black circle for clarity.*

Figure 4.12 shows C K-edge spectra taken from nanoparticles and the substrate respectively when the *E*-vector was oriented at different angles (β) relative to the plane of incidence, normalised to each other. The beamline structure is unique to its *E*-vector orientation and this created a further challenge when performing normalisation and background subtraction.

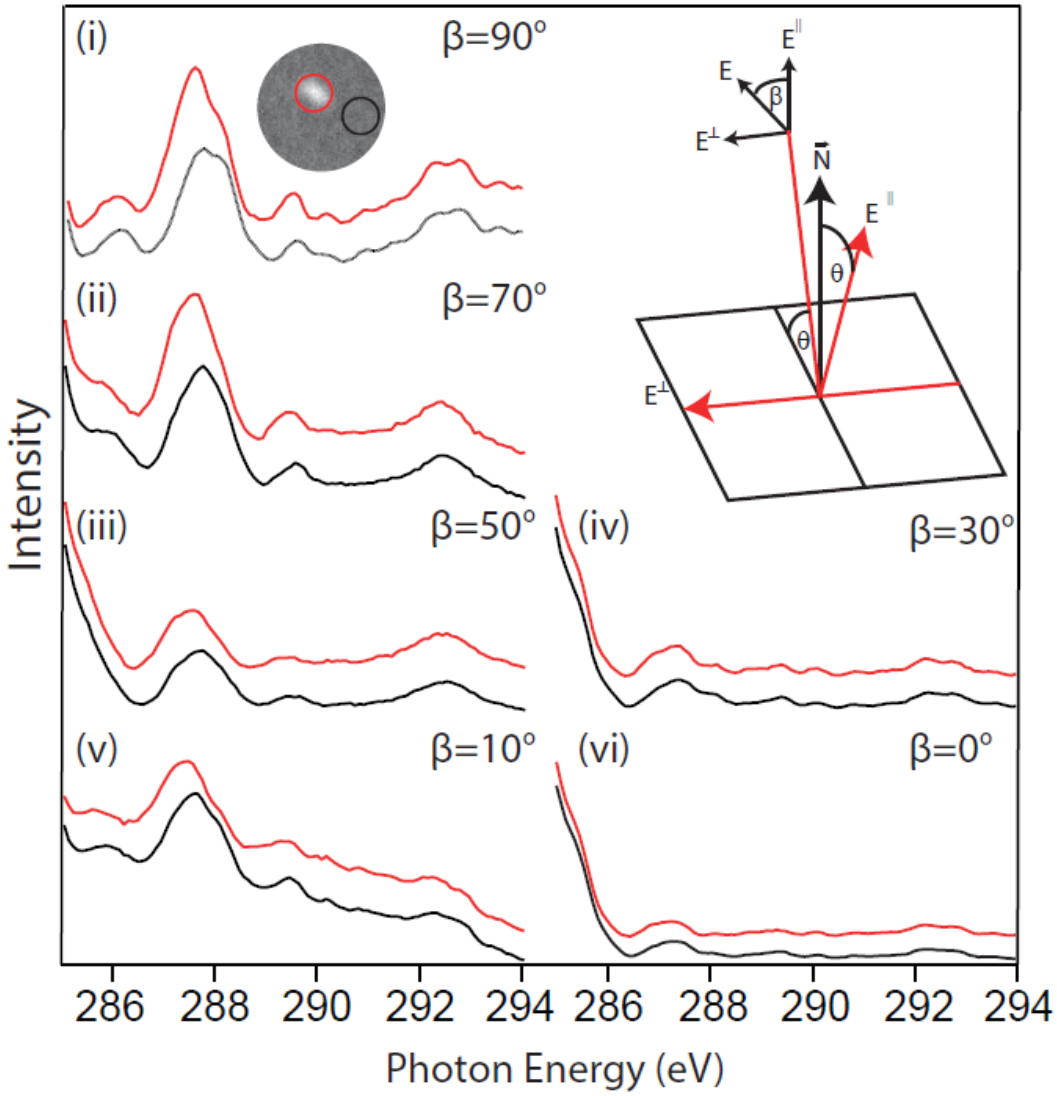

Fig 4.12: *C K-edge μ-NEXAFS spectra collected from nanoparticles (red) and the substrate background (black) when the E-vector is orientated (i) 90°, (ii) 70°, (iii) 50°, (iv) 30°, (v) 10° and (vi) 0° to* $E^{\parallel}$*. Inset; XPEEM image recorded at the Pd* $M_{4,5}$*-edge portrays the respective areas of the surface scrutinised using C K-edge NEXAFS to produce the spectra.*

The difference spectra for each polarisation are presented together in figure 4.13. Each spectrum has a sharp peak corresponding to the C 1s ⟶ 2π* resonance. A second peak is observed at about 289 eV, which is attributed to electron-hole pair excitations in the presence of a core hole. In CO gas phase measurements these peaks are well pronounced. When CO is chemisorbed to a substrate, the intensity of the peaks diminished considerably and can be

broadened to the extent where they are incorporated into the π* peak. Such a feature has been observed in C K-edge NEXAFS studies of CO/NiO(100) [28] and CO/Cu(100) [29]. The peak exhibits an angular dependence as it is a resonance representing a molecular orbital which is π* in nature.

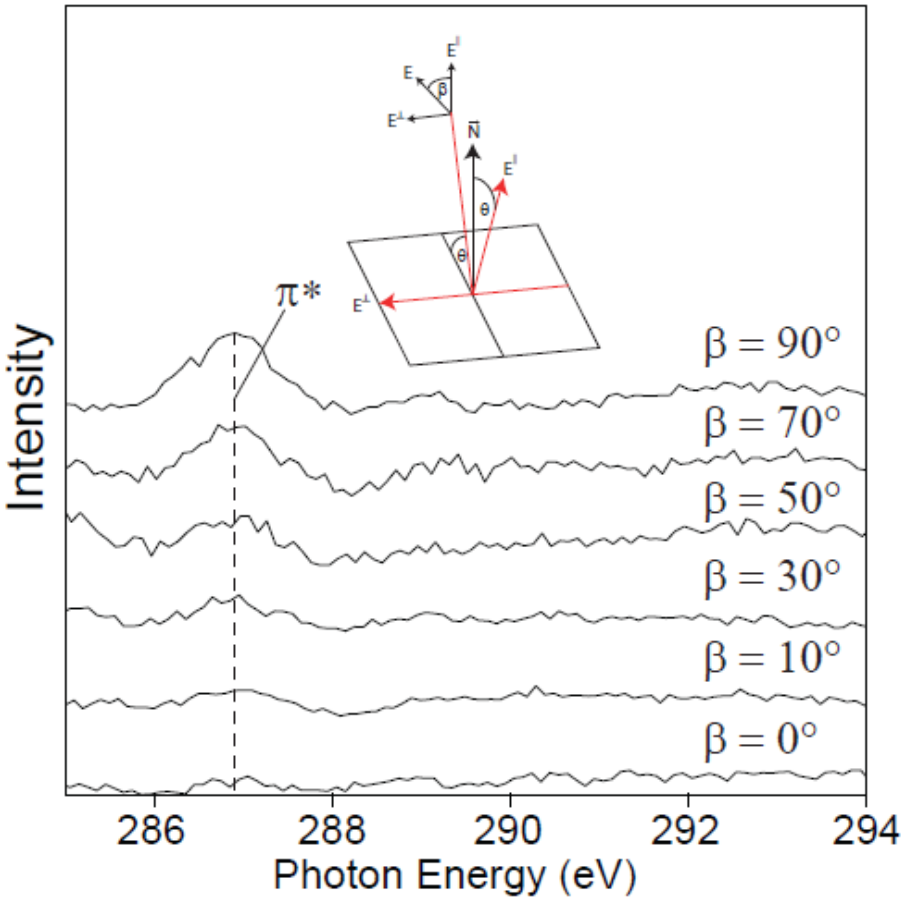

Fig 4.13: *C K-edge difference spectra of CO/Pd/TiO_2(110) at various polarisations of the E-vector of the incident beam relative to the surface normal. The π* resonance at 287.8 eV is most pronounced when the E-vector is orientated perpendicular to the surface normal.*

The resonant intensity in response to illumination is dependent on the orientation of the electric field vector ***E*** of the incident beam, relative to the orientation of the molecule. The experimental setup is depicted via a schematic in figure 4.14. The normal vector of the π* plane orbital ($\mathbf{O}_{CO,\pi^*}$) that runs parallel to the C-O bond axis has a direction of $(1,\gamma,\phi)$ (in spherical form),

where γ is the angle between ($\mathbf{O}_{CO,\pi^*}$) and the surface normal **N**, and ϕ is the azimuthal rotation of ($\mathbf{O}_{CO,\pi^*}$) out of the path of the incident beam. The photon beam is incident on the surface plane at angle θ.

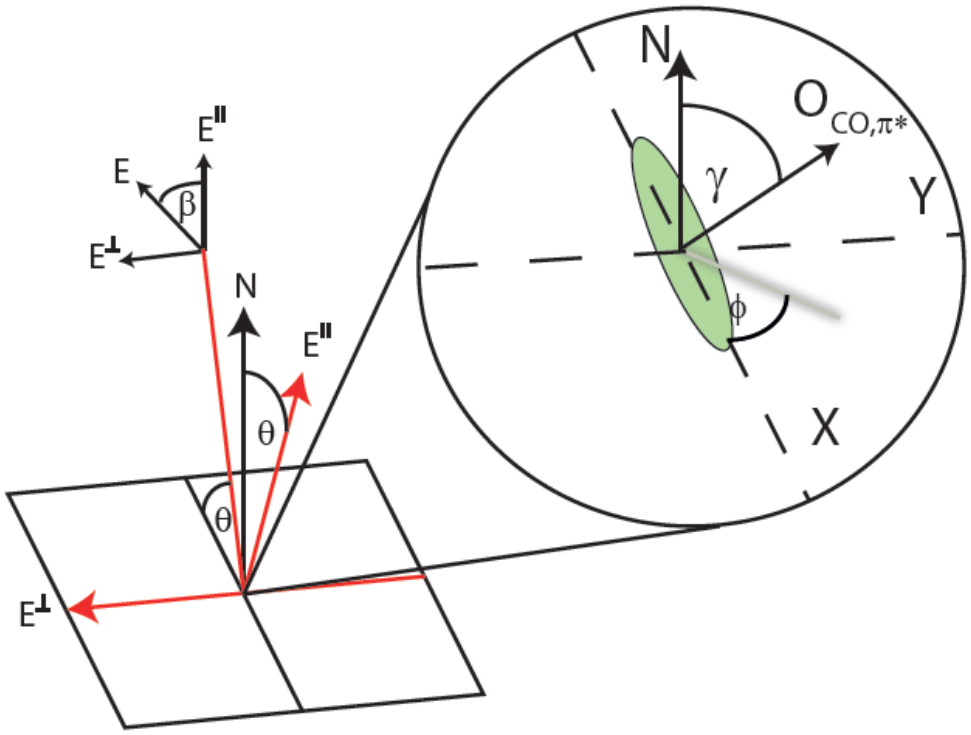

Fig 4.14: *Schematic of the NEXAFS experiment. The electric vector, E of the synchrotron radiation, incident at an angle,* θ *is decomposed into two directional vectors.* $E^{\parallel}$ *is parallel to the orbit plane of the synchrotron ring and* $E^{\perp}$*is perpendicular. As E is rotated through angle* β*, The* $E^{\parallel}$ *and* $E^{\perp}$ *contributions to the illumination of the surface, are varied, producing a unique quantitative electron yield response to irradiation. By comparing the relative electron yields at various experimental geometries, the orientation of a plane molecular orbital, represented by a green circle,* $\mathbf{O}_{CO,\pi^*}$ *that can be described by its angular tilt away from the surface normal* ***N****,* γ *and its angular twist out of the path of the beam,* ϕ*, can be elucidated.*

Initially, it is assumed that the total transition yield is composed entirely of events occurring at the (111) basal plane of the nanoparticles. The orientation can be determined using the following equation;

$$I = C[\cos^2\beta I^{\parallel} + \sin^2\beta\, I^{\perp}] \quad (4.3)$$

Where I is the total π* resonance intensity, C is an arbitrary constant, β the polarisation angle of the incident photon beam measured from the plane of incidence and, $I^{\parallel}(I^{\perp})$ the π* resonance arising in response to illumination by the component of the *E*-vector of the incident photon beam that runs parallel (perpendicular) to the plane of incidence. Note that when β = 0° (90°), the light incident on the basal plane of the nanoparticle is p-(s-) polarised.

Equations designed by Stöhr and Outka describe the intensity components [30], $I^{\parallel}$ and $I^{\perp}$. These components are dependent on the nature of the investigated transition and the rotational symmetry in the surface plane of the substrate. In this experiment when CO is introduced to the (111) termination of a Pd nanoparticle, a π* plane bond to a surface with three-fold rotational symmetry is formed. The individual components of the total intensity yield are decomposed into components describing the geometry of the experiment and the orbital of interest [30]:

$$I^{\parallel} = \frac{2B}{3}\left[1 - \frac{1}{4}(3\cos^2\theta - 1)(3\cos^2\gamma - 1)\right] \quad (4.4\text{ a})$$

And

$$I^{\perp} = \frac{B}{2}(1 + \cos^2\gamma) \quad (4.4\text{ b})$$

In the above equations, θ is the angle of incidence measured from the surface plane, γ is the angular separation between the plane normal of the CO π^* ($\mathbf{O}_{CO,\pi^*}$) and the surface normal (**N**). The azimuthal dependence is averaged out over the three-fold rotational symmetry of the substrate and is therefore not represented by a component. It should be noted that B is an arbitrary constant that is absorbed by the other arbitrary constant C in equation 4.3.

The measured C 1s → 2π* transition dependence on the angular separation of the *E*-vector and the incidence plane is plotted in figure 4.15. Red dots represent data acquired experimentally and superimposed is a numerical fit of the data created using equations 4.3 and 4.4. The best fit value to the experiment as displayed on the figure is $\gamma = 23.8 \pm 4.8°$. In a similar study Yim *et al* [25] determined the bond angle of CO molecules bonded to Pd nanoparticles on a TiO_2(110) substrate to be $\gamma = 14.2 \pm 22.1°$. Both our and Yim *et al's* results are in poor agreement of that of Woodruff's group [31]. In this experiment, the orientation of furan (C_4H_4O) on a Pd(111) single crystal was studied with NEXAFS. Following adsorption at room temperature, CO molecules were formed on the surface as one of the dissociated products. The molecules were found to orient themselves vertically on this surface.

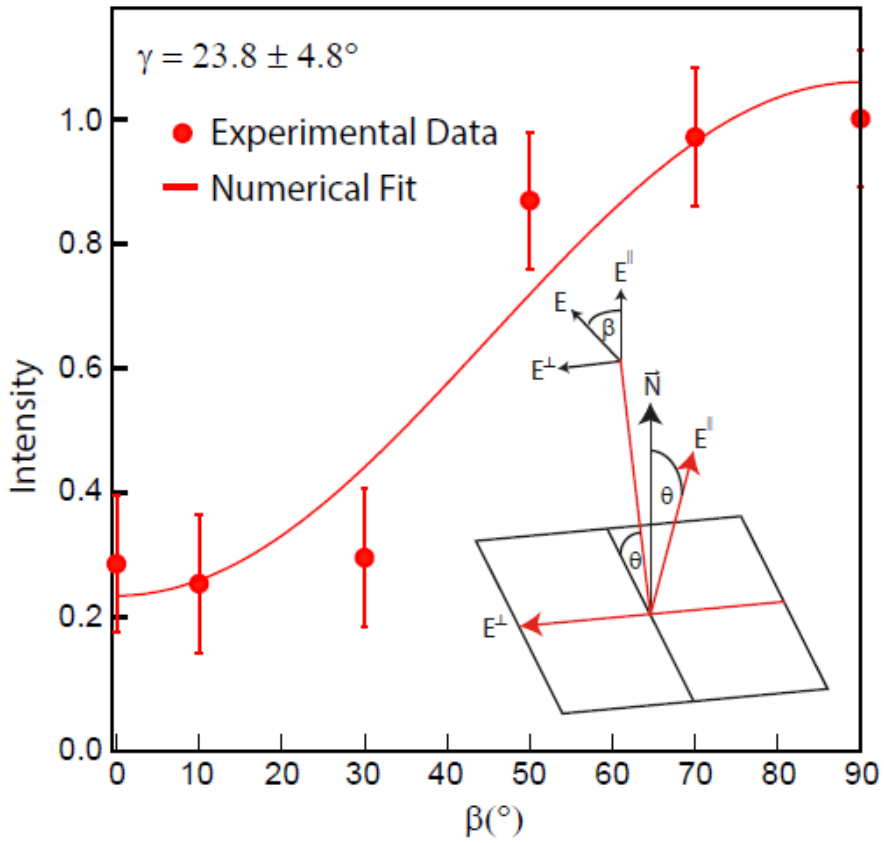

Fig 4.15: *Plot of dependence of intensity (normalised between 0 and 1) of the secondary electron π* resonance on the angle of the electric vector of the incident X-ray beam, the red line represents a fit based on equation 4.3 which returns a value for γ (the angle between the surface normal and the molecular orbital) of 23.8 ± 4.8°.*

A simulation of the C 1s → 2π* intensity arising from a CO molecule on a surface with threefold rotational symmetry (such as has the Pd(111) plane) in response to illumination in a given experimental geometry and its dependence on the angular displacement from the incidence plane is superimposed in figure 4.16. Compared with the curve fitted to the experimental data (red line), the simulated curve (black line) has a steeper decline to a lower intensity.

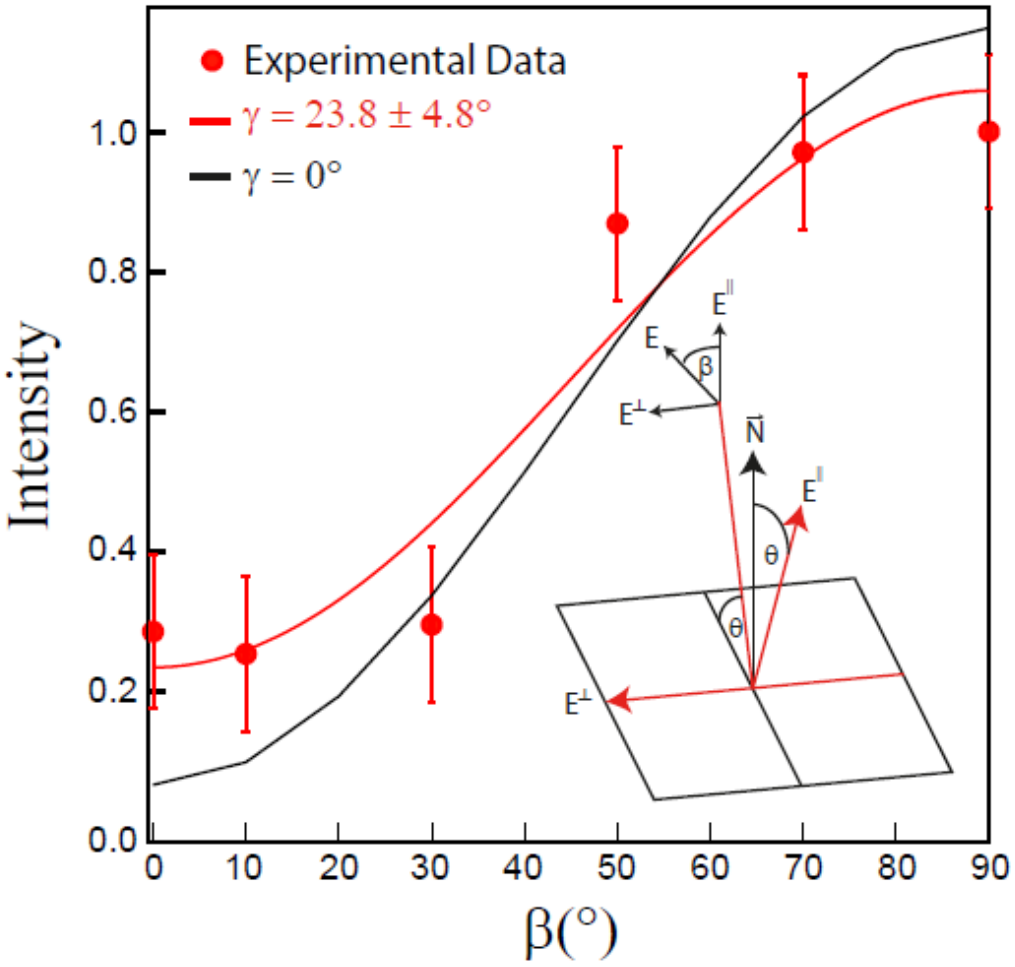

Fig 4.16: *Calculated C≡O π* resonance peak intensity as a function of the polarisation angle of the incident photon beam (β) (black line), superimposed against the numerical fit (red line) of the experimental data (red dots) using equations (4.4a and 4.4b) adapted from the equations of Stohr and Outka [30]. The numerical fit delivers an angular separation of 23.8 ± 4.8°. The simulation was carried out by calculating variation in the C≡O π* resonance peak with β for a CO molecule is bonded upright on the threefold symmetric Pd(111) surface.*

This discrepancy could be explained by the multifaceted nature of the nanoparticle; from STM studies of Pd/MoS_2 [32], $Pd/Al_2O_3/NiAl(110)$ [33] and Pd deposited on graphite [34], it is understood that the morphology of supported (111)-terminated Pd nanoparticles is a truncated tetrahedron exposing (111) and (100) side facets as in figure 4.17.

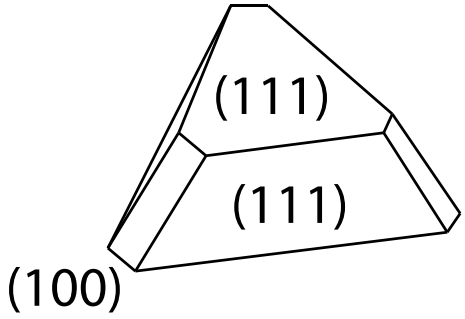

Fig 4.17: *Schematic representation of frequent morphology of Pd nanocrystal grown epitaxially on the basal plane of TiO_2(110), formed from a tetrahedron exposing (111) facets and (100) facets. Adapted from* [35].

CO will adsorb to the {111} and {100} prism facets and it is likely that these faces are large enough that their adsorbed CO molecules will contribute to the total x-ray absorption yield at the C K-edge. Previous studies have shown that CO bonds vertically to both the Pd(111) [31] and the Pd(100) [35] single crystals. Extending these results to the expected morphology of the Pd nanoparticles in this study, a significant contribution to the total signal will come from CO molecules that, while bound vertically to the prism facets, are not orientated vertically relative to the substrate basal plane that is the origin of defined geometry of the experiment.

Furthermore, the results of Yim *et al* are closer to the result of Woodruff's *et al*. In Yim *et al*'s study the surface was 90% covered in Pd so it is possible that adjacent nanoparticles shield the prism facets of their neighbours from the photon beam, a greater proportion of the total yield may come from molecules adsorbed to the basal termination of the nanoparticles, compared with our study where the nanoparticles have separations of the order of microns, laterally.

A second attempt to grow nanoparticles was carried out with the substrate held at 925 K. The sample was dosed with 120 L of CO after well-defined Pd nanoparticles of the order of 100 nm

were established to be present on the surface. C K-edge NEXAFS spectroscopy of the system failed to exhibit the π^* resonance demonstrating that the Pd nanoparticles had likely been encapsulated. TiO_{2-x} can encapsulate Pd nanoparticles of a thickness of the order of 100 nm at temperatures of 900-925 K [4-6].

4.5 Summary

The adsorption and orientation of CO molecules bonded to Pd nanoparticles supported on a TiO_2(110) substrate have been studied using XPEEM and μ-NEXAFS. The presence of Pd nanoparticles on the surface was also confirmed by chemically sensitive, spatially-resolved XPEEM imaging and by a faint Pd(111) signature in LEED.

After well-defined Pd nanoparticles were formed, the bonding orientation of CO on one of the nanoparticles was studied by carbon K-edge μ-NEXAFS measurements. With the angle of incidence fixed, the C-O π^* resonance intensity as a function of the polarization angle (β), which corresponds to the direction of the electric field vector $\boldsymbol{E}$ of the incident photon beam, was measured. This, combined with numerical fitting using the appropriate equations from Stöhr and Outka's paper [30], suggests that CO bonds at a polar angle of $23.8^\circ \pm 4.8^\circ$ away from the nanoparticle's normal. By comparing our result with that of Woodruff's group [31], we propose that CO on the side-facets of the Pd nanoparticles also contribute to the X-ray absorption signal, hence giving an apparent off-normal orientation of CO.

References

[1] C. R. Henry, *Surface Science Reports*, **31** (1998) 231.

[2] M. Bowker, P. Stone, R. Bennett and N. Perkins, *Surface Science*, **497** (2002) 155.

[3] S. Jacinto, J. Bernardi and J. A. Anderson, *Catalysis Letters*, **114** (2007) 91.

[4] S. J. Tauster, S. C. Fung and R. L. Garten, *Journal of the American Chemical Society*, **100** (1978) 170.

[5] S. J. Tauster and S.C. Fung, *Journal of Catalysis*, **53** (1978) 29.

[6] M. Bowker, P. Stone, P. Morrall, R. Smith, R. Bennet, N. Perkins, R. Kvon, C. Pang, E. Fourre and M. Hall, *Journal of Catalysis*, **234** (2005) 172.

[7] C. T. Campbell, *Surface Science Reports*, **27** (1997) 1.

[8] P. Gunter, J. Niemantsverdriet, F. Ribiero and G. A. Somorjai, *Catalysis Reviews*, **39** (1997) **77.**

[9] M.Boudart, *Topics in Catalysis*, **13** (2000) 147.

[10] I. Z. Jones, R. A. Bennett and M. Bowker, *Surface Science*, **439** (1999) 235.

[11] C. Xu, X. Lai, G. W. Zajac and D. W. Goodman, *Physical Review B*, **56** (1997) 13464.

[12] M. J. J. Jak, C. Konstapel, A. van Kreuningen, J. Chrost, J. Verhoeven and J. W. M. Frenken, *Surface Science*, **474** (2001) 28.

[13] U.Diebold, *Surface Science Reports*, **48** (2003) 53.

[14] P.A. Stone *Chemical Communications*, **13** (1998) 1369.

[15] D. S. Humphrey, G. Cabailh. C. L. Pang, C. A. Pang, C. A. Muryn, S. A. Cavill, H. Marchetto, A. Potenza. S. S. Dhesi and G. Thornton, *Nano Letters*, **9** (2009) 155.

[16] D.F. Ogletree, M.A. Van Hove and G.A. Somorjai, *Surface Science*, **173** (1986) 351.

[17] F.M. Hoffmann, *Surface Science Reports*, **3** (1983) 107.

[18] H. Conrad, G. Ertl, J. Koch and E.E. Latta, *Surface Science*, **43** (1974) 462.

[19] S.S. Dhesi, S.A. Cavill, A.Potenza, H.Marchetto and R.A. Mott, *AIP Conference Proceedings*, **1234** (2010) 311.

[20] F. Atamny, J. Blocker, B. Henschke and R.Scholgl, *Journal of Physical Chemistry*, **96** (1992) 4522.

[21] E.M. McCash, *Surface Chemistry* (2007) Oxford University Press

[22] J. J. Yeh and I. Lindau, *Atomic Data and Nuclear Data Tables*, **32** (1985) 1.

[23] A. Locatelli and E. Bauer, *Journal of Physics: Condensed Matter*, **20** (2008) 93002.

[24] A. Thompson, I. Lindau, D. Attwood, P. Pianetta, , E. Gullikson, A. Robinson, M. Howells, J. Scofield, K.J. Kim, J. Underwood, J. Kirz, D. Vaughan, J. Kortright, G. Williams and H. Winick, *X – ray Data Booklet*, Lawrence Berkeley National Laboratory (2009)

[25] C.M. Yim, C.L. Pang, D.S. Humphrey, C.A. Muryn, K. Schulte, R. Perez and G. Thornton, *Faraday Discussions*, **162** (2013) 191.

[26] A. Linsebigler, G. Lu and J.T. Yates Jr, *Journal of Chemical* Physics, **103** (1995) 9438.

[27] P. Marchand and L. Marmet, *Review of Scientific Instruments*, **54** (1983) 1034.

[28] D. Cappus, J. Klinkmann, H. Kuhlenbeck and H.J. Freund, *Surface Science*, **325** (1995) 421.

[29] D. Lovric, B. Gumhalter and K. Wandelt, *Surface Science*, **278** (1992) 1.

[30] J. Stohr and D.A. Outka, *Physical Review B*, **36** (1987) 7891.

[31] M.J. Knight, F. Allegretti, E.A. Kröger, M. Polcik, C.L.A. Lamont and D.P. Woodruff, *Surface Science*, **602** (2008) 2743 .

[32] C. Chapon, S. Granjeaud, A. Humbert and C.R. Henry, *European Physical Journal*, **E13** (2001) 23.

[33] A. Piednoir, E. Perrot, S. Granjeaud, A. Humbert, C. Chapon and C.R. Henry, *Surface Science*, **391** (1997) 19.

[34] K. Hojrup-Hansen, T. Worren, S. Stempel, E. Laegsgaard, M. Baumer, H.J. Freund, F. Besenbacher, I. Stensgaard, *Physical Review Letters*, **83** (1999) 4120.

[35] R.J. Behm, K. Christmann, G. Ertl and M.A. Van Hove, *Journal of Chemical Physics*, **73** (1980) 2984.

Chapter 5: APPES and APNEXAFS Studies of $CH_3COO^-/TiO_2(110)$

5.1 Introduction

Among the multitude of technological applications of TiO_2, its photo-activity and consequent potential for solar power generation is especially attractive to industry. UV-irradiation of the $TiO_2(110)$ surface can create an electron-hole pair and the subsequent chemical or electron transfer reactions are central to TiO_2 based photo-devices [1]. TiO_2 has a relatively wide band-gap (~3 eV) and does not absorb sunlight particularly well [1]. The sensitivity of TiO_2 solar devices to sunlight is improved by the addition of a dye to the surface [2-5]. Indeed, the most efficient example of a commercial solar cell is the dye-sensitized Grätzel cell with power conversion efficiencies of up to 11% under direct sunlight reported [6].

Particularly important to the dye-sensitisation process are carboxylate moieties that are contained within the organic dyes as an effective means of binding them strongly to the surface of the metal-oxide [7-10]. Here acetate is used as a mimic of such a carboxylate moiety. In the presence of the $TiO_2(110)$ surface, acetic acid undergoes deprotonation to form the acetate anion. This anion adsorbs to the $TiO_2(110)$ surface via the bonding of the molecule's two carboxylate oxygen atoms to two Ti^{4+} sites on the surface. The dissociated hydrogen atom forms hydroxyls on the $TiO_2(110)$ surface [11]. Saturation coverage of acetate occurs at 0.5 ML (i.e. all Ti^{4+} $TiO_2(110)$ surface sites are filled) [11].

The mechanism of the bonding of acetate to the TiO_2(110) surface is well-characterised under ultra-high vacuum (UHV) conditions. Novel phenomena can occur under atmospheric conditions, however and UHV studies can therefore sometimes only provide a limited description of a catalyst [12-15]. This limitation is often referred to as the 'pressure gap'.

In the following study, a TiO_2(110) single crystal is held under acetic acid pressures ranging from UHV (~10^{-10}) to 10^{-1} Torr and the extent of coverage and the orientation of the adsorbed molecules are examined with ambient-pressure photoemission spectroscopy (APPES) and near-edge X-ray absorption fine structure (AP-NEXAFS). The TiO_2(110) surface is very well-characterised and thus an excellent substrate for the exploration of new phenomena [1].

5.2 Experimental

The experiment was carried out on beamline 11.0.2 (See Chapter 3) at the Advanced Light Source (ALS) [16]. This beamline utilises linear and circular polarised light from an undulator with a 5 cm period [17] and can produce photons over a wide energy range (75 – 2150 eV). The energy of the incident beam can be changed via an SX700 style monochromator [18] that is equipped with two gratings (150 and 1200 lines/mm). The monochromator stigmatically focuses the photons at the exit slits of either the STXM or the spectroscopy branchline. The branchline is selected by moving the spectroscopy mirror.

The APPES end-station was utilised in this experiment. The spectrometer facilitates the study of samples under pressures of up to 10 Torr. The sample chamber and the beamline are

separated by a 1 × 1 mm^2, 100 nm thick silicon nitride window. The sample is held approximately 0.5 mm from the entrance to the hemispherical analyser. Minimising the distance between the sample and the aperture through which photo-generated electrons pass in to the hemispherical analyser is crucial. Above the millibar pressure range the mean free path of an electron with kinetic energy of the order of 100 eV is less than 1 mm [16].

Electrons photo-excited from the sample are focused using a series of electrostatic lenses through three differential pumping stages before being finally focused on an aperture that is the entrance to the hemispherical analyser. A pressure difference of up to 8 orders of magnitude can be maintained between the sample chamber and the hemispherical analyser. This facilitates the experimental scrutiny of samples held under ambient pressure by sensitive equipment that must operate under UHV conditions [16].

A rutile TiO_2(110) sample (*Pi-Kem*) was prepared by cycles of Ar^+ sputtering and annealing to 1000 K until a sharp (1 × 1) low energy electron diffraction (LEED) pattern was observed and no contaminants were detected in PES. 100 L (1 Langmuir = 1×10^{-6} Torr.s) of acetic acid was dosed at 1×10^{-6} Torr onto the as-prepared TiO_2 sample through a leak valve until saturation coverage of 0.5 monolayers (ML) was confirmed by the observation of a (2 × 1) pattern in LEED. The chemical nature and the orientation of the adsorbed acetate molecules on the surface were then examined using PES and NEXAFS respectively.

This experimental procedure was repeated with pumping to the chamber discontinued and C 1s and O 1s core-level spectra were recorded at photon energies of 395 eV and 735 eV respectively to monitor the coverage of acetic acid on the sample that was held at partial acetic

acid pressures between 10^{-5} and 10^{-1} Torr. In addition, Ti $L_{2,3}$-edge resonant valence band PES spectra were collected to study changes to the defect peak under these conditions. The binding energy of all PES spectra presented here were calibrated with respect to the central position of the O 1s peak originating from the O^{2-} ions of the TiO_2(110) surface [19], which was considered to be the best reference point.

Carbon K-edge (hv = 275 – 320 eV) AP-NEXAFS measurements were recorded together with PES measurements to determine the bonding orientation of acetate/acetic acid molecules on the TiO_2(110) surface at various coverages. Change of the peak intensity of the $2b_2$ resonance as a function of the orientation of the electric field vector of the incident photon beam were measured. Data were collected at two angles of incidence, allowing the polar and azimuthal angular orientations of the adsorbate molecules to be determined. AP-NEXAFS measurements were taken in Auger-yield mode (AEY), which was chosen due to its superior surface sensitivity [20].

5.3 The As-prepared TiO_2(110) Surface

Figure 5.1 displays a PES survey scan of the as-prepared TiO_2(110) surface recorded at an incident photon energy of 735 eV. This scan revealed no other elements than Ti and O. It was very important to ensure that no carbon was present on the surface initially as variations in the C 1s peak would be used to determine the coverage and chemical nature of acetic acid molecules adsorbed on the TiO_2(110) surface in this experiment.

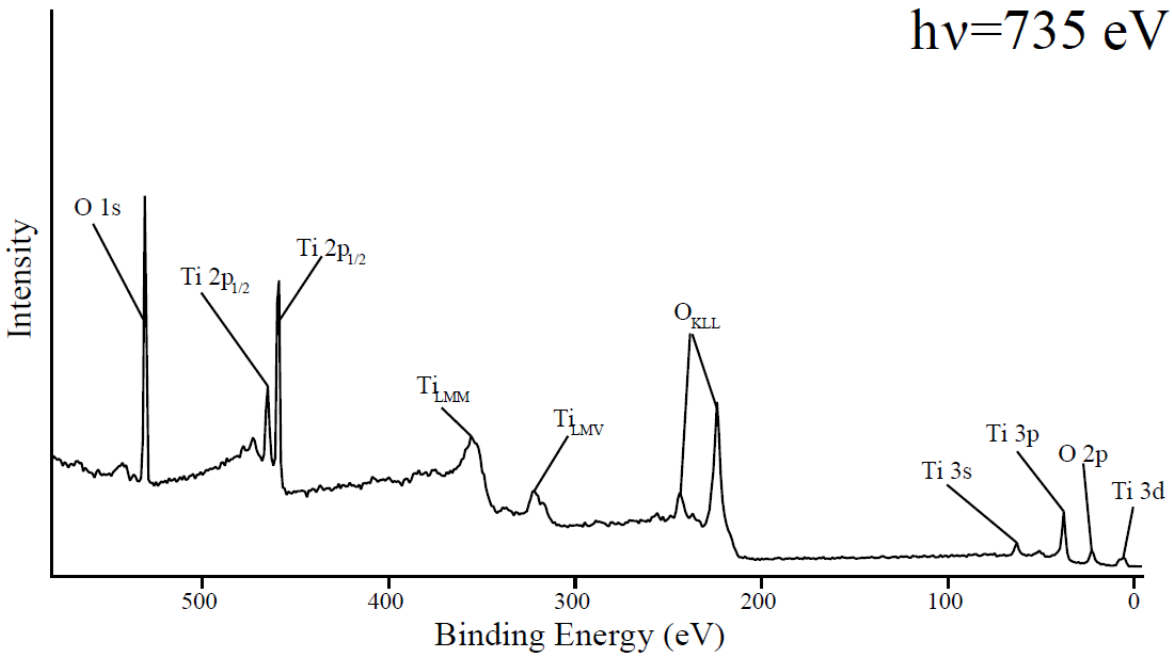

Fig 5.1: *PES survey scan of as-prepared TiO_2(110) (hv = 735 eV) showing peaks attributed to no other elements than oxygen and titanium.*

Figure 5.2 shows an O 1s photoemission spectrum of as-prepared TiO_2(110), recorded at an incident photon energy of 735 eV. The spectrum is composed of two peaks, a significant peak at 530.4 eV that is attributed to the contribution of Ti-O in TiO_2(110) in various chemical environments, consistent with prior studies [21-23]. A minority peak at 531.3 eV constitutes 12.71 % of the region and is a result of hydroxyl groups formed on the surface [22].

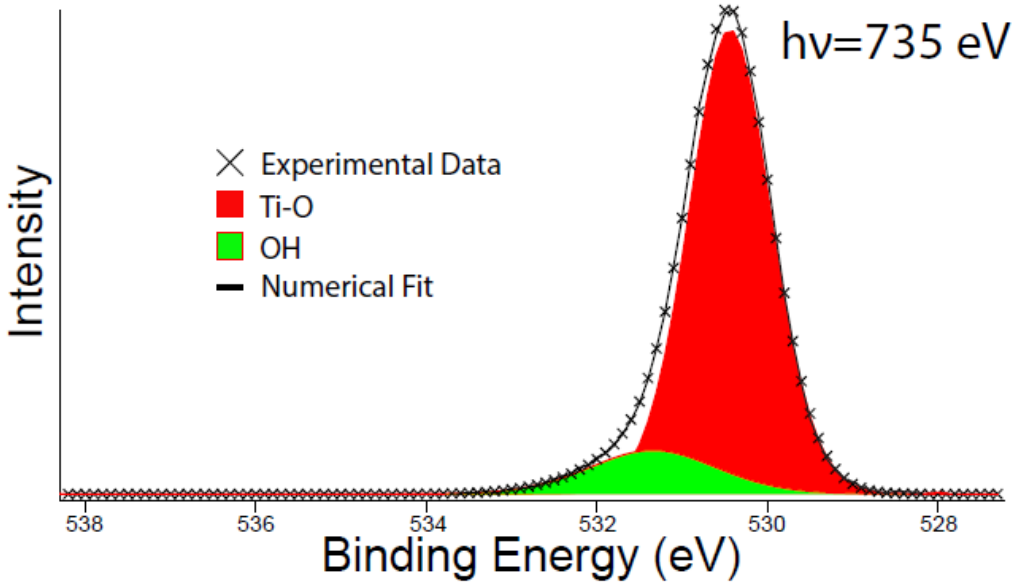

Fig 5.2: *O 1s photoemission spectrum recorded from an as-prepared TiO_2(110) surface taken at incident photon energy of 735 eV. Crosses are experimental data and solid lines are the numerical fits to the experiment data. Numerical fitting reveals two peaks: a main peak at a binding energy (BE) of 530.4 eV corresponds to contributions from O ions in the TiO_2(110) substrate (highlighted in red), and a minor peak at BE = 531.3 eV arises from O atoms in the bridging hydroxyl groups (OH_b) (highlighted in green).*

5.4 CH_3COO^- Adsorption on TiO_2(110)

100 L of CH_3COOH was admitted to the chamber and saturation coverage (0.5 ML) of acetate on the TiO_2(110) sample was confirmed by the appearance of a (2 × 1) pattern in LEED such as displayed below in figure 5.3 [24].

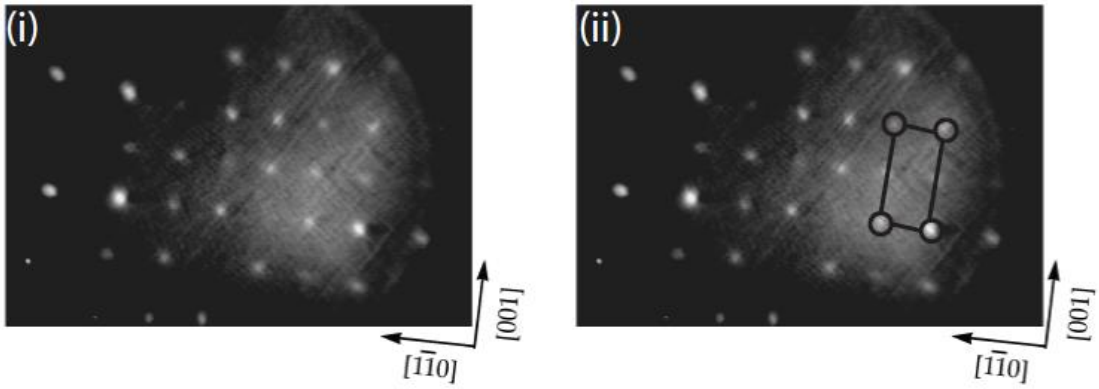

Fig 5.3: *(i) Low energy electron diffraction (LEED) pattern (electron energy = 177 eV) recorded from a TiO_2(110) surface following a saturation dose (0.5 ML) of acetic acid at 300 K, giving rise to an additional set of (2×1) diffraction spots. (ii) As (i), with the unit cell of the TiO_2(110) substrate in reciprocal space highlighted. Adapted from* [24].

C 1s and O 1s spectra of TiO_2(110)-2×1(CH_3COO^-) recorded at photon energy 395 eV and 735 eV, respectively are presented in figure 5.4. The C 1s spectrum is characterised by two peaks from the methyl carbon (CH_3) and carboxylate carbon (COO^-) at 285.9 eV and 289.3 eV, respectively. The observed separation between the two peaks (3.4 eV) is similar to that observed in PES experiments where Si(110)-(2 × 1) and Ge(001)-(2 × 1) substrates were exposed to gaseous acetic acid [25, 26].

In the O 1s spectrum in Fig. 5.4 (ii), the peak at 532.1 eV is a mixture of two O 1s peaks corresponding to the carboxylate group (two O atoms in COO^-) and bridging hydroxyls (OH_b), formed following the dissociation of the acid hydrogen atom from acetic acid [11]. The energy separation between the TiO_2(110) main peak and the COO/OH peak is observed to be 1.8 eV.

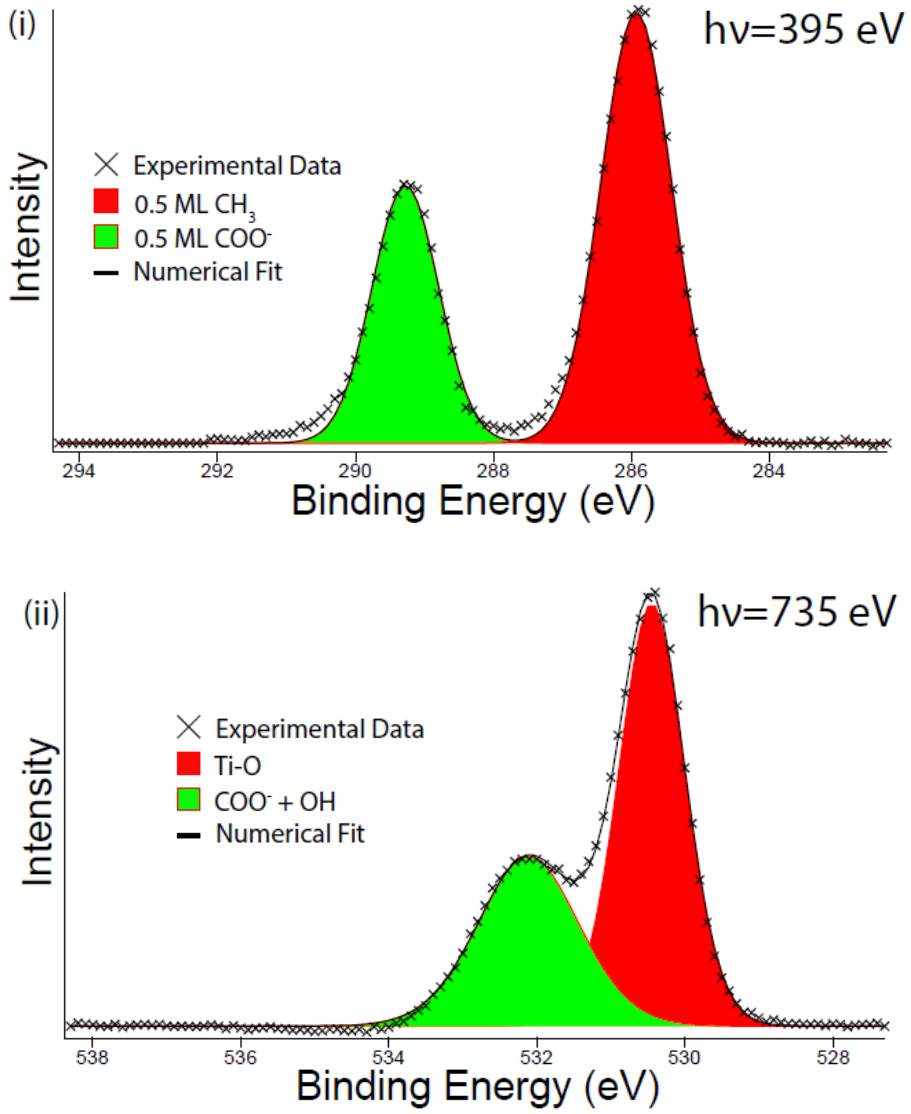

Fig 5.4: *(i) C 1s and (ii) O 1s photoemission spectra from TiO_2(110)(HCOO)-2×1 recorded at incident photon energies of 395 eV and 735 eV, respectively. Crosses are the experimental data and solid lines are the numerical fits to the experimental data. In (i), the peak at BE = 285.9 eV is comprised of C atoms in the carboxylate (-COO^-) group of the acetate ions (highlighted in red), while that observed at 289.3 eV arises from C atoms contained in the methyl (CH_3-) group (highlighted in green). In (ii), apart from the substrate O 1s peak at BE = 530.4 eV (highlighted in red), an additional peak centred at BE = 532.3 eV, arises (highlighted in green) from the dual oxygen atoms bonded to a carbon atom to make the carboxylate group of the ion. This peak is heavily convoluted with the peak pertaining to surface hydroxyls described in figure 5.2, which is also expected to increase due to the formation of further OH_b, following the adsorption of acetate.*

Then, the same photoemission measurements were performed at increased acetic acid partial pressures. As shown in Fig. 5.5, as the partial pressure reaches 10^{-5} Torr, two extra peaks,

which are respectively located at higher binding energy next to the C 1s peaks associated with the first half-monolayer of acetate, appear and increase in intensity with increasing partial pressure. These peaks are thought to describe a more weakly absorbed second layer of acetic acid. Ottosson et al. reported that acetic acid and acetate can be differentiated by a relative difference in their C 1s peak positions [27], that the excess negative charge of the acetate caused a negative shift in binding energy. At partial pressures above 10^{-2} Torr, two additional C 1s peaks are observed. The peaks are thought to originate from acetic acid molecules that are in the gas-phase. These are significantly shifted as their energy position is defined relative to the vacuum level.

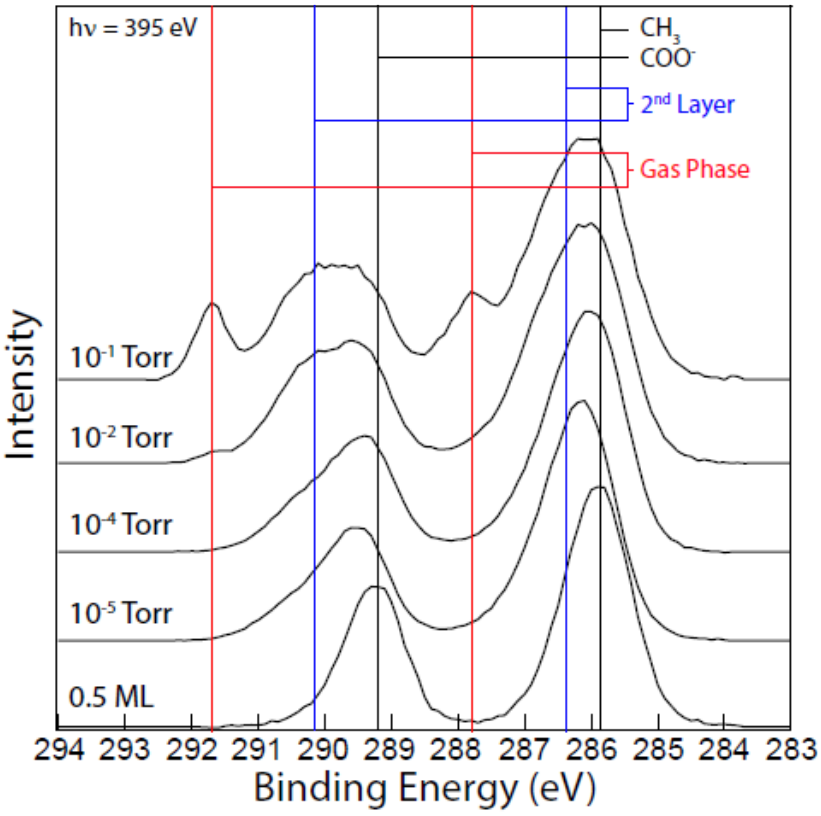

Fig 5.5: *C 1s photoemission spectra recorded from the TiO_2(110) surface initially covered with 0.5 ML CH_3COO^-, before the surface was monitored as the preparation chamber was back-filled with increasing partial pressures of acetic acid. All spectra were collected using an incident photon energy of 395 eV. At increased pressure, shoulder peaks (their positions marked with blue lines) representing methyl and carboxyl C 1s PES electron yield emergent from a second layer of acetic acid on the surface are evident at higher binding energy than their respective peak arising from the first 0.5 ML. These shoulder peaks increase with the pressure in the chamber and at 10^{-2} Torr an additional pair of peaks appear that are ascribed to acetic acid molecules in the gas phase.*

To verify this, a C 1s photoemission spectrum from acetic acid molecules in the gas phase was recorded at a background pressure of 10^{-1} Torr. This spectrum is shown in Fig. 5.6 to exhibit a methyl carbon peak at 287.4 eV and a carboxyl carbon peak at 291.2 eV. These peak positions are in very good agreement with those associated to the additional peaks observed at 10^{-1} Torr in figure 5.5, confirming their gas-phase character. The energy separation between the methyl- and carboxyl- peaks associated with the acetic acid gas phase was measured to be 3.8 eV which is in agreement with previous studies [28].

The relative intensities of the methyl- and carboxyl- peaks in the C 1s spectrum are noteworthy. The intensities of the methyl- and carboxyl- peaks of the gas-phase acetic acid molecules were measured to be within 10 % to each other. An equal intensity between two peaks was expected for the gas phase acetic acid molecules that are orientated randomly and have no preferential orientation towards the energy analyser. Following adsorption, the methyl- C 1s peak is almost double the intensity of the carboxyl C 1s peak. This has been observed in another study of acetic acid adsorption [29] where it was postulated that adsorbed acetic acid molecules have a preferred orientation relative to the surface; if the methyl group is oriented towards the vacuum while the carboxyl group is oriented towards the sample, electrons excited from the carboxyl group could experience more scattering losses [29].

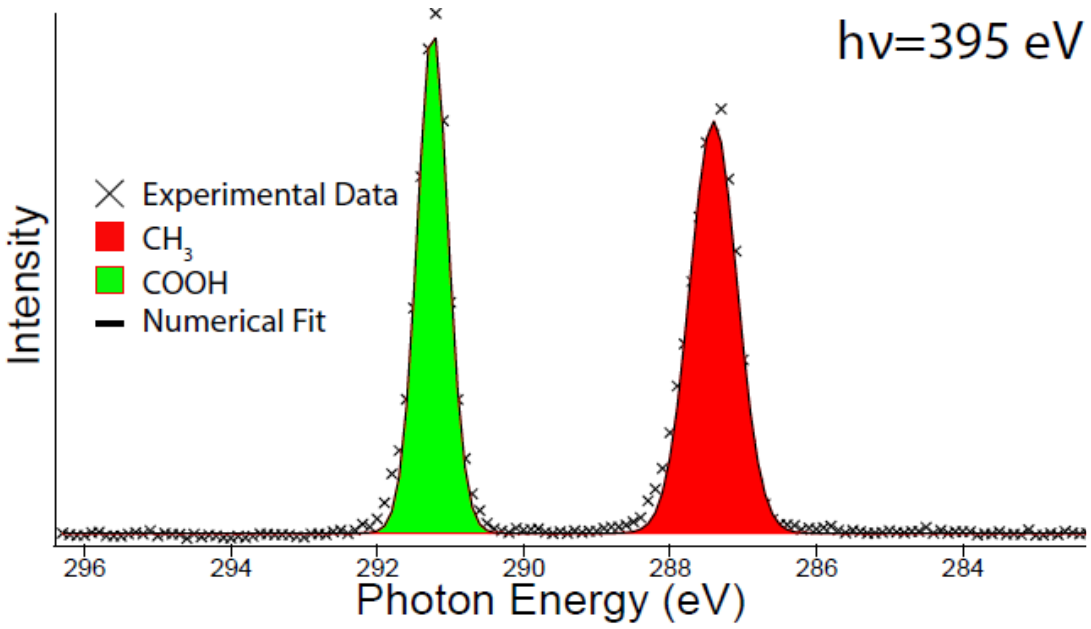

Fig 5.6: *C 1s photoemission spectrum of acetic acid molecules in the gas phase, recorded at incident photon energy of 395 eV. The spectrum consists of two peaks; one at BE = 287.4 eV is attributed to the methyl- carbon and another at BE = 291.2 eV to the carboxyl- carbon. In the gas phase, the intensity ratio between the methyl- and carboxyl- C 1s peaks was determined to be close to unity, which is in contrast to those determined from the adsorbed species in the first and second adsorbate layer respectively. This suggests that the adsorbed species in the first and second adsorbate layer have preferred orientations relative to the surface.*

Plotting the spectra obtained with different partial pressures together as in figure 5.5 represents only a rudimentary examination of the system. Quantitative analysis was carried out to elucidate the extent of the coverage of the second layer of acetic acid in figure 5.7. To estimate the coverage of acetate/acetic acid in different adsorbate layers; Firstly, Gaussian/Lorentzian (70/30) peaks were fitted to (i) (green and red). Secondly, peaks were fitted to (ii),(iii),(iv),(v) at the same peak positions and with the same separation and intensity ratio between the peaks to represent the first layer's extent in each spectrum. Thirdly, a second set of peaks were fitted to (ii),(iii),(iv) and (v) at different positions but with the same peak separation and relative intensity as (i). These peaks (blue) represent the second layer of adsorbate. Finally, peaks were fitted to the gas phase features evident in (iv) and (v) (purple). It is known that the first layer represents 0.5 ML [28], so coverage is determined via an average of the ratio of the methyl-

and carboxyl- peaks of the second to the first layer. The quoted error is the difference between these ratios.

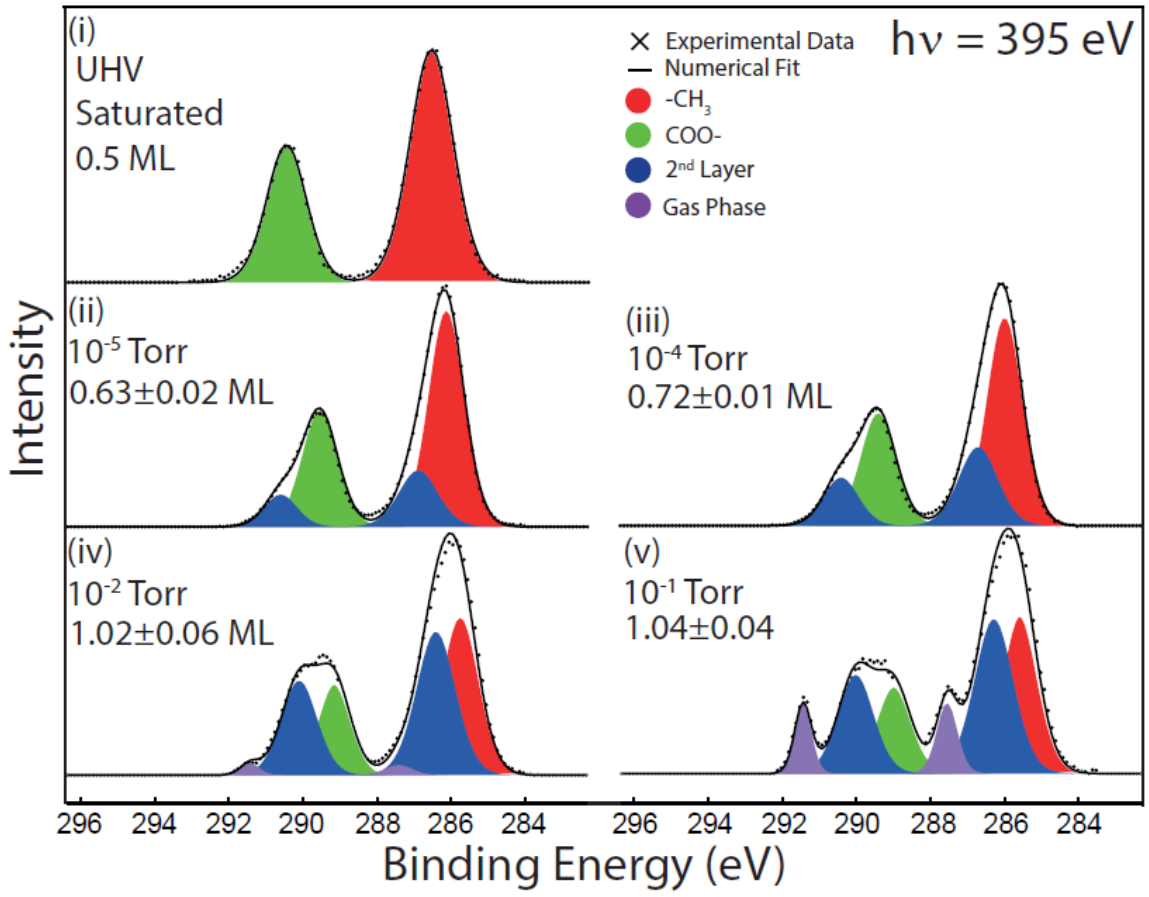

Fig 5.7: *Carbon 1s photoemission spectra obtained from (i) the TiO_2(110) surface following saturation with 0.5 ML acetic acid and additionally, from the same surface held under increased acetic acid partial pressure: (ii) 10^{-5} Torr, (iii) 10^{-4} Torr, (iv) 10^{-2} Torr and (v) 10^{-1} Torr. Crosses are the experimental data and solid lines are the numerical fits to the experimental data.*

The coverage increases steadily as a function of pressure before the second layer saturates at a coverage of 0.5 ML. The ~2:1 ratio of the Gaussian/ Lorentzian C 1s methyl peak intensity to the carboxyl(ate) peak intensity is almost identical to that observed in the first layer. This again suggests that electrons excited from the methyl- carbon undergo fewer scattering losses on their journey to the detector than those from the carboxyl group because the carboxyl group is close to the substrate and the methyl- group is situated in the gas phase [29]. It is proposed that acetic

acid molecules form one O-OH_b bond with a hydroxyl and one OH-O_b bond with a bridging oxygen site on TiO_2(110) and a molecular model of this arrangement is presented in figure 5.8. A second layer orientated relative to the substrate via bidentate hydrogen bonding, sitting slightly higher up than the first layer. This would saturate at 0.5 ML and have the carboxyl group at the surface. These dual phenomena are apparent from our PES analysis. This proposed arrangement is demonstrated using a molecular model in figure 5.8, which is shown at low coverage, for clarity. The orientation of acetic acid depicted in figure 5.8 is notional. Another consideration is that acetic anhydride can be formed from acetic acid [30]:

$$2CH_3COOH \rightarrow (CH_3COO)_2O + H_2O \qquad (5.1)$$

And this reaction could occur, to some extent, at elevated partial pressures.

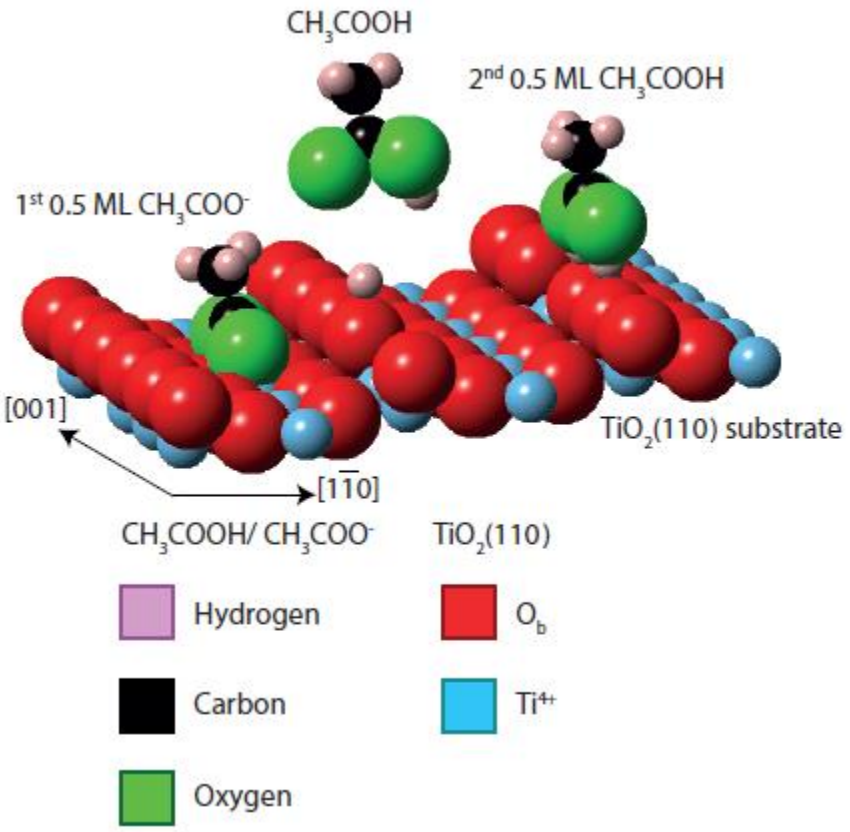

Fig 5.8: *Space-filling ball and stick model describing the well-characterised mechanism by which the acetic acid molecule deprotonates to the acetate ion which then forms two O-Ti covalent bonds with the TiO_2(110) substrate and a proposed model for the bonding mechanism of a second layer of acetic acid to the same surface. The second layer appears when the substrate is held under various partial pressures of acetic acid and is thought to be held to the surface via two hydrogen bonds per molecule. One hydrogen bond is between the acid group of the acetic acid molecule and an O_b site on the substrate and the second hydrogen bond materialises between the non-acid group oxygen atom in the molecule to an OH_b site on the surface, indeed 0.5 ML OH_b are created when the acid hydrogen of the acetic acid 'breaks off' to form the ions constituting the first half-monolayer of acetate on the surface. A low coverage case is presented for illustrative purposes, in reality the first layer is saturated at 0.5 ML prior to the adsorption of the second layer. The depicted orientation of the second layer acetic acid is notional.*

5.5 Effect of Adsorption on the Valence Band

A valence band spectrum of the as-prepared TiO_2(110) substrate, recorded on the Ti $L_{2,3}$ resonance is exhibited in figure 5.9. It is in line with previous studies carried out on this well-characterised surface [31].

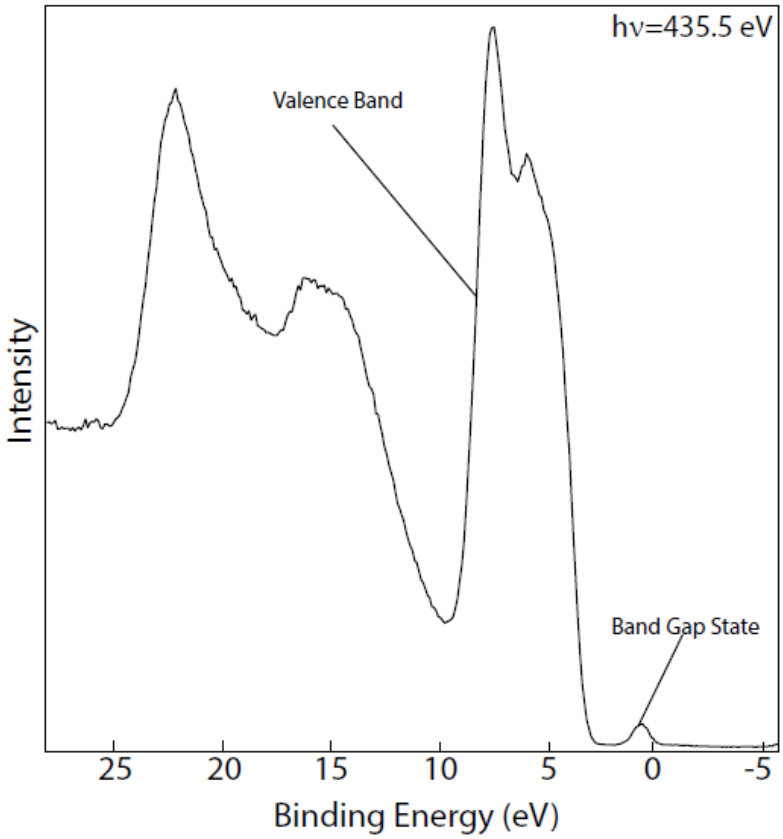

Fig 5.9: *Ti $L_{2,3}$ resonance, photoemission spectrum valence band of TiO_2(110) collected at hν = 435.5 eV.*

The above Ti $L_{2,3}$ resonance photoemission spectrum displays a peak at ~1 eV below the Fermi level (E_F) in the bandgap. The nature of the band-gap state affects the surface chemistry of TiO_2 [32]. At the Ti $L_{2,3}$ absorption edge, a 2p→3d transition occurs and Ti 3d features appear in the spectrum [33]. The band gap state is known to be Ti 3d derived, and indicates the presence of surface bridging oxygen vacancies (O_b-vac) or bridging hydroxyl groups [34]. In addition, two features assigned to hybrid Ti 3d and O 2p valence band states of TiO_2 are centred at 6 and 9 eV [35]. A peak assigned to emission from the O 2s level is apparent at 22 eV [36] and the structure located at 15 eV is assigned as an L $M_{4,5}$ Auger peak for titanium [35].

In fig 5.10 the valence band spectrum of the as-prepared TiO_2(110) surface is co-plotted with that of the same surface following saturation with 0.5 ML of acetate and subsequently

following exposure to intermittently higher sub-atmospheric pressures of acetic acid to demonstrate the evolution of certain features, particularly the defect peak with increasing coverage. Changes to the O 2s peak and the valence band peak, are distinguishable as prominent shoulder peaks that grow as a function of pressure. These shoulders likely stem from the O atoms contained in the acetic acid molecules sticking to the surface in increasing numbers with increasing pressure. The most fascinating and prominent evolvement, however, is that of the Ti 3d defect state peak.

Inset in figure 5.10; initially a function that is a Gaussian(70%)-Lorentzian(30%) product is fitted to the defect peak at 0.8 eV below the E_F (highlighted in red). This peak is initially apparent on the hydroxylated TiO_2(110) ($hTiO_2$(110)) surface before increasing four-fold in intensity upon the saturation of the surface with 0.5 ML of acetate. This might be expected due to the aforementioned OH_b formation on the TiO_2(110) as a consequence of exposure to acetic acid [11]. It has been evidenced that increased OH_b concentration on this surface increases the intensity of the Ti 3d defect peak [37,38].

After the formation of the 0.5 ML covered surface and the pressure of the acetic acid environment encompassing the sample is increased to 10^{-6} Torr, a shoulder peak at 1.5 eV below E_F (highlighted in green) appears. As the partial pressure is raised, the intensity of this shoulder peak enlarges to the detriment of the intensity of the defect peak established on the clean and saturated surfaces.

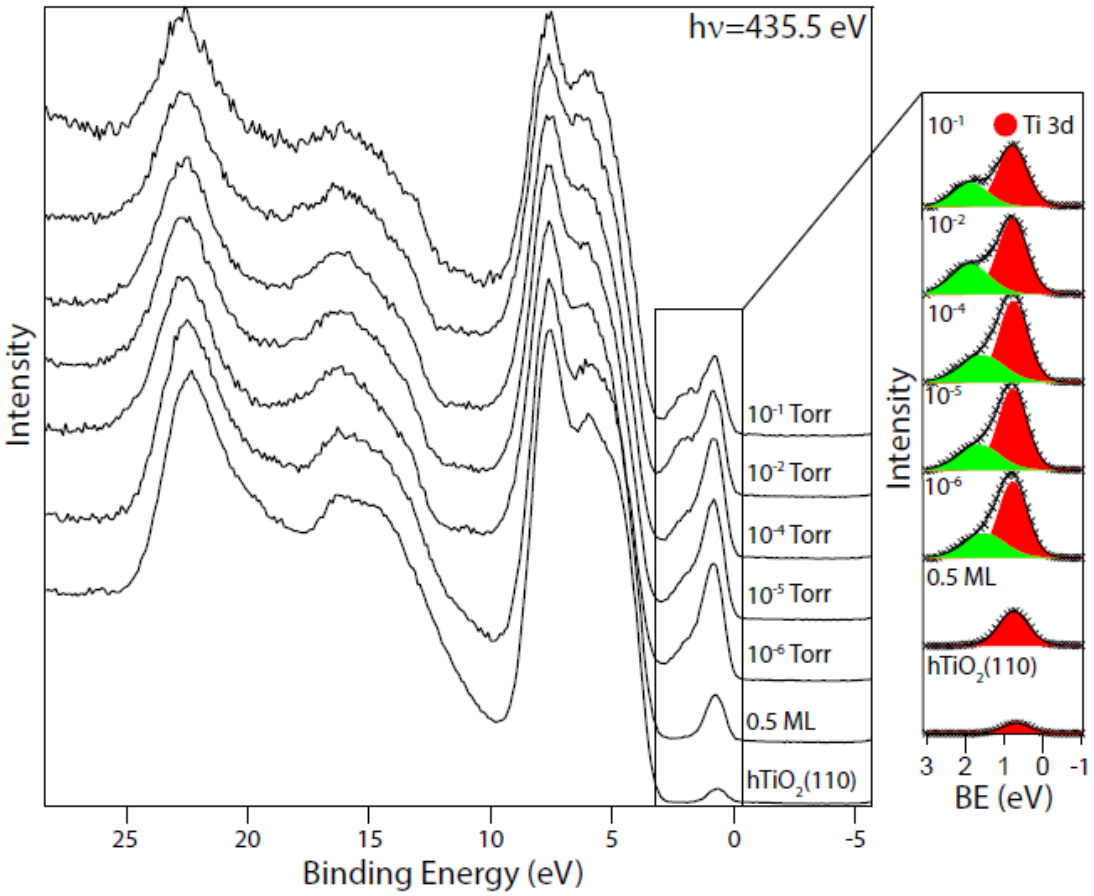

Fig 5.10: *Ti $L_{2,3}$ on-resonance photoemission valence band spectra of the $hTiO_2(110)$ surface, the same surface following saturation with 0.5 ML acetic acid (obtained under UHV conditions) and then held under increasing acetic acid partial pressure. Inset: magnified spectral region near the Fermi level (E_F) illustrating the evolution of the $TiO_2(110)$ defect state peak (red) and an additional peak (green) that appears when the acetic acid partial pressure in the chamber is 10^{-6} Torr and then increases in intensity as a function of acetic acid pressure. Experimentally acquired data points are shown as dots and numerical fits as solid lines. Spectra are normalised to the pre-band gap region and the O 2s peak at ~ 22 eV.*

In order to track changes to the valence band (VB) spectrum of the $hTiO_2(110)$ surface that could be attributed to atoms contained in the acetate ions forming the first half-monolayer, a difference spectrum formed via the subtraction of the $hTiO_2(110)$ VB spectrum from that of the 0.5 ML saturated $TiO_2(110)$ spectrum, following normalisation of the spectra to the pre-band gap region and the O 2s peak at 22 eV, is compared with the VB spectrum of acetic acid in figure 5.11. The latter spectrum was captured by performing a photoemission scan of the

acetic acid vapour at 10^{-2} Torr by moving the sample out of the path of the incident X-rays. The most distinguishable contrast between these two spectra is the prominent peak at ~0.8 eV below E_F in the difference spectrum but not the in the gas-phase spectrum. This signifies that the increase in the band gap state peak intensity is not simply due to the addition of intensity intrinsic to the PES of acetic acid. The feature induced at 1.5 eV arises from a charge transfer reaction involving acetic acid and the surface (as well as the bulk) TiO_2. There is no chemical pathway that can reasonably explain this without invoking some kind of subsurface contribution. This will need to be addressed in future work. The Ti 3d band-gap state highlighted in red in figure 5.10 is likely unchanging with pressure but attenuation by the adsorbed acetate/ acetic acid causes a reduction in the measured PES signal.

Though both spectra exhibit photoemission activity at similar binding energy in the region away from the band gap stage (5-20 eV), the photoemission peaks arising in the gas phase are sharper than those in the acetic acid difference spectrum. The likelihood is that as the molecules are chemisorbed, discrete peaks extant in the gas phase become smeared-out and convoluted into wider peaks due interaction with the substrate [39].

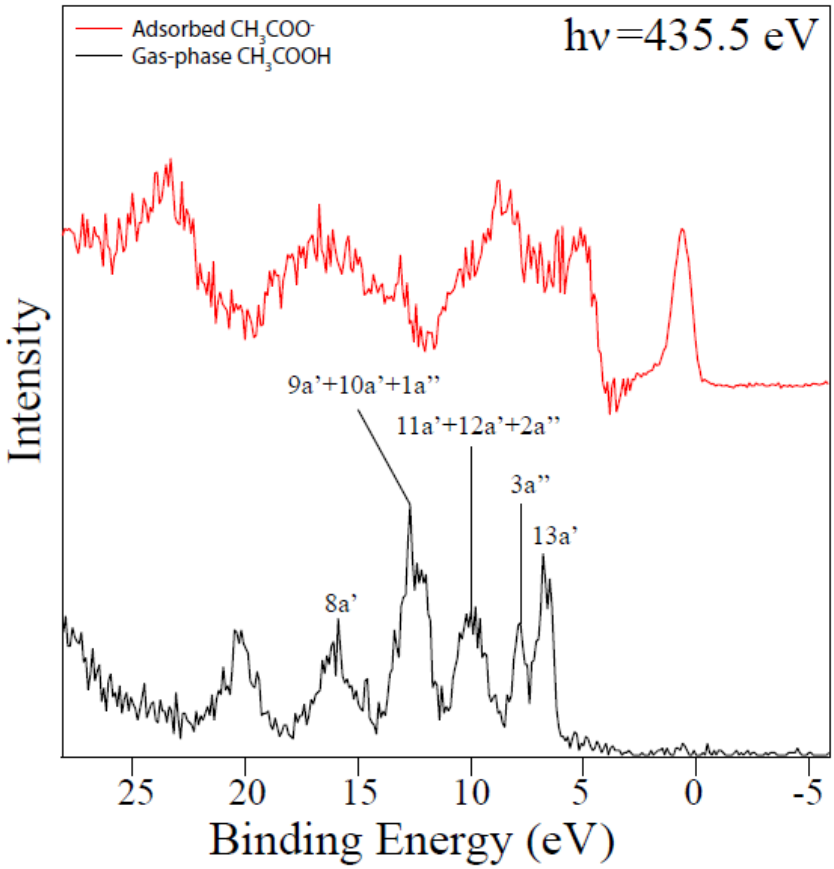

Fig 5.11: *Co-plotted Ti $L_{2,3}$ on-resonance spectra of a difference spectrum (red) obtained via the subtraction of a valence band (VB) spectrum of the as-prepared TiO_2(110) surface from the same surface following saturation with 0.5 ML acetate and a VB spectrum of 10^{-2} Torr gaseous acetic acid on which contributing molecular orbitals are indicated (black)*[40].

5.6 NEXAFS Study of Acetic Acid on TiO_2(110)

The bonding orientation of the acetate molecules that constitute 0.5 ML coverage of the TiO_2(110) surface under UHV conditions was examined using NEXAFS before the analysis was extended to higher partial pressures to explore the orientation of the acetic acid molecules constituting the second 0.5 ML. This was achieved by exploiting the dependence of the C 1s → $2b_2$ transition yield intensity on the angular displacement between the $2b_2$ orbital and the electric field vector of the incident photon beam (***E***-vector). Before proceeding to the experimental results, it is necessary to first discuss the spatial distribution of the $2b_2$ orbital of

the carboxyl group in the acetate/acetic acid molecules, which we used to gauge the bonding orientation of acetate/acetic acid on the surface.

A ball and stick model of the acetate anion is displayed in fig 5.12, below. The acetate moiety can be considered as two separate groups, each centred on a carbon atom. The carboxyl group, that identifies the molecule as a carboxylic acid, is comprised of a carbon atom single bonded to an OH group and double bonded with an O atom. When the molecule deprotonates in the presence of the TiO_2(110) surface, via the loss of the hydrogen atom from the OH group of the carboxyl group, the carboxylate group is formed, which is a hybrid of two simultaneous resonance structures. The second group, which both molecules share is the methyl group that identifies the carboxylic acid (carboxylate) as acetic acid (acetate) and is formed via a central carbon atom bonded to 3 hydrogen atoms. In both molecules the carbon atoms, central to each group are connected by a σ bond. It is the angular separation of the vector representing this C-C bond away from the surface normal that is used to define the polar angle, α, of the molecule. The azimuthal angle of the molecule, ϕ, is initially defined relative to the direction of propagation of the incident beam, before later being more conveniently defined as relative to the substrate geometry, typically. Previous studies of acetate have shown that resonances from σ bonds tend to overlap within the NEXAFS spectrum [11] and are relatively broad compared with the $2b_2$ bond that is formed via the overlap of p molecular orbitals from the carbon atom and the available p orbital in the oxygen atom in the carboxyl group of the acetic acid molecule (that is double bonded). In the resonance structure of the acetate molecule's carboxylate group the $2b_2$ orbital is extended across the O-C-O plane. In both molecules, the vector describing the direction of the $2b_2$ orbital is perpendicular to both the C-C σ bond direction and the O-C-O plane. Vectors describing the relative direction of the C-C σ MO and the $2b_2$ MO are

indicated on the diagram below for the purposes of highlighting their relative directions and positions in the model.

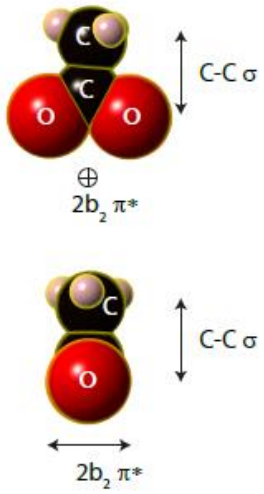

Fig 5.12: *Molecular model showing the relative directions of the $2b_2$ and C-C bonds in acetate.*

The $2b_2$ orbital is defined as a vector orbital [40] and this means that in response to irradiation by a light source of appropriately energetic photons, a maximum (minimum) in the C 1s → π* transition yield is observed when the ***E***-vector is parallel (perpendicular) to the direction of the vector describing the $2b_2$ orbital.

Figure 5.13 shows the C K-edge (hν = 275 – 320 eV) X-ray absorption spectra of the as-prepared TiO_2(110) surface, co-plotted with spectra from the same surface saturated with 0.5 ML of acetate, recorded as a function of the angle of polarisation of the *E*-vector, β. Spectra were recorded with the incident beam normal to the surface where β=0°(90°) corresponds to the *E*-vector parallel to the [1$\bar{1}$0] ([001]) direction, relative to the substrate surface. Data recorded following saturation of the sample with acetate exhibits a sharp peak at a photon

energy of ~289 eV. This peak represents the extent of electronic transitions from the C 1s atomic orbital in the carboxylate carbon atoms to the $2b_2$ anti-bonding orbital occurring within the carboxylate group in the acetate molecule at a given experimental geometry.

The extraction of data required to examine the angular dependence of the $2b_2$ resonance was a two-step process as illustrated in figure 5.13; firstly each pair of spectra (recorded at the same value of β) were normalised to the pre-edge region. Secondly, for each angle of the *E*-vector, the spectrum recorded from the clean surface was subtracted from that recorded from the acetate-saturated surface.

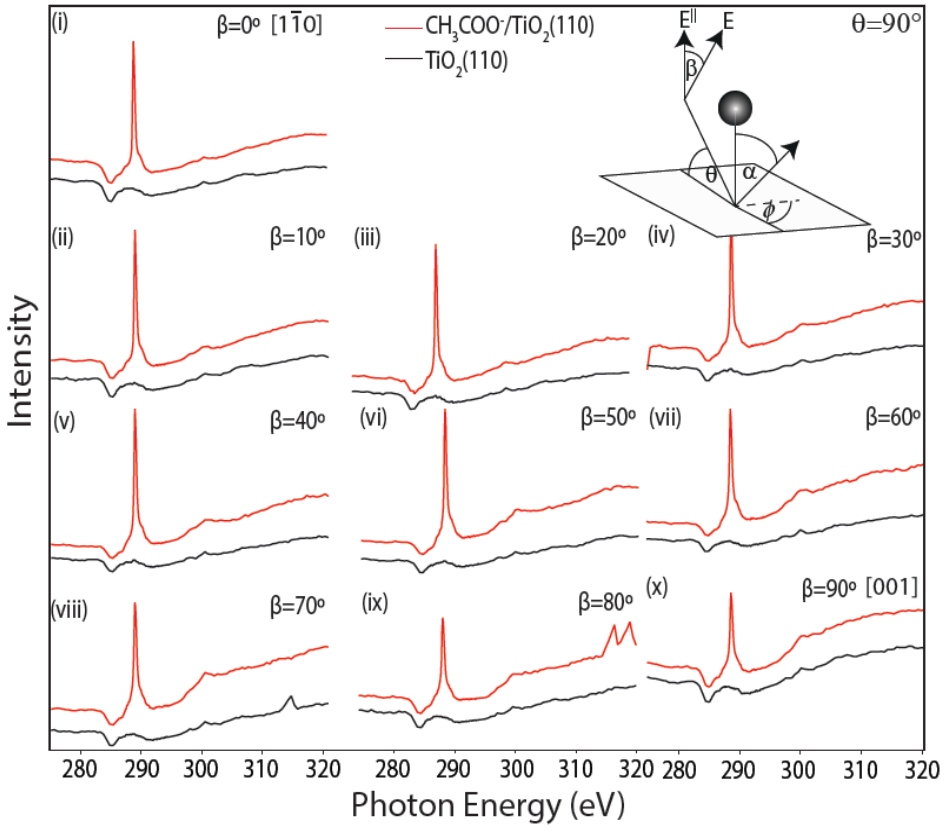

Fig 5.13: *C K-edge (270-320 eV) X-ray absorption spectra of hTiO$_2$(110) surface (black) and following saturation coverage (0.5 ML) with acetate (red). All spectra were recorded in Auger-electron yield (AEY) mode. The incident beam was held normal to the sample surface. Each pair of spectra were recorded at a different polarisation of the **E**-vector, β. β=0° pertains to this vector oriented parallel to the [1$\bar{1}$0] direction on the TiO$_2$(110) surface and each pair of spectra are normalised to their respective pre-edge regions.*

This process produces the series of C K-edge NEXAFS difference spectra that exhibit a sharp peak at 288.8 eV that represents the C 1s → $2b_2$ transition yield arising from the acetate anions on the substrate surface at a given polarisation of the ***E***-vector. These difference spectra are organised using increasing β in figure 5.14. The maximum (minimum) recorded instance of this transition occurs when the ***E***-vector is polarised at β=0°(90°), parallel to the [1$\bar{1}$0] ([001]) substrate-defined direction. The difference spectra are normalised to the height of the absorption step edge.

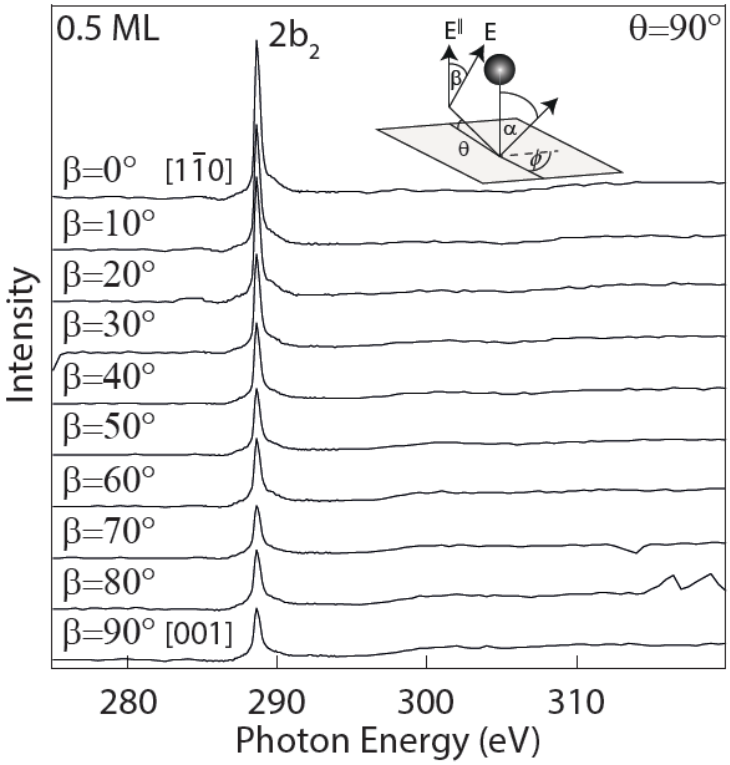

Fig 5.14: *C K-edge (275-320 eV) NEXAFS difference spectra of the TiO_2(110) surface following saturation with 0.5 ML of CH_3COO^-, recorded at normal incidence. Spectra were recorded as the **E**-vector of the incident photon beam was rotated from the [1$\bar{1}$0] azimuth (β=0°) to the [001] azimuth (β=90°). Spectra are normalised to the absorption step edge.*

The sharp peak observed in each difference spectrum is fitted using the multi-peak fit function in Wavemetrics Igor Pro and an example of this process is shown in figure 5.15. Each fit is a combination of three peaks; A Gaussian curve is fitted to the main peak, representing the $2b_2$

resonance and the area recorded under this Gaussian curve is taken as the C 1s → $2b_2$ transition intensity yield for a given value of θ and β. An exponential Gaussian function is fitted to the absorption edge jump, a step-like rise in the absorption coefficient at the ionisation threshold, defined as the difference between the intensity of the post-edge region and the pre-edge region. In all difference spectra, this feature rises from 0 → 1 as a reliable means of normalisation [40] of the NEXAFS spectra. Finally, a second Gaussian is fitted to a shoulder peak at ~290 eV that has been observed in a similar study and attributed to a slight imperfection in normalisation prior to subtraction to form difference spectra [29].

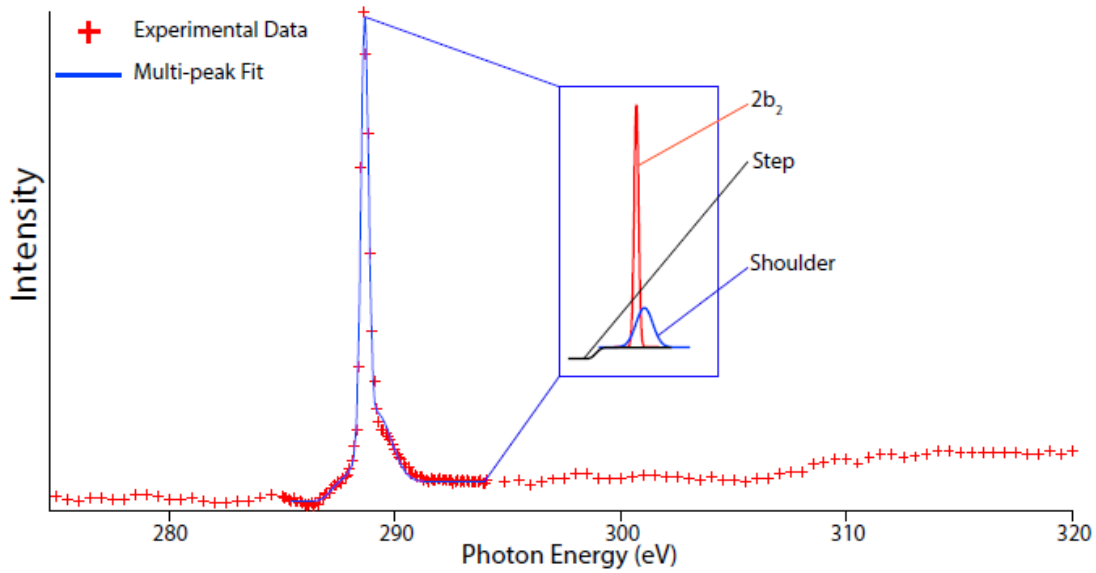

Fig 5.15: *Multi-peak numerical fit (blue envelope) of experimental (red crosses) C K-edge spectrum of the $CH_3COO^-/TiO_2(110)$ surface recorded at normal incidence and polarisation angle $\beta=0°$. Inset, the multi-peak fit envelope decomposes in to three peaks; the main peak pertaining to the C 1s → $2b_2$ resonance (red), the absorption edge-jump (black) and a shoulder (blue).*

The angular separation between the electric field vector, *E* of the incident beam and the vector describing the orientation of the $2b_2$ orbital defines the measured C 1s → π* transition yield in response to illumination by incident light of the appropriate wavelength. A schematic of the

NEXAFS experiment, where polarised X-rays are incident at angle θ, to the sample surface is displayed in figure 5.16. Inset, the spherical coordinates (1,α,ϕ) describing the direction of the π* vector orbital $\vec{O}$ are highlighted. The angle α describes the tilt of $\vec{O}$ away from $\vec{n}$ and ϕ describes the angular azimuthal twist of $\vec{O}$ out of the direction of the incident beam. The polarisation of the beam is described by the angle β out of the plane of incidence.

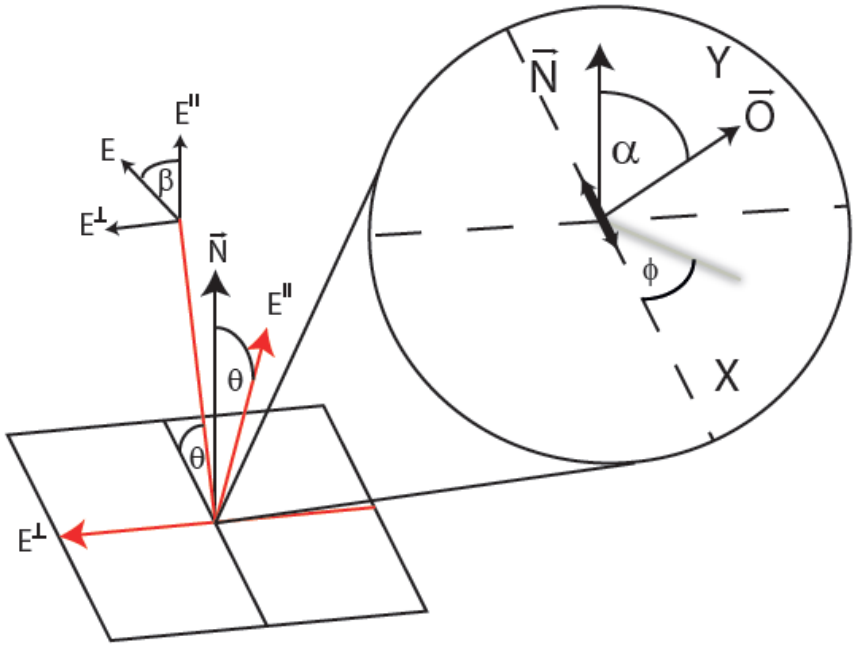

Fig 5.16: *Schematic of the NEXAFS experimental setup. The X-ray beam (highlighted in red) is incident at an angle θ to the sample surface. The orientation of a molecular orbital, $\vec{O}$ is described by the twist angle, α, away from the surface normal, $\vec{N}$ and the apparent twist out of an azimuth defined by the direction of the incident beam, ϕ. The polarisation angle β describes the direction of the electric field vector E of the incident photon beam, hence its components which are parallel ($E^{||}$) and perpendicular ($E^{\perp}$) to the plane of incidence.*

The equation below [41] describing the measured C 1s → π* transition intensity, ***I*** can be used to determine the orientation of the $2b_2$ orbital:

$$I = C[\cos^2 \beta I^{\parallel} + \sin^2 \beta \, I^{\perp}] \quad (5.2)$$

Where C is an arbitrary constant, β is the angular separation of the ***E***-vector of the incident photon beam from the plane of incidence, $I^{\parallel}(I^{\perp})$ the π* resonance that arises in response to illumination by the component of the ***E***-vector that runs parallel (perpendicular) to the plane of incidence. Note that when β = 0° (90°), the light incident on the surface is *p*- (*s*-) polarised.

Equations below derived by Stöhr and Outka describe the intensity components [41], $I^{\parallel}$ and $I^{\perp}$. These components are dependent on the nature of the probed transition and the rotational symmetry in the surface plane of the substrate. This investigation is of the orientation of a π* vector orbital of acetate/ acetic acid molecules adsorbed on to a substrate exhibiting two-dimensional rotational symmetry. The individual intensity components are dependent on the tilt α and twist ϕ of the inspected orbital.

$$I_V^{\parallel} = A(cos^2\theta cos^2\alpha + sin^2\theta sin^2\alpha cos^2\phi) \quad (5.3(i))$$

And:

$$I_V^{\perp} = Asin^2\alpha sin^2\phi \quad (5.3(ii))$$

Data must be recorded at two separate experimental geometries on each surface because determination of the two unknowns, the tilt angle, α and the twist angle, ϕ require the solution of two equations to pinpoint. After an initial experiment carried out at θ = 90º, data were collected from the clean and saturated surfaces with the beam held at an incident angle of θ =

19º to the sample as the electric vector of the light was rotated. It is known that in this case, that the beam is incident along the [1$\bar{1}$0] substrate-defined direction. This is understood because the sample's orientation, relative to its LEED pattern, is known. The difference spectra are exhibited in figure 5.17 where the $2b_2$ peak is again, prominent at 288.8 eV.

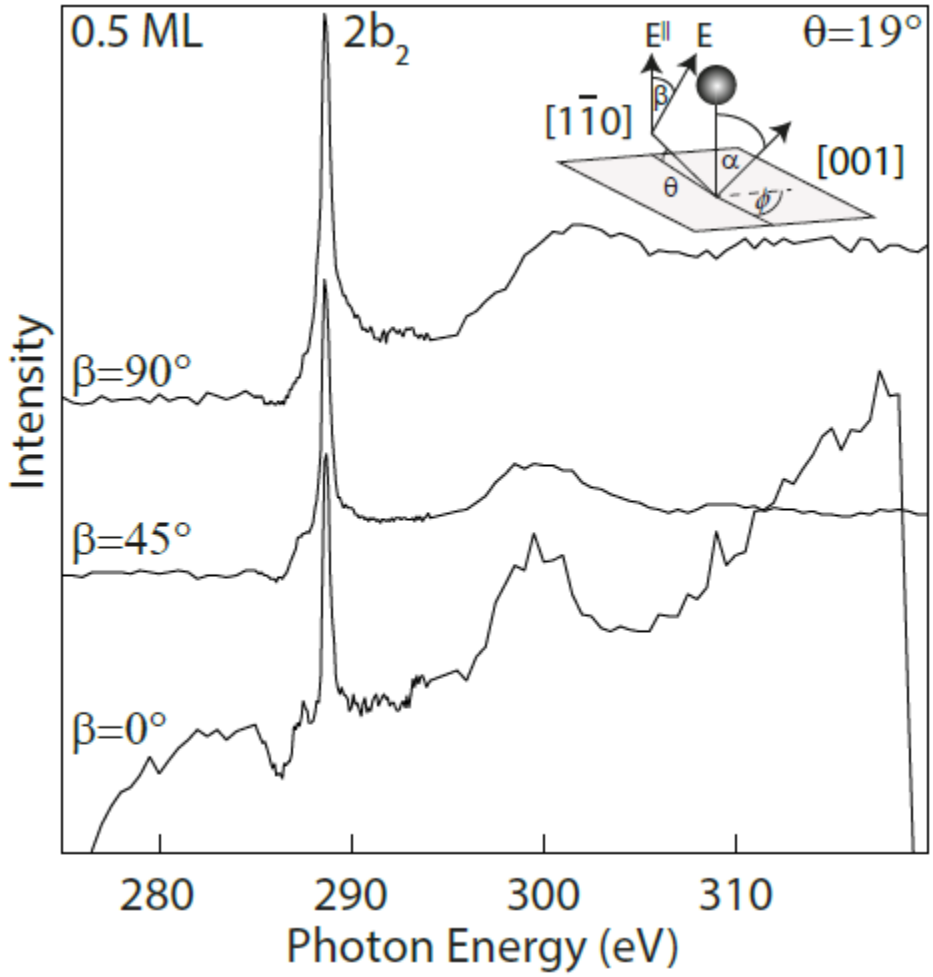

Fig 5.17: *C K-edge (275-320 eV) NEXAFS difference spectra of $CH_3COO^-/TiO_2(110)$ with the beam incident on the surface at 19º. Measurements are taken as the electric vector of the beam, β, is rotated in increments of 45º.*

The global fitting function in *Wavemetrics* IGOR Pro facilitates the simultaneous fitting of several functions. This function was used to plot the variation in the recorded transition intensity with the ***E***-vector polarisation of a beam incident at two incident angles simultaneously so as to define a unique set of unknowns (fig 5.18). Both sets of data were

normalised over a scale of 0-1 by dividing both sets of data by their respective preceding constant following co-fitting. Fitting again after normalisation delivered a tilt angle of $\alpha = 69.6^{\circ} \pm 8.2^{\circ}$ and a twist angle of the $2b_2$ orbital, $\phi = 32.4^{\circ} \pm 2.7^{\circ}$ out of the $[1\bar{1}0]$ substrate direction. These results indicate a molecule that is tilted 20.4° ± 8.2° away from the surface normal and twisted 32.4 ± 2.7° out of the [001] azimuth of the TiO_2(110) surface.

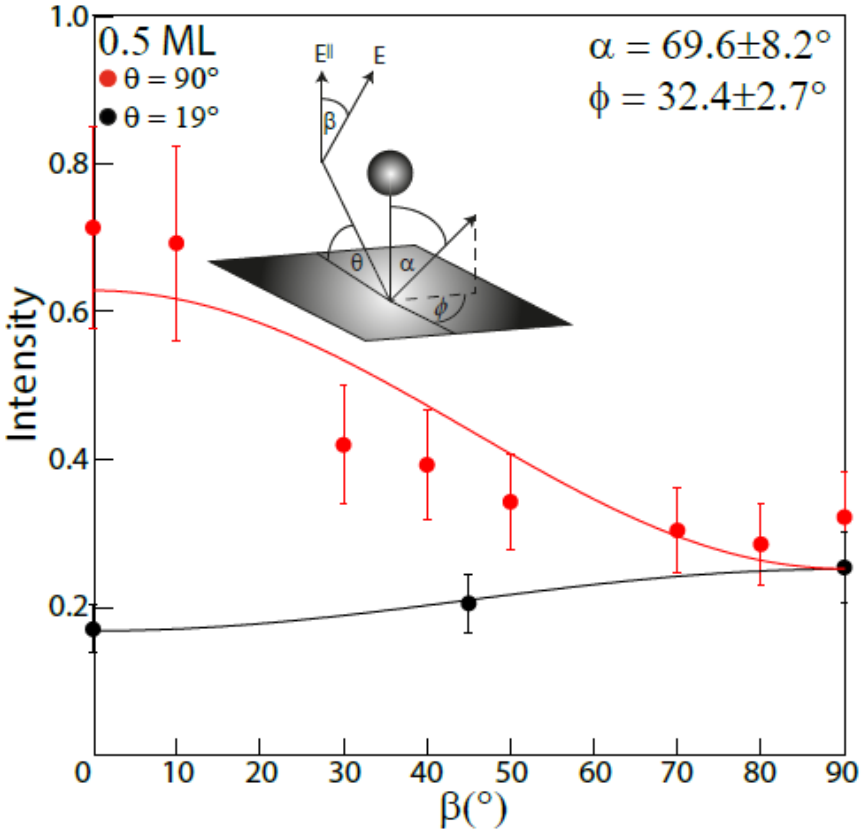

Fig 5.18: *Normalised integrated intensity of the C 1s → $2b_2$ transition as a function of angle of polarisation of the E-vector,β, determined at two different incident angles: θ=90° (red) and 19° (black). Dots represent experimentally acquired data and solid lines represent numerical fits to the data. Using the appropriate equations adapted from Stöhr and Outka's work [41], numerical fits applied to both sets of data simultaneously yields the tilt (α) and twist angles (ϕ), which describe the π* orbital of the carboxyl groups in the acetate molecules to be tilted 69.6°±8.2° and twisted 32.4°±2.7°.*

The errors in the intensities represented by error bars in each plot are determined by entering the upper and lower limits of the tilt angle back into equation 5.2 to determine the upper and

lower limit of the intensity for each angle of incidence. The tilt and twist angles of the adsorbed acetate molecules elucidated at saturation coverage both require further explanation as they are in conflict with previous studies. Firstly, the observed twist angle of the acetate molecule is curious as STM studies have shown that carboxylates adsorb on the rows of fivefold coordinated Ti^{4+} cations along the [001] direction [42,43]. It is understood that the scrutinised π^* orbital is orientated perpendicular to the carboxylate plane (i.e. parallel to the $[1\bar{1}0]$ direction of the substrate). The synchrotron beam is incident parallel to the $[1\bar{1}0]$ substrate direction and the twist angle should hence be ϕ=0°.

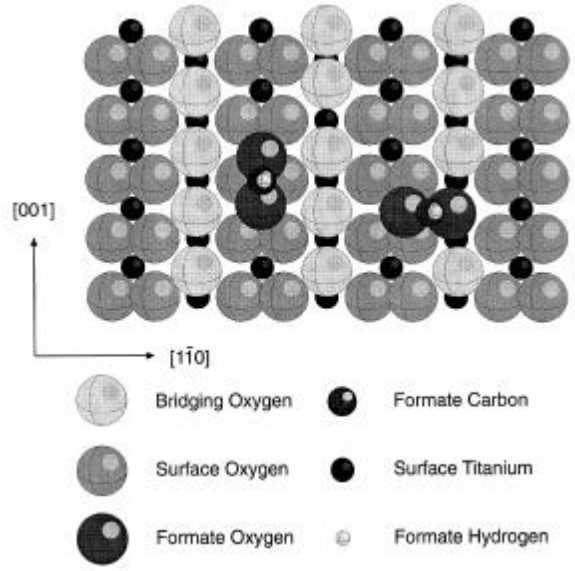

Fig 5.19: *A model of the majority and minority formate species on TiO_2(110) identified by chemical shift photoelectron diffraction [44] and FT-RAIRS [45].*

FT-RAIRS and PhD experiments carried out on the formate saturated TiO_2(110) surface (0.5 ML) identified a second species [44,45], aligned perpendicular to the [001] direction, seemingly by the filling in of a bridging oxygen vacancy (O_b-vac) with one of the O atoms in the carboxyl group. A ball model depicting how both of these species adsorb on the TiO_2(110) surface is presented in figure 5.19. Prior NEXAFS studies of the TiO_2(110) surface saturated

with formate, acetate and propanate arrived at the conclusion that due to the similar bonding mechanism of their respective anions to the TiO_2(110) surface to that of formate, the apparent twist angle observed in the NEXAFS measurements is likely a result of the averaging of X-ray absorption induced photoemission data arising from two domains of acid molecules that bond to the surface in different configurations: the majority species bond with their carboxyl planes running parallel to the [001] direction, while the minority species bond with their carboxyl planes running perpendicular to the [001] direction [11] via a bridging-oxygen vacancy.

Secondly, while the twist angle found in our study (32.4±2.7°) is in fine agreement with [11] (26±5°), the value we have proposed for the tilt angle of acetate (20.4±8.2°), is not, as [11] reports that the acetate molecules stand upright on the surface. The phenomena of acetate molecules adsorbed to the TiO_2(110) surface tilting towards and away from O_b sites as a result of repulsive and attractive interactions with the hydroxyls and neighbouring acetate ions that has been observed, however [46,47]. The polar orientation of acetate ions has thus been shown to vary locally on the TiO_2(110) surface. A molecular model, showing the tilting of acetate molecules adsorbed to TiO_2(110), relative to the surface, is available in figure 5.20.

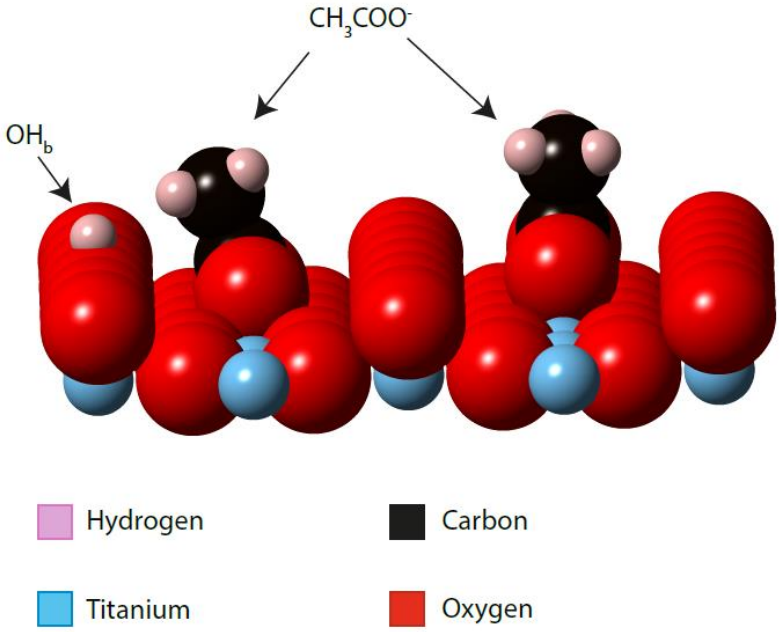

Fig 5.20: *Molecular model of CH_3COO^-/ TiO_2(110) at the limit of low coverage for illustrative purposes showing the physical tilting of adsorbed CH_3COO^- molecules towards OH_b sites created during the absorption of the anions to the TiO_2(110) surface.*

The Stohr and Outka equations [41] can be extended to decipher the relative geometry of the same molecule in various domains, as well as the extent of each domain. As previously mentioned, it is believed that the azimuthal angle of the acetate adsorbed on the TiO_2(110) surface that we have observed arises from two domains of acetate sharing the surface. The majority domain is orientated with the carboxylate plane of the molecule being orientated along the [001] direction of TiO_2(110) surface and the minority domain formed via the bonding of one oxygen atom from the acetate molecule to an O_b-vac on the substrate and the other oxygen atom in the acetate molecule bonding to a Ti^{4+} site. The majority and minority species are azimuthally orthogonal to each other.

Equations 5.2 and 5.3 are modified to the following to accommodate the study of the mutual existence of two domains with unique azimuthal orientation on the surface:

$$I_n = A\left[\cos^2\beta {I_n}^{\parallel} + \sin^2\beta\, {I_n}^{\perp}\right] + B\left[\cos^2\beta {I_{n-1}}^{\parallel} + \sin^2\beta\, {I_{n-1}}^{\perp}\right] + \cdots \qquad (5.4)$$

Where,

$$I_n^{\parallel} = A(cos^2\theta cos^2\alpha_n + sin^2\theta sin^2\alpha_n cos^2\phi_n) \qquad (5.5(i))$$

And,

$$I_n^{\perp} = Asin^2\alpha_n sin^2\phi_n \qquad (5.5(ii))$$

Where the constants A,B… represent the relative magnitude of each domain, the definitions of θ and β do not change and represent the incident angle of the beam and the angular separation of the $\boldsymbol{E}$-vector from the $E^{\parallel}$ position. The orientation of domain n is defined by (1,α_n,ϕ_n). A numerical fit to the data presented in fig 5.18 with the Stohr equation modified to accommodate the presence of two domains mutually occupying the surface. The beam is incident along the $[1\bar{1}0]$ direction and the $2b_2$ orbital is orientated perpendicular to the carboxylate plane of the acetate molecule. This means that $\phi_{[001]}$=0° (Domain A) and $\phi_{[1\bar{1}0]}$=90° (Domain B).

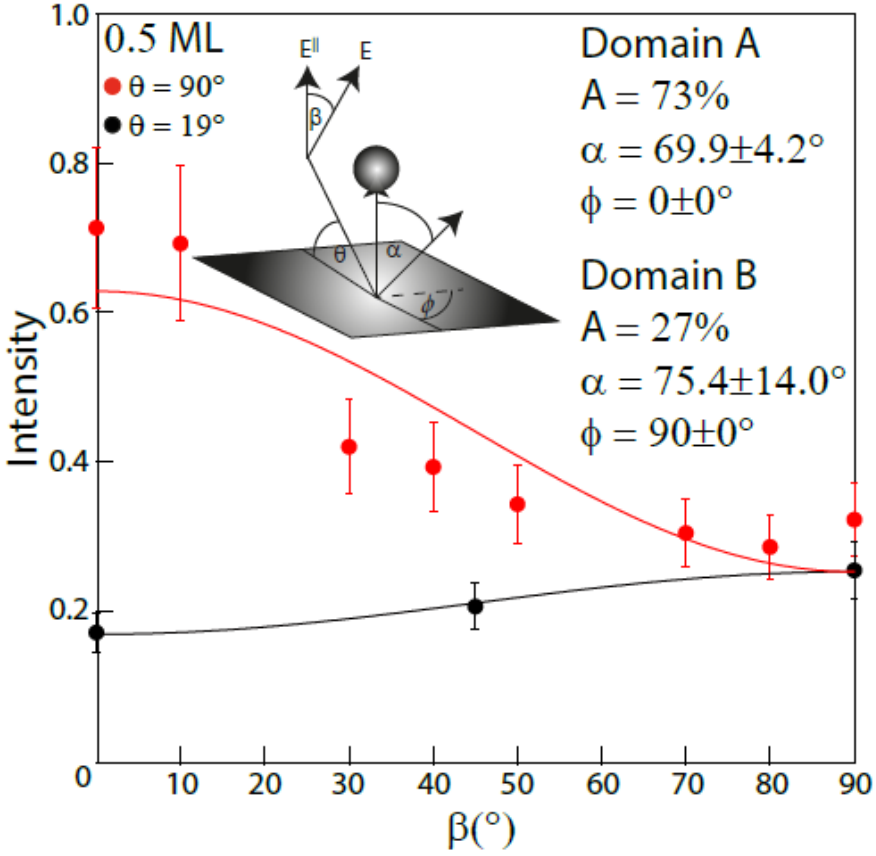

Fig 5.21: *Normalised integrated intensity of the $2b_2$ resonance as a function of the angle of polarisation of the **E**-vector, β. Experimental data represented by dots is as fig 5.18. Modified equations of Stohr and Outka [38] have been further extended to accommodate the elucidation of the tilt (α) and twist (ϕ) of two domains of CH_3COO^- mutually occupying the TiO_2 surface. 73% of the molecules are in domain A, the majority species where the carboxylate plane of the CH_3COO^- molecule is orientated along the [001] direction of the TiO_2 surface and tilted 20.1±4.2° out of the surface normal. The remaining 27% of the CH_3COO^- molecules are orientated along the $[1\bar{1}0]$ direction of the TiO_2(110) surface. The molecules comprising this minority species are tilted 14.6±14.0° away from normal.*

According to the numerical fit, above in figure 5.21, 73% of the acetate is bidentate bonded along the rows and 27% are in the minority orientation. As one oxygen vacancy is filled for every acetate atom bonded perpendicular to the rows, then the as-prepared TiO_2(110) surface has 13.5% of a ML of oxygen vacancies which is typical for this surface following the commonplace preparation conditions utilised [43]. The tilt angle $2b_2$ orbital of the minority species is 75.4 ± 14.0° along the $[1\bar{1}0]$ direction (14.6 ± 14.0º of the C-C bond away from the

surface normal). This is in better agreement with Sosa *et al*, perhaps due to the reduced likelihood of tilting of the molecule parallel to the carboxylate plane. It is noteworthy that the values describing the relative magnitudes for domain A and domain B were 0.73 and 0.27, respectively. The constants conveniently sum to unity because the two curves recorded at θ=90,19° were normalised to unity in figure 5.18 (fit for single domain).

5.7 AP-NEXAFS Study of Acetic Acid on TiO_2(110)

The multiple domain approach of NEXAFS analysis can be extended to accommodate multiple layers of adsorbate also. NEXAFS data were recorded from the TiO_2(110) surface while it was held under acetic acid pressures of 10^{-2} Torr and 10^{-1} Torr. From accompanying APPES analysis, it is apparent that at both pressures, the TiO_2(110) sample acquires 0.5 ML acetate as all of its Ti^{4+} surface sites are occupied and a second layer, 0.5 ML in thickness, thought to be comprised exclusively of acetic acid, bonded to the surface via O_b and OH_b sites.

Two sets of C K-edge NEXAFS data were recorded from the sample held in 10^{-2} Torr acetic acid as the ***E***-vector was rotated. One set of data was recorded with the beam incident normal to the sample and the other set of data was recorded with the beam at 19° to the sample surface, propagating along its [$1\bar{1}0$] direction. As with data collected from the saturated surface under UHV conditions, beamline structure is removed from the spectra via subtraction of data recorded at the same angle of incidence and the same ***E***-vector orientation but from the as-prepared TiO_2(110) substrate following normalisation to the pre-edge region. The resulting difference spectra, normalised to the absorption step edge are displayed in figure 5.22. The $2b_2$ resonance is prominent at 288.8 eV and its intensity was recorded by charting the area of a

Gaussian function fitted to each peak. The intensity arises from three sources, identified in APPES measurements. Firstly, acetate comprising the 1st 0.5 ML, secondly, acetic acid molecules, thought to comprise the second 0.5 ML and thirdly acetic acid molecules belonging to the gas phase. The relative contribution from the gas phase in APPES is ~3% at P_{AA} (Pressure of acetic acid) =10^{-2} Torr and it is thus considered negligible.

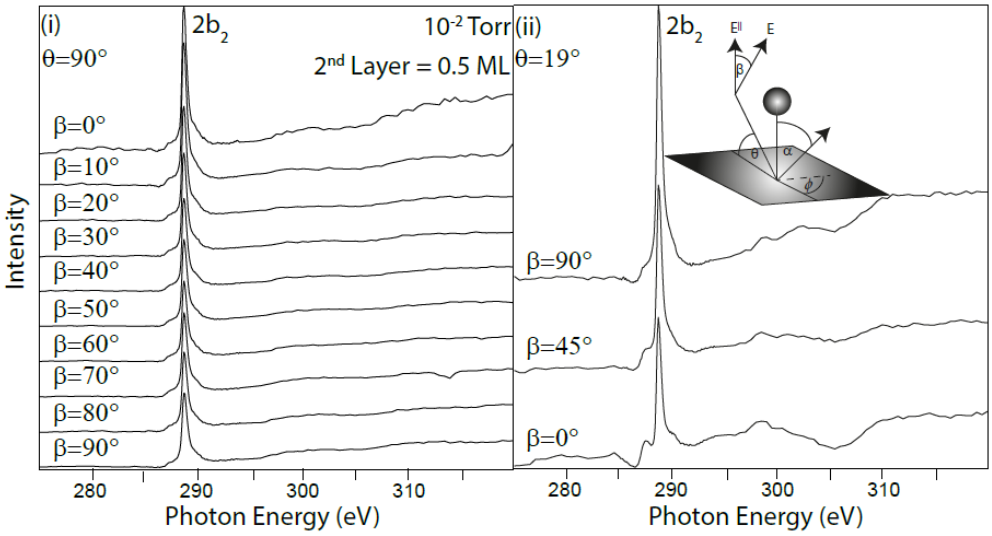

Fig 5.22: *C K-edge difference spectra (275-320 eV) recorded from the TiO_2(110) surface held under P_{AA} = 10^{-2} Torr with the beam incident at (i) θ=90° and (ii) θ=19° and in each difference spectrum, the polarisation of the **E**-vector, β, is altered. Each difference spectrum exhibits a sharp peak at 288.8 eV, representing, mainly, the C 1s → $2b_2$ XAS transition yield.*

The resultant statistics displayed in figure 5.23 chart the intensity of the $2b_2$ resonance as a function of β, the angular separation of the $\boldsymbol{E}$-vector away from the $E^{\parallel}$ position when the sample is held under 10^{-2} Torr acetic acid. A set of data recorded with the beam held incident normal to the surface are co-plotted with a set recorded with the beam incident at 19° and shining along the $[1\bar{1}0]$ direction in figure, below. In this case the data was fitted to determine the orientation of two distinct layers simultaneously. It is acceptable to normalise both data sets to make the constant in eq. 5.2 equal to unity because both the first and the second layer are

the same size in ML. Gas phase contributions are ignored as APPES data reports their extent to be ~ 3% at this pressure.

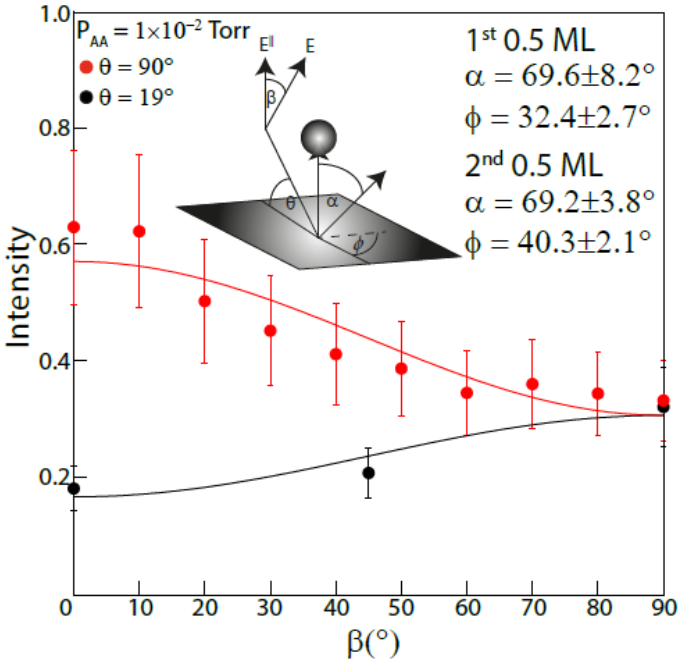

Fig 5.23: *Normalised integrated intensity of the $2b_2$ resonance as a function of angle of polarisation of the **E**-vector, β, determined from difference spectra in fig 5.21. The equations of Stohr and Outka [41], are extended to calculate the tilt (α) and twist (ϕ) angles of molecules comprising the second layer. The study suggests the tilt of molecules of the second layer are strongly influenced by that of the first.*

The first domain is the first layer, known to have a tilt angle of 69.6±8.2° and a twist angle of 32.4±2.7° associated with its $2b_2$ orbital. This layer is itself has two domains, orientated azimuthally perpendicularly. The second layer (domain) should also be comprised of two domains orientated perpendicular to each other, azimuthally, also. Co-fitting the curves (fig 5.23) delivers values of the $2b_2$ orbitals of the second layer of α=69.2±3.8° and ϕ=40.3±2.1°. The tilt angle of the $2b_2$ orbital (69.2±3.8°) suggests that the second layer molecules are orientated by molecules that are in the first layer as each second layer molecule is between 4 molecules from the first layer. The value of the azimuthal angle (40.3±2.1°) suggests a near 50:50 split between molecules bonded with their carboxyl plane along rows of O_b and those

bonded orthogonal to O_b. This is in contrast to the first layer where the minority domain that is bonded with the carboxylate plane along the [1$\bar{1}$0] azimuth of the substrate is dependent on the extent of available O_b-vac. It is also possible that the azimuthal angle is simply a snapshot of a changing surface at a given time in its evolution. As previously mentioned, evidence points towards the second layer forming via hydrogen bonding to OH_b sites created by the creation of the first layer. Firstly, these OH_b sites will influence the azimuthal angle of the second layer and their distribution across the surface will likely vary following each exposure of the clean TiO_2(110) surface to acetic acid. Secondly, it is likely that the second layer is dynamic, with acetic acid molecules breaking their hydrogen bonds and new molecules bonding continually, which would cause the azimuthal angle of the second layer to change with time.

The experiment was repeated with the sample held under 10^{-1} Torr acetic acid pressure. It is again known from the concomitant AP-XPS studies, that the coverage of the second layer is ~0.5 ML. Again, two sets of β dependent, C K-edge NEXAFS data are recorded with the beam incident normal to the surface and then at 19° to the surface, along the [1$\bar{1}$0] direction of the TiO_2(110) surface. The data sets, divided by the angle of incidence at which they were recorded are presented in figure 5.24. A large $2b_2$ resonance is observed at 288.8 eV. All spectra are difference spectra, created via the subtraction of spectra recorded from the bare TiO_2(110) surface and all difference spectra have an absorption step edge of unity in magnitude.

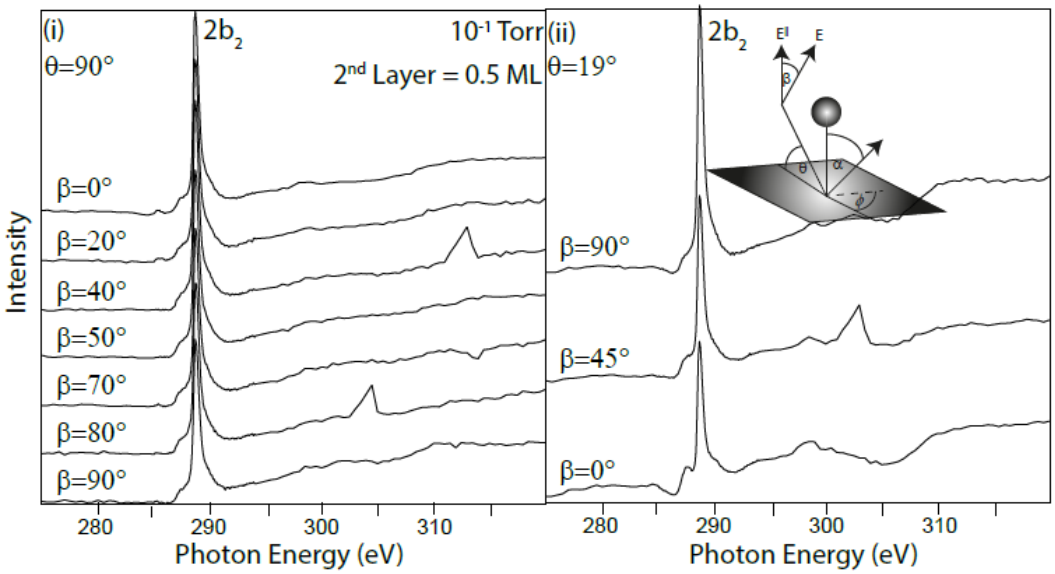

Fig 5.24: *As fig 5.22 but recorded at $P_{AA}=10^{-1}$ Torr.*

Gaussian functions were fitted to the $2b_2$ resonances of the curves displayed above in figure 5.24 at each angular rotation of the ***E***-vector. Two curves are presented in fig 5.25, one curve is recorded with the beam incident normal to the sample surface and the other with the beam grazing (19°) the surface. A numerical fit was initially carried out assuming only one domain is present (not shown) as a means of normalising the curves. As C 1s APPES data carried out on the system at 10^{-1} Torr showed that the gas phase constituted ~10% of the total yield. The constant prefixing the eq. 5.2 was set to 0.9 because the gas phase should be independent of the polarisation of the ***E***-vector and represented by a straight line of magnitude 0.1 (10%) for the numerical fit to the data, extended to two domains, presented in figure 5.25, below.

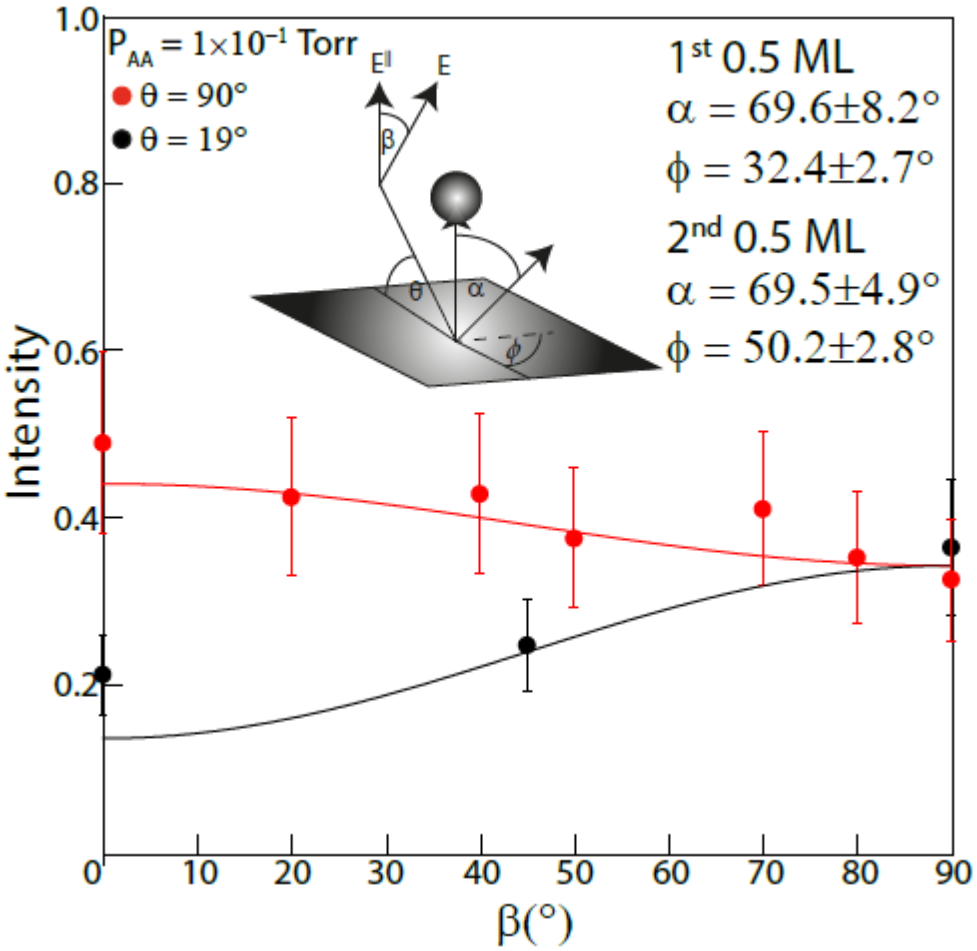

Fig 5.25: *As fig 5.23, but recorded at* P_{AA} *=* 10^{-1} *Torr.*

Analysis of the orientation of the second layer reveals values of α=69.5±4.9° and ϕ=50.2±2.8°. The C-C tilt angle is 20.5±4.9° out of the surface normal, suggesting as with the data recorded at 10^{-2} Torr that the polar orientation of the second layer is dependent on that of the first. The azimuthal angle, ϕ, a measure of the ratio of molecules with their carboxyl plane oriented along the [1$\bar{1}$0] and [001] substrate-defined directions, is significantly different from that recorded at 10^{-2} Torr, suggesting that the adsorption of the second layer is indeed a dynamic process.

5.8 Summary

The TiO_2(110) surface was saturated with 0.5 ML acetate and studied initially under UHV conditions before the system was studied under higher partial pressures of acetic acid. The chemical and electronic state were characterised using PES as well as the relative coverage. The orientation of adsorbed molecules was examined using NEXAFS.

C 1s PES revealed that at higher partial pressures, a second layer of adsorbate formed. This second layer is thought to be comprised of acetic acid molecules forming hydrogen bonds with substrate. Scrutiny of the VB region with PES revealed that the Ti 3d derived defect peak of the TiO_2(110) substrate is enhanced significantly by saturation exposure to acetic acid. This is probably due to charge transfer from adsorbed acetate. At higher partial pressures the main defect peak is seen to shrink as a shoulder peak grows at lower binding energy.

Analysis of NEXAFS data recorded from the saturated CH_3COO^-/ TiO_2(110) surface revealed that 73% of the acetate molecules were bonded with the carboxylate plane along the [001] direction of TiO_2(110) and 27% were bonded with their carboxylate plane along the [$1\bar{1}0$] direction of the same surface. The former species were tilted 20.4±8.2° away from the surface normal and the latter 14.6±14.0° away from the surface normal. The tilt angle of the former group can be explained by interactions of the acetate molecule with OH groups and adjacent acetate molecules.

NEXAFS studies of the sample under higher partial pressures revealed a tilt angle of the second 0.5 ML of adsorbate that suggested its molecular constituents are likely orientated by those

of the first layer. The twist angle of molecules comprising the second 0.5 ML were in poor agreement at different partial pressures, suggesting that the process is dynamic.

References

[1] C.L. Pang, R. Lindsay and G. Thornton, *Chemical Reviews*, **113** (2013) 3887.

[2] O.A. Illeperuma, *Materials Technology*, **28** (2013) 65.

[3] M.S. Liang, C.C. Khaw, C.C. Lui, S.P. Chin, J. Wang and H. Li, *Ceramics International*, **39** (2013) 1519.

[4] W.M. Campbell, A.K. Burrell, D.L. Officer and K.W. Jolley, *Coordination Chemistry Reviews*, **248** (2004) 1363.

[5] T. Tesfamichael, G. Will, J. Bell, K. Prince and N. Dytlewski, *Solar Energy Materials and Solar Cells*, **76** (2003) 25.

[6] M. Gratzel, *Comptes Rendus Chimie*, **9** (2006) 578.

[7] X.H. Zhang, J. Ogwa, K. Sunahara. Y. Cui, Y. Uemura, T. Myasaka, A. Furube, N. Koumura, K. Hara and S. Mori, *Physical Chemistry C*, **117** (2013) 2024.

[8] M. Yanagisawa, F. Korodi, J.J. He, L.C. Sun, V. Sundstrom and B. Akermark, *Journal of Porphyrins and Phthalocyanines*, **6** (2002) 217.

[9] K. Sodeyama, M. Sumita, C. O'Rourke, U. Terranova, A. Islam, L. Han, D.R. Bowler and Y. Tateyama, *The Journal of Physical Chemistry Letters*, **3** (2012) 472.

[10] P. Persson and S. Lunell, *Solar Energy Materials and Solar Cells*, **63** (2000) 139.

[11] A. Gutierrez-Sosa, P. Martinez-Escolano, H. Raza, R. Lindsay, P.L. Wincott and G. Thornton, *Surface Science*, **471** (2001) 163.

[12] H. Hong, *Acta Scientiae Circumstantiae*, **23** (2003) 224.

[13] M. Bron, D. Teschner, A. Knop-Gericke, B. Steinhauer, A. Scheybal, M. Havecker, D. Wang, R. Fodisch, D. Honickem A. Wootsch, R. Schlogl and P. Claus, *Journal of Catalysis*, **234** (2005) 37.

[14] J. Assmann, V. Narkhede, N.A. Breuer, M. Muhler, A.P. Seitson, M. Knapp, D. Crihan, A. Farkas, G. Mellua and H. Over, *Journal of Physics-Condensed Matter*, **20** (2008) 1.

[15] M. Muhler and H. Over, *Progress in Surface Science*, **72** (2003) 3.

[16] H. Bluhm, K. Andersson, T. Araki, K. Benzerara, G.E. Brown, J.J. Dynes, S. Ghosal, M.K. Gilles, H.-Ch. Hansen, J.C. Hemminger, A. P. Hitchcock, G. Ketteler, A.L.D Kilcoyne, E. Kneedler, J.R. Lawrence, G.G. Leppard, J. Majzlam, B.S. Mun, S.C.B Myneni, A. Nilsson, H. Ogasawara, G. Ogletree, K. Pechler, M. Salmeron, D.K. Shuh, B. Tonner, T. Tyliszczak, T. Warwick, T.H. Yoon *Journal of Electron Spectroscopy and Related Phenomena* **150** (2006) 86.

[17] T. Warwick, N. Anderson, J. Comins, K. Kaznacheyev, J.B. Kortright, J.P. McKean, H.A. Padmore, D.K. Shuh, T. Stevens, T. Tyliszczak *Synchrotron Radiation Instrumentation* **705** (2004) **458.**

[18] R. Follath and F. Senth, *Nuclear Instruments and Methods in Physics Research*, **390** (1997) 388**.**

[19] U. Diebold and T.E. Madey, *Surface Science Spectra*, **4** (1998) 227.

[20] G. Hähner, *Chemical Society Review*, **35** (2006) 1244.

[21] F. Allegretti, J.P.W. Treacy and R. Lindsay, *Physical Review B*, **85** (2012) 205422.

[22] N. Kruse and S. Chenakin, *Applied Catalysis A: General*, **391** (2011) 367.

[23] M.E. Simonsen, Z. Li and E.G. Søgaard, *Applied Surface Science*, **255** (2009) 8054.

[24] Q. Guo and E.M. Williams, *Surface Science*, **433** (1999) 322.

[25] M.A. Filler, J.A. Van Deventer, A.J. Keung and S.F. Bent, *Journal of the American Chemical Society*, **126** (2006) 770.

[26] H.K. Lee, K.J. Kim, J.H. Han, T.H. Kang, J.W. Chung and B. Kim, *Physical Review B*, **77** (2008) 115324.

[27] N. Ottosson, E. Wernersson, J. Soderstrom, S. Kaufmann, S. Svensson, I. Persson, G. Ohrwall and O. Bjorneholm, *Physical Chemistry Chemical Physics*, **13** (2011) 12261.

[28] S.R. Smith and T.D. Thomas, *Journal of the American Chemical Society Legacy*, **100** (1978) 5459.

[29] A. Krepelova, T. Bartels-Rausch, M.A. Brown, H. Bluhm and M. Ammann, *The Journal of Physical Chemistry A*, **117** (2013) 401.

[30] N. Padmanabhan, P.K. Deshpande and N.R. Kuloor, *Industrial and Engineering Chemistry Process Design and Development*, **7** (1968) 511.

[31] L.C. Mayor, J.B. Taylor, G. Magnano, A. Rienzo, C.J. Satterley, J.N. O'Shea and J. Schnadt, *Journal of Chemical Physics*, **129** (2008) 114701.

[32] P. Krüger, S. Bourgeois, B. Domenichini, H. Mangnan, D. Chandesris, P. Le Fèvre, A.M. Flank, J. Jupille, L. Floreano, A. Cossaro, A. Verdini and A. Morgante, *Physical Review B*, **100** (2008) 055501.

[33] M. Masahiko, T. Uozumi, A. Kotani, Y. Harada and S.Shin, *Journal of the Physical Society of Japan*, **71** (2002) 347.

[34] F. Allegretti, J. P. W. Treacy and R. Lindsay, *Physical Review B*, **85** (2012) 205422.

[35] M. Sanchez-Agudo. L. Soriano, C. Quiros, M. Abbate, L. Roca, J. Avila and J. M. Sanz, *Langmuir*, **17** 2001 7339.

[36] K. C. Prince, V. R. Dhanak, P. Vinetti, J. F. Walsh, R. Davis, C. A. Muryn, H. S. Dhariwal, G. Thornton and G. van der Laan, *Physical Review B*, **55** (1997) 9520.

[37] L.E. Walle, A. Borg, P. Uvdal and A. Sandell, *Physical Review B*, **86** (2012) 205415.

[38] C.M. Yim, C.L. Pang and G. Thornton, *Physical Review Letters*, **104** (2010) 036806.

[39] D. Cappus, J. Klinkmann, H. Kuhlenbeck and H.J. Freund, *Surface Science*, **325** (1995) 421.

[40] S. Bahr, A. Borodin, O. Höfft, V. Kempter, A. Allouche, F. Borget and T.Chiavassa, *Journal of Physical Chemistry B,* **110** (2006) 8649.

[41] J. Stohr and D.A. Outka, *Physical Review B*, **36 (**1987) 7891.

[42] H. Onishi, Y. Yamaguchi, K. Fukui and Y. Iwasawa, *Journal of Physical Chemistry,* **100** (1996) 9582.

[43] H. Onishi and Y. Iwasawa, *Chemical Physics Letters,* **226** (1994) 111.

[44] B.E. Hayden, A. King and M.A. Newton, *Journal of Physical Chemistry B*, **103** (1999) 203.

[45] S. Thevuhasan, G.S. Herman, Y.J. Kim, S.A. Chambers, C.H.F. Peden, Z. Wang, R.X. Ynzunza, E.D. Tober, J. Morias and C.S. Fadley, *Surface Science Letters,* **401** (1998) 261.

[46] K.Fukui and Y.Iwasawya, *Surface Science,* **464** (2000) 719.

[47] A.S. Foster and R.M. Nieminen, *Journal of Chemical Physics,* **121** (2004) 9039.

Chapter 6: Structural characterisation of the $Fe_3O_4(111)$ single crystal surface

6.1 Introduction

Iron is a transition metal with two variable oxidation states, Fe^{2+} and Fe^{3+} that forms oxides with distinct crystal structures; FeO (wüstite), Fe_3O_4 (magnetite) and α-Fe_2O_3 (hematite). There also exist a further two synthetic oxides; γ-Fe_2O_3 (maghemite) and ε-Fe_2O_3. These iron oxides have unique and overlapping industrial applications [1]. Reactions that occur at the surface of magnetite (Fe_3O_4) are relevant to the field of catalysis [2]. The $Fe_3O_4(111)$ surface reveals three possible surface terminations, akin to slicing various distances through the bulk. These three terminations have been observed using scanning tunnelling microscopy (STM) and are described as follows [3]; surface A' is a close-packed oxygen layer revealing ¼ ML tetrahedrally coordinated Fe ions. Capping each of these Fe ions with an oxygen atom produces surface A. On surface B an oxygen layer caps ½ ML of equal numbers of octahedral and tetrahedral Fe ions [3]. These surfaces are illustrated schematically in the molecular model, below (figure 6.1). Fe_3O_4 is viewed from a perspective perpendicular to the (111) direction to illustrate where each termination is situated throughout the bulk, respective to the others. A bird's eye view of each (111) surface is presented, inset.

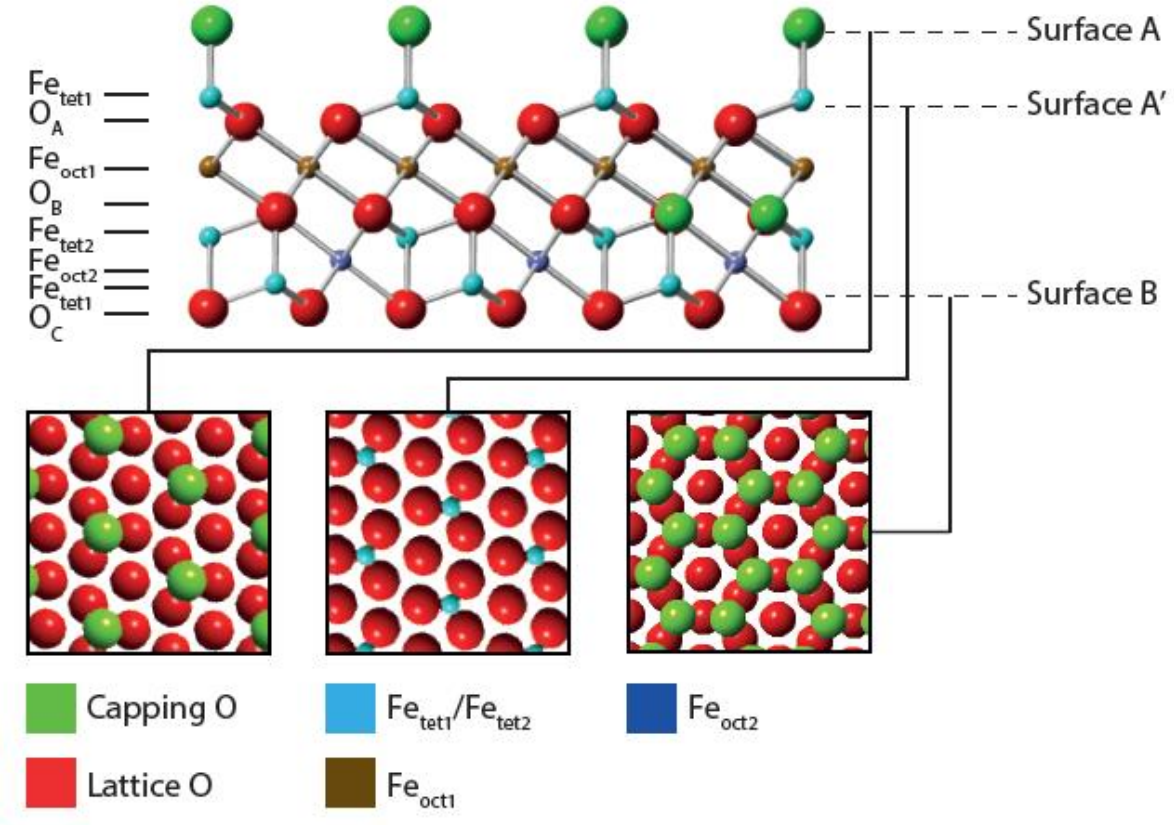

Fig 6.1: *Bulk structure of Fe_3O_4 displayed from a perspective that clearly exhibits layers of atoms lateral to the (111) plane. Planate layers comprised of single atomic species parallel to the (111) surface are identified to the left of the bulk model. Slicing the model at a depth pinpointed on the right, exposes one of its three possible (111) terminations (A,A' or B). A top-down view of each surface is presented inset; surface A' is a close-packed oxygen layer revealing ¼ ML tetrahedrally coordinated Fe ions, capping each of these Fe ions with an oxygen atom produces surface A and surface B is an oxygen layer capping ½ ML of equal numbers of octahedral and tetrahedral Fe ions.*

The scrutiny of the interactions with surfaces can be crucial to understanding the route by which they catalyse certain reactions. Cutting *et al* [3] were able to make significant inroads into understanding the morphology of these three surfaces by exposing them to three organic molecules (ball and stick models, figure 6.2); formic acid, pyridine and carbon tetrachloride, chosen because of their variable chemistry on oxide surfaces [4-8]. Of the three terminations, A' is the most reactive. The acids react distinctly with each surface. According to the STM results of Cutting *et al* [3], formic acid undergoes dissociation at the magnetite surface, bonding

to the A' surface via a bidentate linkage while a weaker 'physisorption' is observed of formate and pyridine to surfaces A and B. Pyridine absorbs to surface A' via its nitrogen atom. Carbon tetrachloride reacts only with surface A' and the molecule undergoes a series of temperature dependent dissociations and surface chemical reactions [3].

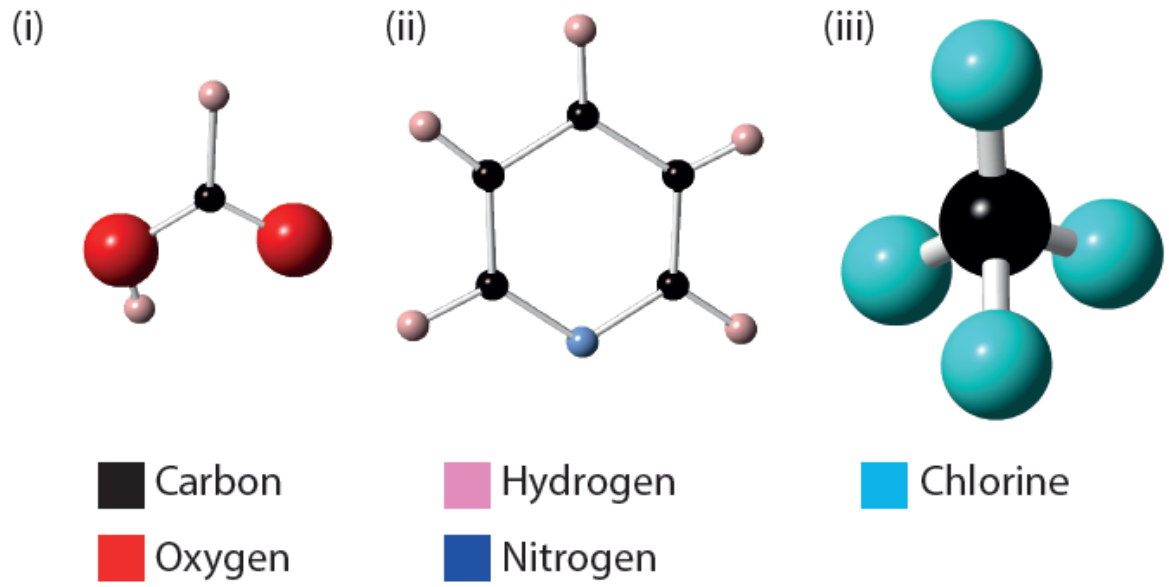

Fig 6.2: *Ball and stick models of (i) formic acid (HCOOH), (ii) pyridine (C_5H_5N) and (iii) carbon tetrachloride (CCl_4).*

The details of the reactivity of each termination are concluded from STM and lack associated chemically sensitive information. We constructed an experiment for beamline I06 at the Diamond Light Source [9] with the aim of bridging the chemical/spatial gap for adsorption to this surface. We attempted to initially identify the three terminations observed by Cutting *et al* [3] by using the work function of each surface as a contrast mechanism for imaging. This was to be followed by a further experiment employing XPEEM and µXPS measurements to chemically identify, with spatial resolution, the reaction products after the exposure of the clean Fe_3O_4(111) surface to formic acid, pyridine and carbon tetrachloride. Additionally, µ-NEXAFS

analysis was to be carried out to establish the orientation of the adsorbed molecules in each case.

Under the intense light of the synchrotron beam, the acids were quickly stripped off the sample and it was not possible to establish any useful experimental data from XPEEM measurements. LEEM and LEED I-V data were collected subsequently from the bare substrate surface. The reasons for this are two-fold; firstly, electrons are a gentler probe than X-rays. Secondly, while there have been extensive structural characterisations of Fe_3O_4(111) thin-films on various metal substrates such as Pd(111), Pt(111) and Ru(0001) [10-13] carried out with LEED I-V analysis, no such study of the corresponding single crystal surface is available for comparison. This is due to fairly commonplace issues associated with metal oxide single-crystals such as low conductivity, poor control over impurities and in some cases, simply difficulties obtaining a single-crystal sample [13]. Thin films of each naturally-occurring oxide of iron can be synthesised at various O_2 pressures, oxidation temperatures and levels of iron exposure [1]. Previous LEED I-V studies of thin Fe_3O_4(111) films by Barbieri *et al* [13] and Ritter *et al* [10] report a surface comprising a ¼ monolayer of Fe ions at 3-fold hollow sites of a close-packed oxygen layer. Characterisation of this surface by LEED I-V is complicated by the coexistence of 180º rotated Fe_3O_4(111) domains [10,13-16] and in a recent study by Sala *et al*, the extent of each of these rotated domains is quantified using LEEM [16].

6.2 Experimental

All experiments were carried out in an ultra-high vacuum (UHV) chamber with a base pressure of 1×10^{-10} mbar. As described in detail in chapter 3, the preparation chamber is equipped with an ion-bombardment gun and a sample heater for specimen cleaning, gas inlet valves are also present. Furthermore, the chamber facilitates low energy electron diffraction (LEED) and Auger electron spectroscopy (AES) experiments as a means of sample characterisation. The preparation chamber is separated via a gate valve from the experimental chamber that is an Elimtec LEEM III spectroscopic photoemission and low energy electron microscope (SPELEEM). This multi-faceted instrument is capable of performing both bright and dark-field low energy electron microscopy (LEEM), X-ray photoemission electron microscopy (XPEEM), X-ray magnetic circular dicroism (XMCD-) and X-ray linear dicroism (XMLD-) PEEM, micro-X-ray photoelectron microscopy (μXPS) and micro-spot low energy electron diffraction (μLEED). The Fe_3O_4(111) single-crystal sample was prepared by cycles of sputtering and annealing to 900 K until an Fe_3O_4(111) low energy electron diffraction (LEED) pattern was observed and no contaminant peaks were observed in Auger electron spectroscopy (AES) measurements. The as-prepared magnetite sample was exposed to 1.2×10^{-6} mbars of pyridine (C_5H_5N) and carbon tetrachloride (CCl_4) vapour in the preparation chamber, the acids were administered through a leak valve. LEED I-V data were taken in the energy range 40-199 eV, using the LEEM optics.

6.3 XPEEM Characterisation of the $Fe_3O_4(111)$ Single Crystal Surface

XAS spectra are normalised to the π* resonance of a natural graphite sample. The spectra are not shown here, but can be seen in figure 4.1 in chapter 4. The energy range of all XAS spectra that follow are corrected in this manner. The O K-edge XAS spectrum obtained experimentally from the as-prepared $Fe_3O_4(111)$ single crystal surface, recorded in the energy range 522-562 eV is presented in figure 6.3. The spectrum is in good agreement with both previous band-structure calculations [17] and experimental data [17-19]. The peak at 530 eV is thought to arise from hybrid O 2p and Fe 3d orbitals [18]. Spectral features observed at higher energies are due to O 2p states hybridised with Fe 4s and Fe 4p states [19].

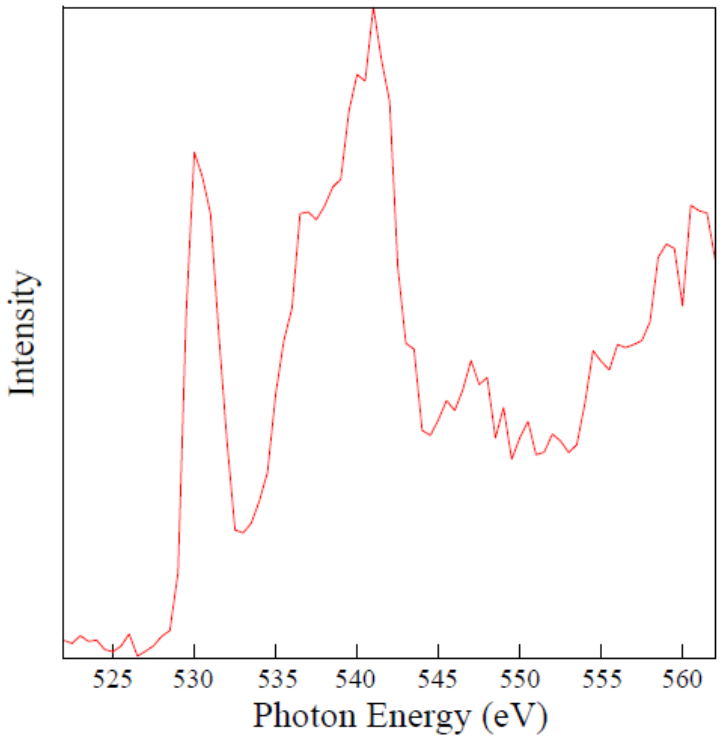

Fig 6.3: *O K-edge XAS spectrum (522-562 eV) recorded from the as-prepared $Fe_3O_4(111)$ substrate. Spectral features are in fine agreement with previous studies* [17-19].

An absorption spectrum from the same substrate but recorded across the Fe $L_{2,3}$ edge is presented in figure 6.4 and like the O K-edge spectrum, it agrees well with a previous experimental study [20]. The spectrum is contributed to by the three Fe ions in $Fe_3O_4(111)$ bonded in different chemical environments (1/3 Fe^{2+} octahedral, 1/3 Fe^{3+} octahedral and 1/3 Fe^{3+} tetrahedral.) [21].

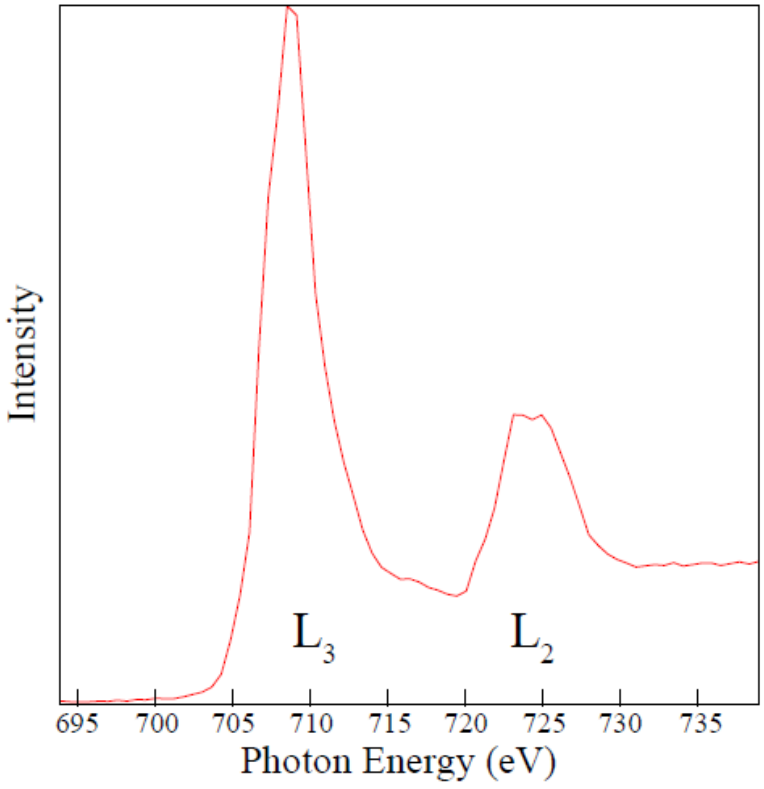

Fig 6.4: *Fe $L_{2,3}$-edge XAS spectrum (694-739 eV) recorded from the as-prepared $Fe_3O_4(111)$ substrate. Spectral features are in fine agreement with previous studies* [20].

XPEEM images recorded at appropriate energies serve as a spatial snapshot of X-ray absorption on the surface of a material. In figure 6.5 images recorded just above the Fe (i) L_3 and (ii) L_2-edges are presented. The images appear to show two distinct regions, ~ 4 µm across. It is unlikely that they are domains with distinct surface terminations; Cutting *et al* reported domains of the order of 100 nm [3] and the same method of surface preparation is carried out

in this study. It is possible that the structures could be due magnetic effects, but without a full XMCD study it is not possible to tell. Magnetic domains of a similar nature have been observed in XPEEM studies of Fe_2O_3 and other magnetic systems [22,23].

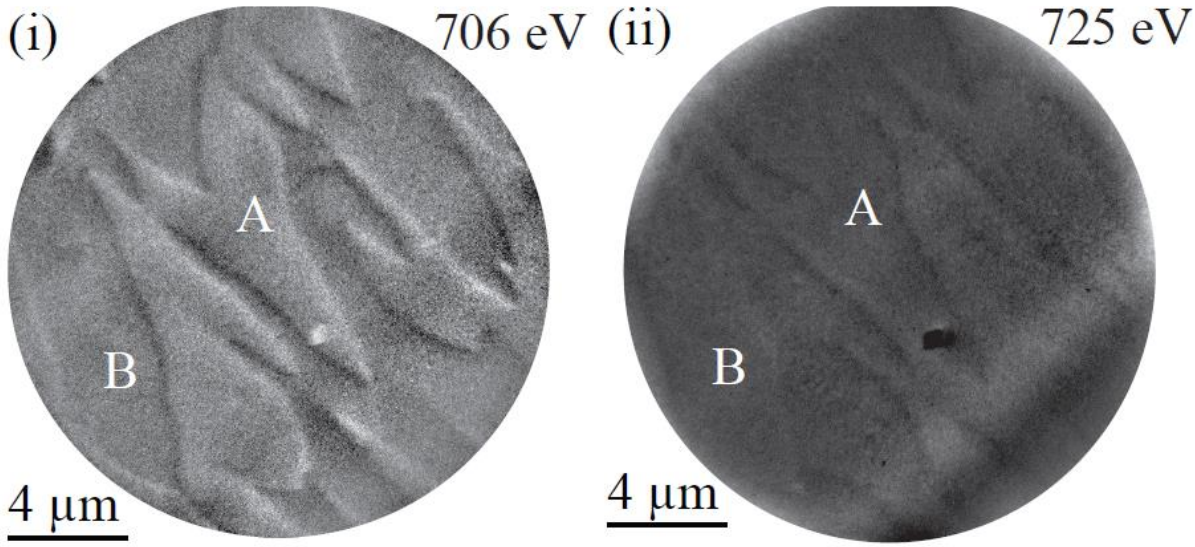

Fig 6.5: *XPEEM images with a 20µm FOV collected from the Fe_3O_4(111) surface slightly (within 2 eV) above the (i) Fe L_3-edge and (ii) Fe L_2-edge. Two regions, labelled A and B, are evident which likely arise from the long range structure or magnetic effects rather than two chemically different domains which are known from STM work at UCL to be only ~100 nm.*

To further invesitigate, µXAS spectra were recorded from each region and plotted together to compare their shape and extent. The spectra presented in figure 6.6 were synthesised from XPEEM images recorded at an incident energy of 694-739 eV. Inset, the L_3 and L_2 peaks of each domain are superimposed to highlight any subtle changes that would distinguish the surfaces structurally. No distinction can be drawn between the shape of the absorption edges, bar a slight difference in amplitude of the L_2-edges, most likely due to imperfect normalisation. Individual domains could perhaps have been identified were it possible in this instance to record higher resolution XPEEM images. XPEEM images recorded at a resolution of an order of 50 nm imaged in supremely surface-sensitive Auger yield mode, could perhaps have been used to identify each surface. Theoretical Fe $L_{2,3}$-edge spectra have been generated by

Crocombette *et al* that agree well with Fe $L_{2,3}$-edge XAS spectra aquired experimentally [24]. These theoretical curves were generated by summing Fe $L_{2,3}$-edge plots arising from the three different types of iron atoms in magnetite (octahedrally oriented Fe^{2+} and Fe^{3+} and tetrahedrally orientated Fe^{3+}), seperately. As these three different ions exist in equal proportions within the constitution of magnetite, an equally weighted additive contribution of these three spectra produce an estimate of bulk Fe $L_{2,3}$-edge spectra from magnetite. Perhaps more highly surface-sensitive, higher resolution XPEEM data could be used to pinpoint the Fe $L_{2,3}$-edge features associated with each termination via comparison with the work of Crocombette *et al* [24].

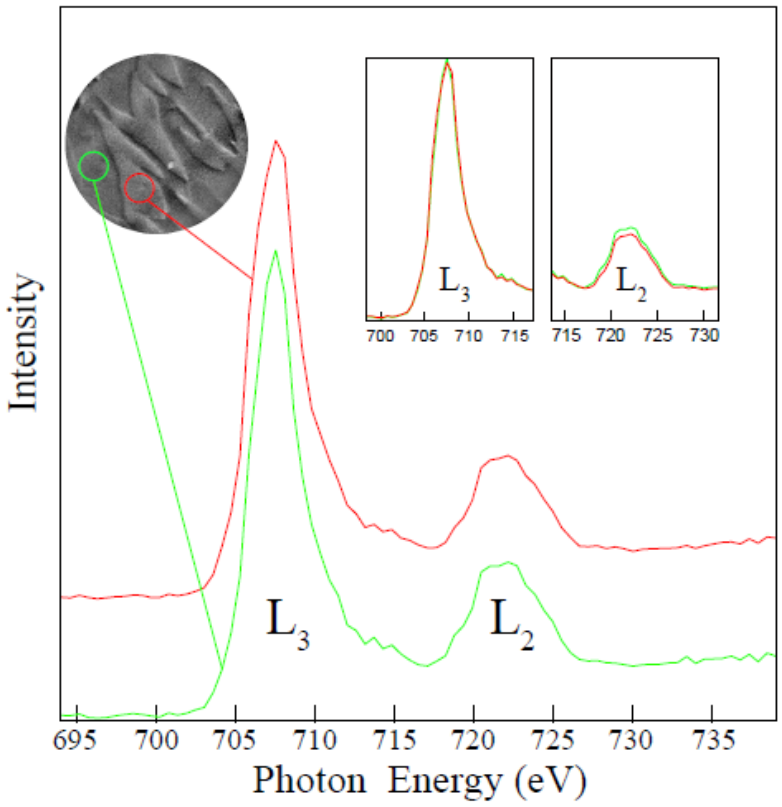

Fig 6.6: *Fe $L_{2,3}$-edge μXAS spectra recorded from region A (red) and region B (green) as defined in fig 6.5. Inset; zoomed in superimposition of spectra show that spectral features are shared and thus the contrast is not due to separate chemical domains.*

The as-prepared Fe_3O_4(111) surface was exposed to 1.2×10^{-6} mbars of pyridine (C_5H_5N) to test the response of the acid/magnetite system to XPEEM measurements. Initially, when the C_5H_5N/Fe_3O_4(111) system was imaged at an energy just above the N K-edge (400 eV), adsorbed pyridine was identified by the intensity apparent on the micro-channel plate (MCP) increasing exponentially. The exposure time for each XPEEM image was of the order of seconds for each image recorded.

6.4 Application of Low Energy Electron Techniques

The technique of LEEM was subsequently employed. While electronic damage to surfaces can occur [25], low energy electrons are a much gentler probe than synchrotron photons and the probability of damage to the surface is dramatically reduced. Imaging the surface with LEEM at the nanoscale can identify surface terminations of the magnetite crystal by using variations in the work function. The resolution required to image the substrate in sufficient detail is at the limit of the capability of the LEEM setup at beamline I06 and technological issues prevented the resolving the surface better than the microscale (High-voltage between the surface and sample could not be maintained.). Figure 6.7 below, shows a typical LEEM image recorded from the Fe_3O_4(111) surface. As with the XPEEM images, contrast is the result of microscale structure and nano-structure domains are not distinguished.

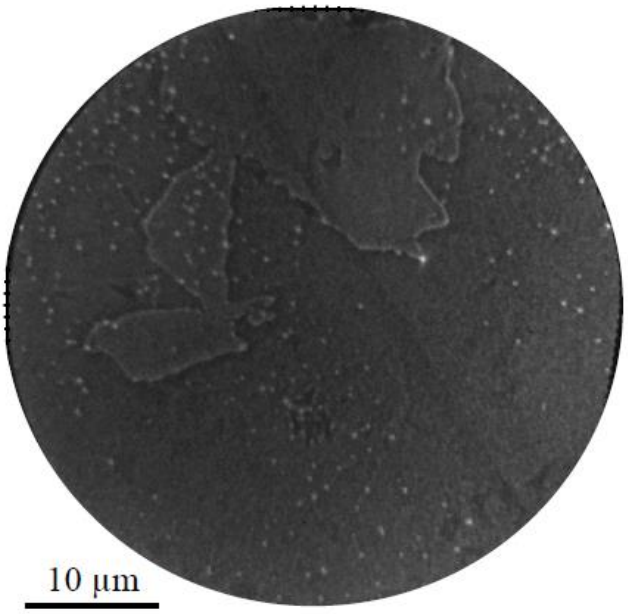

Fig 6.7: *LEEM image recorded from the Fe_3O_4(111) surface (40 µm FOV).*

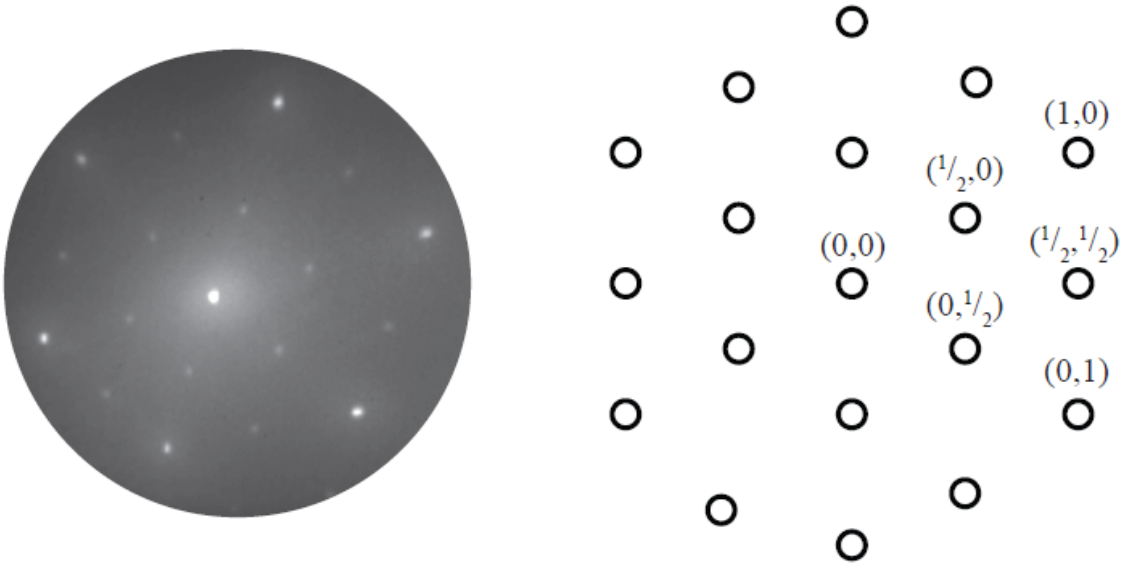

Fig 6.8: *LEED image recorded from the Fe_3O_4(111) single crystal surface. The image left represents an average of LEED patterns recorded between 40-119 eV. Right; a schematic of the relative positions of the Fe_3O_4(111) LEED spots and their corresponding coordinates.*

Removing the contrast aperture from the LEEM caused the MCP to exhibit the LEED pattern of the Fe_3O_4(111) single crystal when the crystal was illuminated by the electron beam. This LEED pattern is presented in figure 6.8 and is in-line with previous observations of the single-crystal and thin-film surfaces [3,10, 13,16]. Scanning the incident energy and capturing images from the MCP facilitated the extraction of LEED I-V spectra in the same manner as XAS spectra from a series of XPEEM data, i.e. the spectra from each LEED spot were recorded by integrating over bright areas of the micro-channel plate (MCP). The intensity from six diffraction spots, (0,0), ($^1/_2$,0), (0,$^1/_2$), (1,0), (0,1) and ($^1/_2$,$^1/_2$) and their symmetrical equivalents were recorded in an energy range between 40-199 eV equating to a dataset comprising 954 eV as the data were recorded in steps of 1 eV. It is advantageous to use LEEM optics for LEED spectroscopy over the traditional rear-view LEED setup. Using LEEM, the diffraction spots remain stationary on the MCP as the energy of the incident electron beam is altered. Additionally, the (0,0) spot is visible, even with perpendicular illumination, as in this case. The experimental LEED I-V spectra are presented in figure 6.9.

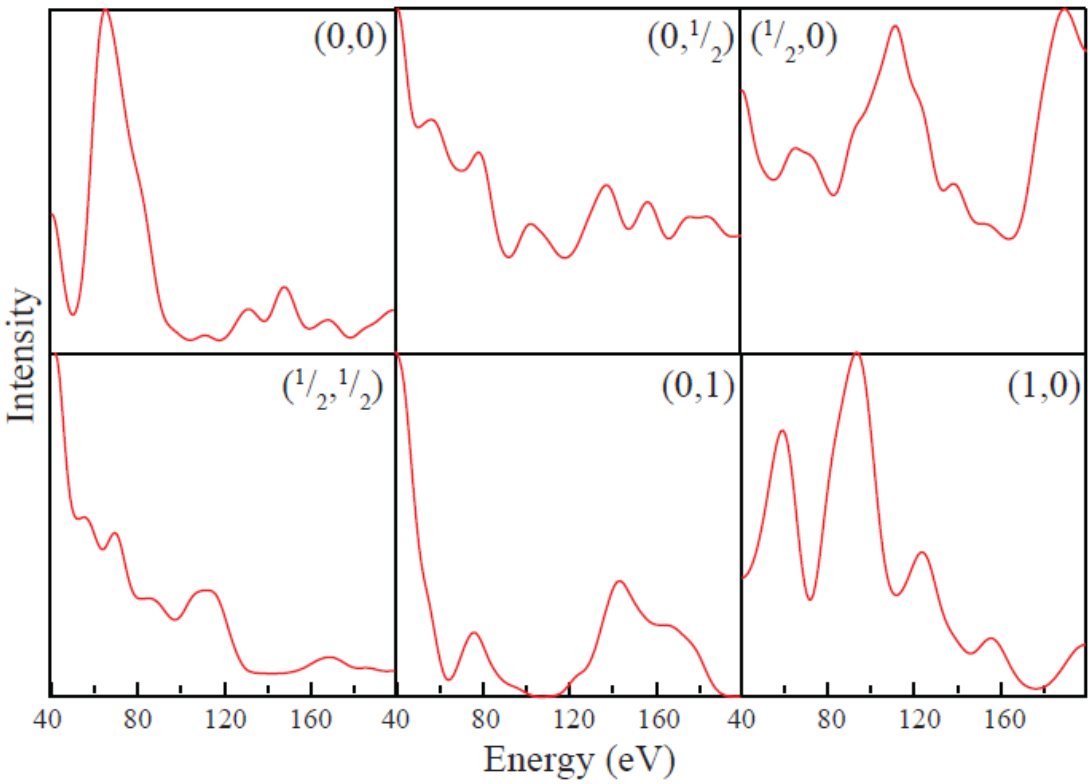

Fig 6.9: *Gaussian-broadened* [26] *LEED I-V spectra extracted from the as-prepared Fe_3O_4(111) surface in the energy range 40-199 eV.*

It is important that noise is eliminated as false spectral features have a strong detrimental effect on structural characterisation by LEED I-V. For the brighter spots such as the (0,0), the curves are smooth (~2000 counts at max). The (0,$^1/_2$) and ($^1/_2$,0) spots are ~20% of the intensity of the (0,0) spot and noise is more likely to cause false spectral features. A solution to this was to apply Gaussian smoothing [26]. Smoothing the spectra carries with it the risk of 'broadening-out' real peaks, though the low overall intensity achieved by the experiment may not facilitate the recording of certain spectral features for some curves in the first place. The smoothed experimental data are compared with the theoretical LEED I-V curves due to these potential difficulties. Such measures could have been avoided by increasing the exposure time during data collection. Each snapshot of the LEED pattern was taken over only 4 s and 159 images comprise each data set. The exposure time for each frame could have been increased

significantly without the overall data collection process becoming problematically time-consuming. The minimum spot-size available for LEED I-V spectroscopy at this beamline is 0.9 μm. The surface of our sample is prepared to be as the surface observed by Cutting *et al* [3], where domains of 100 nm across are observed with STM. In this case, the electron beam would span all three surface terminations simultaneously.

LEED I-V analysis involves generating a set of theoretical spectra from a proposed atomic structure (or 'trial structure') and comparing them with experimentally obtained curves. The reliability factor of Pendry [27], is typically used as a yardstick for how well the proposed surface structure matches the surface structure of the sample. The R-factor is expressed as a number between 0 and ~1, where 0 represents a 'perfect' correlation between experiment and theory. The upper limit for an acceptable R-factor is dependent on the complexity of the system under analysis. For the Fe_3O_4(111) surface, an R-factor between 0.2-0.3 is considered more than acceptable [10,13,16], although this is for a single structural termination. In this study, analysis was carried out with the CLEED [28] software package, which is written in the C programming language. Prior to analysis, phase shifts had to be calculated for each atomic species comprising the material using the Van-Hove phase shift package, written in Fortran [29].

An electron incident on the surface of a material can be described by its wavefuntion:

$$\varphi = aexp(-ib) \tag{6.1}$$

Where a is the amplitude of the wave and b is the phase. The intensity of the wave can be calculated by taking the complex conjugate $\psi\psi* = a^2$. As only elastic scattering is considered in this case, the measured intensity and, by extension, the amplitude remains unchanged and the entire scattering interaction can be described in terms of phase shifts [30]. Phase shifts were created using the Van-Hove phase program for each atomic species (O^{2-}, Fe^{2+} and Fe^{3+}). Shifts pertaining to O^{2-} atoms in the structure calculated for l = 0-9 are presented in figure 6.10. This figure shows that the phase shifts get smaller as the upper limit of the angular momentum quantum number is increased until they have a negligible effect on the simulation. Phase shifts up to $l = \infty$ exist but in practice phase shifts up to l= 5-8 are typically used. In this case l = 9 is calculated because of the large unit cell of iron oxide.

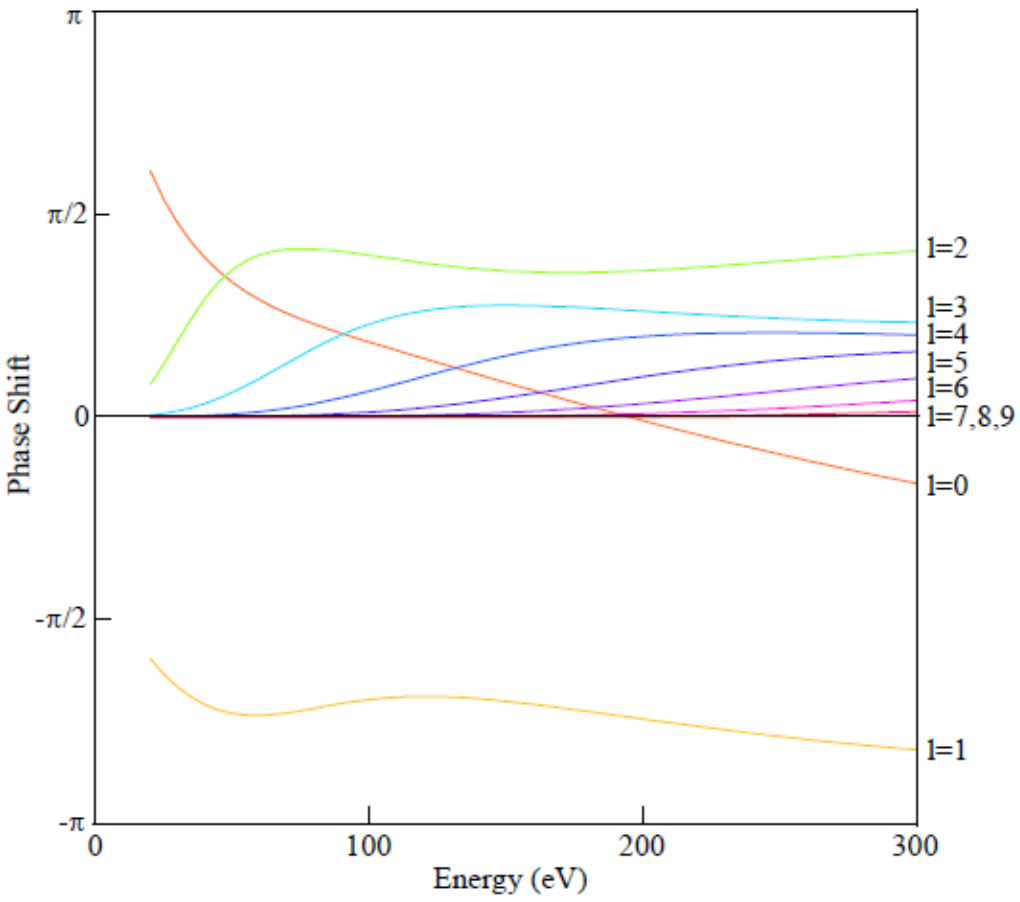

Fig 6.10: *Phase shifts for oxygen in Fe_3O_4 calculated using the Van-Hove phase shift package.*

The calculated phase shifts for each ion comprising Fe_3O_4(111) were assigned a relative geometric coordinate in 3 dimensional space inside two input files; one describing the bulk structure and a second describing the structure of the outermost surface layers. To evaluate whether the phase shifts were a good estimation, the coordinates of Ritter *et al* were used to describe the bulk structure and that of the surface layers [10]. Their system constituted a 10-20 nm Fe_3O_4(111) thin film supported on a Pt(111) substrate. This film was terminated with surface A' only and the terminating atomic ¼ ML of Fe ions was found to relax by 41% [10]. A comparison between the simulation of Ritter *et al* [10] and our own simulation of the same surface is presented below in figure 6.11. Visually, it can be seen that their peak positions are comparable. For the (1,0) spot, the mismatched peaks (highlighted with green squares) appear in the experimental data of Ritter *et al* [10] but not in their simulation.

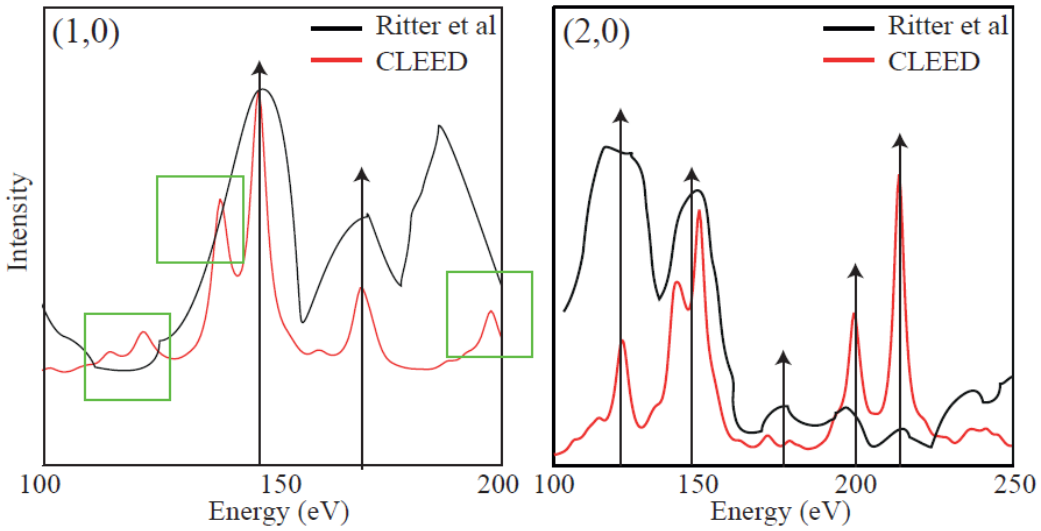

Fig 6.11: *Simulated LEED-IV curves of the Fe_3O_4(111) surface A' from Ritter et al generated using the Van Hove phase shift package (black) compared with the same simulations carried out using CLEED (red). While the peak intensities vary, their positions are in fine agreement. In the (1,0) spectrum the features highlighted in green squares appear in the experimental data of Ritter et al. This is a strong indication that the CLEED program is operating as it should and that our phase shifts generated using the Van-Hove phase shift package are a good approximation.*

LEED I-V characterisation of epitaxial $Fe_3O_4(111)$ thin films have revealed surface A', ¼ ML of Fe ions arranged tetrahedrally on a close packed oxygen layer [10,13,16]. An initial comparison between our experimental data and that of Sala *et al* is drawn in figure 6.12. via the superimposition of curves arising from corresponding spots in the energy region 40-199 eV. The experimental data presented in the figure below that corresponds to our own scrutiny of the single crystal surface has been smoothed using a Gaussian function [26], Gaussian broadening was applied by Sala *et al* to their own data [16]. Green areas of the plots represent energies at which spectral features arise in both data within ~5eV of each other and red regions represent energy regions over which features arise in one spectrum that are not observed in the other. The results of the analysis are unsurprising; there are both consistencies and inconsistencies observed between the spectra. The surface scrutinised by Sala *et al* is comprised entirely of structure A' [16], whereas STM analysis of the single crystal has shown that multiple surface domains (of which surface A' is one) can simultaneously terminate the single-crystal [31-35]. Moreover, for a surface terminated by these three surfaces it would be expected that the half-integer spots would vary more with Sala *et al*'s, than the full-integer spots. The reason for this is that the half-integer $((^1/_2,0),(0,^1/_2),(^1/_2,^1/_2))$ spots are caused by diffraction from iron atoms in surface A'. In the other two surfaces, these iron atoms are capped by an oxygen atom. The integer ((1,0),(0,1)) spots in all three surfaces arise from a close packed oxygen layer, with the same surface unit-cell and differences between their spectral features should be caused by interference from the 'half-integer' layer above. It can be seen below that there is a far greater difference between the half-integer spectra from each surface and this could possibly be explained by different absorption sites in each case.

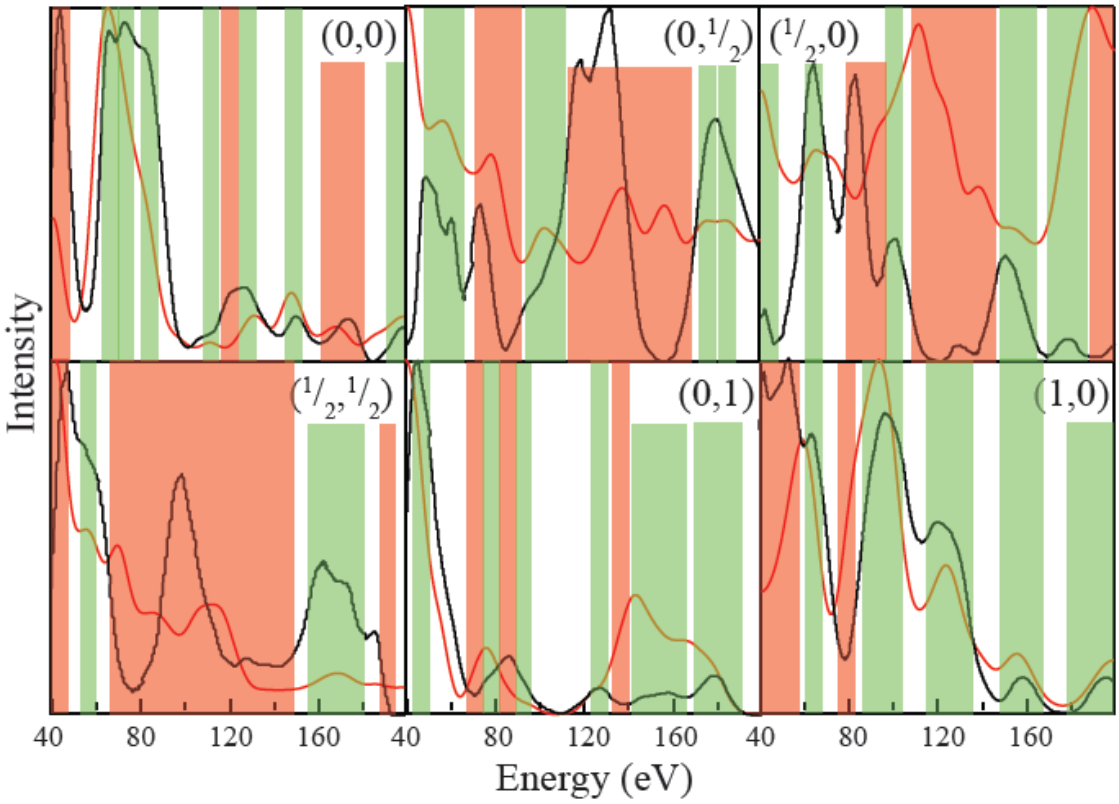

Fig 6.12: *Experimentally obtained LEED I-V spectra from the Fe_3O_4(111) single crystal surface compared with spectra obtained experimentally from the Fe_3O_4(111) thin-film surface. Both sets of spectra were recorded in the energy region 40-199 eV and were processed using a Gaussian function* [16, 26].

The work of Sala *et al* describes an analysis where 180º rotated domains of surface A' are considered [16]. The extent of each domain has been shown to influence the accuracy of LEED I-V analysis for this surface [10,16]. Ritter *et al* [10] found that the R-factor of their analysis of surface A' was more than halved by the consideration of additional rotated domains. It is likely that the presence of additional structural domains affecting our own data greatly weight the extent of difference between the spectra considerably. It can be concluded that, based only on previous STM studies, while surface A' is likely to feature on the single-crystal surface, it is probably present alongside further surfaces. A visual analysis of the curves is rudimentary,

however, and a surface wholly terminated by surface A' is proposed (among many other trial structures) for full LEED I-V analysis.

Initially, the atomic coordinates of Ritter *et al* of surface A' [10] are used to geometrically distribute the phase shifts of the oxide, as they describe the thin-film surface well, before they are modified to surfaces A and B. A total of 7 trial surfaces were analysed with the CLEED software and compared with the experimental curves presented in figure 6.9. Three trial structures incorporate a single termination (A, A' or B) and a further 4 trial structures consider all possible combinations of these surfaces. The *CLEED* software was not prepared to deal with co-existing surface structures and modifications were made to the code to accommodate trial surface co-habited by distinct atomic arrangements. A flow chart describing the interplay between the 3 programs comprising the *CLEED* software package is included as figure 6.13. The R-factor between the intensity curves generated by the *Nsym* program from the proposed surface structure is calculated by the *Crfac* program. The R-factor is then fed to the *Search* program, which varies the geometric parameters of the surface using the downhill simplex method [36,37]. This modified trial structure is passed to the *Nsym* program to generate new theoretical curves and a new R-factor is calculated. The R-factor continues to drive the search program until the best possible fit is reached. The upper limit for the extent of movement of an atom from its original user-proposed position by the *Search* program is ±0.1 Å.

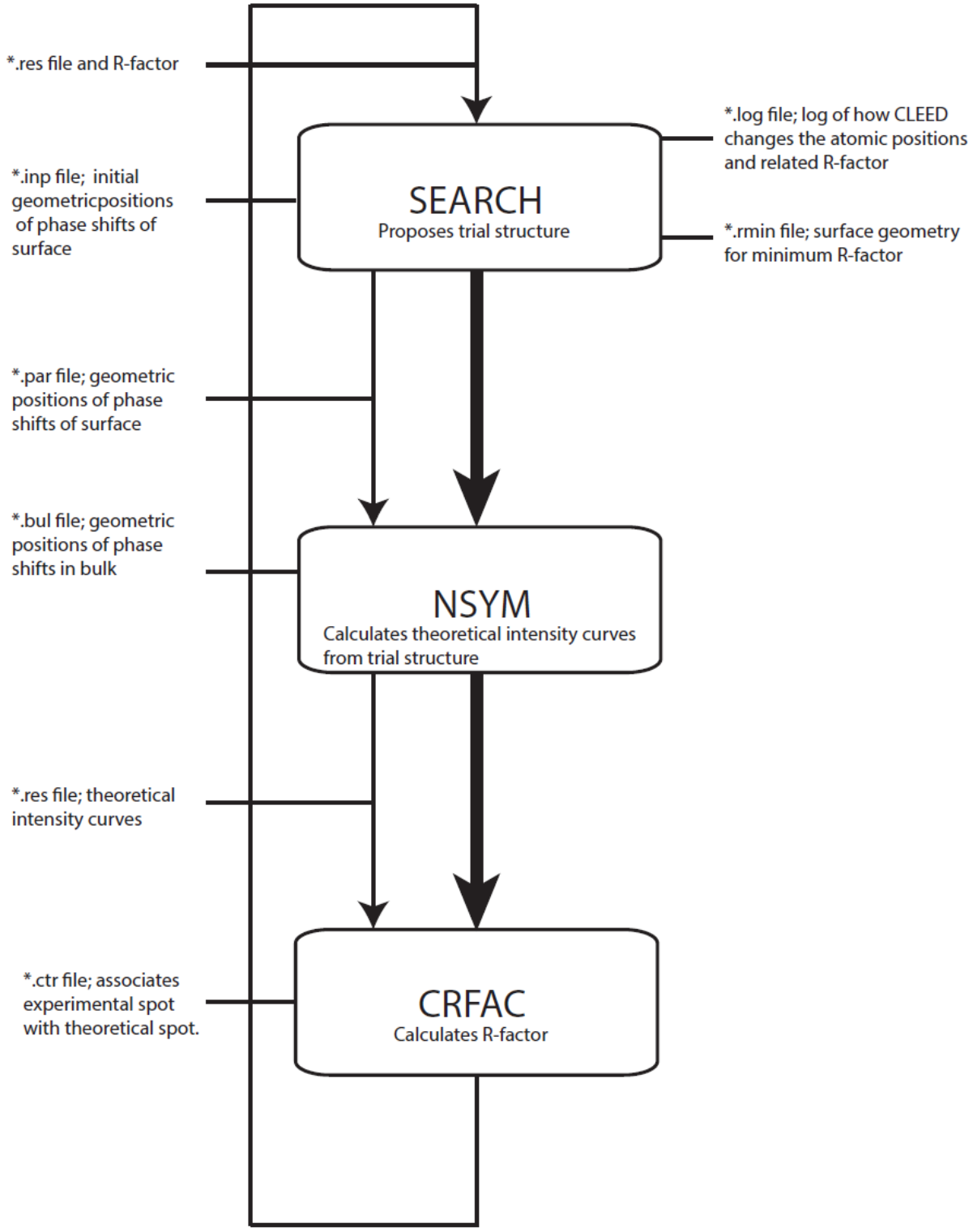

Fig 6.13: *Flow chart describing the exchange between the 3 programs that constitute the CLEED software package.*

The code was modified so that *Nsym* could generate curves for *N* surfaces. Prior to passing the curves to *Crfac* for comparison with experimental data, the *N* sets of curves were added together to create one set of I-V curves representing the surface. Previous characterisations of the Fe_3O_4(111) surface have been complicated by 180º rotated Fe_3O_4 domains [10,16]. A knowledge of the relative weight of these domains is also essential and in previous studies were carefully scrutinised using LEEM or STM [10,16]. An Fe_3O_4(111) surface with domains rotated relative to each other by 180º would cause blending of the ($^1/_2n$,0) with the (0,$^1/_2n$) spectra, where *n* is any integer. A rotated domain could be introduced as an additional surface. Sala *et al* report from LEEM analysis a 94:6 ratio of one rotational domain to the other and rotated domains were omitted from our own characterisation. Effective LEEM data would have provided *a priori* knowledge of the relative coverage of the domains, as well as the relative concentration of each structurally distinct termination, which would greatly improve the accuracy of this analysis. The R-factor corresponding to each spot on each surface as well as the total R-factor for each surface for the Gaussian modified data (figure 6.9) are presented in table 6.1.

Surface	(0,0)	(0,½)	(½,0)	(½,½)	(0,1)	(1,0)	Total
A	0.88	0.80	0.92	0.86	0.87	0.92	0.87
A’	0.84	0.88	0.88	0.96	0.96	0.61	0.85
B	0.84	0.97	0.83	1.00	0.87	0.87	0.91
AA’	1.00	0.85	1.00	0.88	0.91	0.89	0.93
BA’	0.98	0.93	1.00	0.90	0.80	0.85	0.92
BA	1.00	0.89	0.86	0.96	0.80	1.00	0.94
BAA’	0.82	0.81	0.84	0.86	0.90	0.63	0.81

Table 6.1: *R-factors corresponding the extent of agreement between various trial structures based on STM characterisation of the single crystal and thin-film $Fe_3O_4(111)$* [3, 31-35] *surface compared with experimental LEED I-V recorded from the $Fe_3O_4(111)$ single crystal surface.*

There are no suitable matches with the surface. The analysis was hindered considerably by incomplete experimental data. It is commonplace that perpendicular alignment of the incident beam is determined by a good agreement between the intensities of symmetrically equivalent spots [38-40]. The MCP in beamline I06 is hindered by a spatial inconsistency in efficiency as encountered in the experiment described in chapter 4 (carried out at the same beamline). In figure 6.14 the intensities of the spots pertaining to the (1,0) LEED spot and its symmetrical equivalents over the energy range 40-199 eV are presented. Variations in the intensity of the symmetrically equivalent peaks are evident visually and furthermore, distinct spectral features are observed. This could be the result of the incident beam being misaligned or the effect of spatial variations across the channel plate. It therefore cannot be said certainly that the electrons are at a 90º angle of incidence in our experimental setup. The LEED I-V experiment is sensitive

to minor changes to the incident angle of the electron beam [41-43]; changing the incident angle of the electron beam causes the spectra of symmetrical spots to differ from each other. This phenomenon must be accounted for even in instances where a tilt of up to 5º off-normal of the electron beam is observed [42]. Because of the damaged channel-plate, a tilt cannot be identified/quantified and it is unknown if the channel plate is capable of capturing data with a high enough resolution for analysis. The data is unsuitable for LEED I-V analysis, particularly for that of a complicated multi-terminated transition metal oxide and furthermore, quantitative characterisation of structural and associated rotational domains is not available.

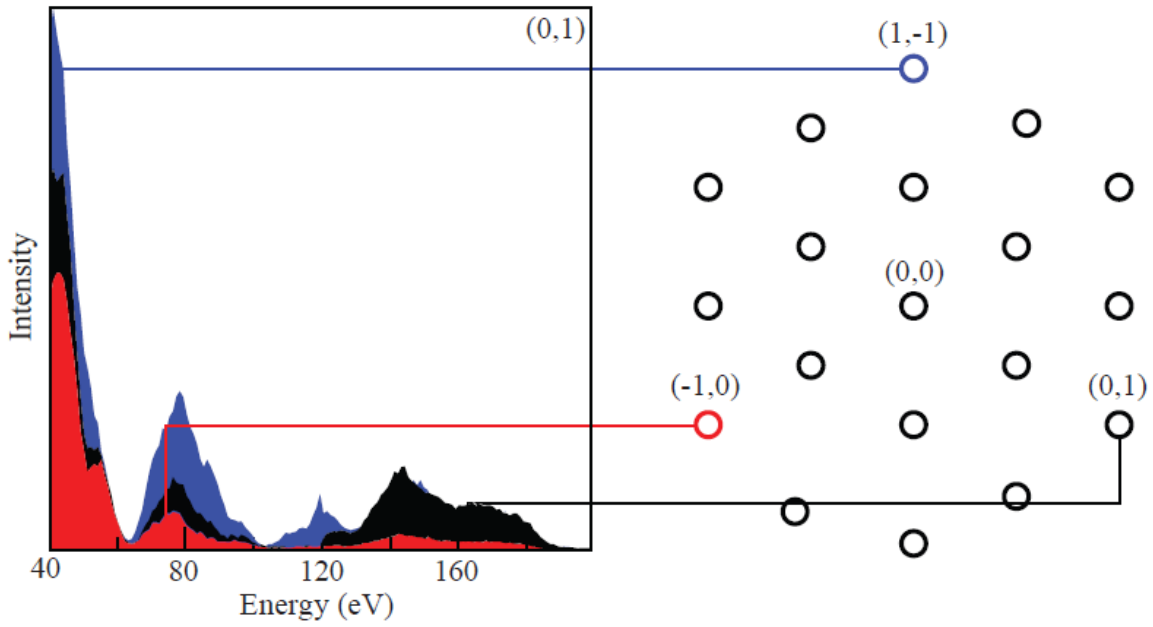

Fig 6.14: *LEED I-V spectra associated with the (1,0) spot and its symmetrical equivalents.*

While a good agreement factor could not be established in the analysis, a simulation that shared all of the experimental peaks, however out of proportion the relative intensities, would be encouraging and could go some way to explaining the difference between our experimental curves and those of Sala *et al* and serve as a starting point for the characterisation of more in-

depth data. The only set of theoretical curves generated with spectral features matching in energy positions of those in the experimental data are from the trial surface incorporating all three surfaces as presented in figure 6.15. While all of the peaks in the experimental data are accounted for by this simulation and these correlated peaks are highlighted together in green bars, there are some peaks arising only in the simulated curves that must be explained. It is possible that these peaks are simply in the experimental data as they were not picked up by the damaged channel plate, or because the experiment occurs at a slightly tilted incidence. Moreover, as the extent of the coverage of each surface and it's rotationally symmetric equivalents is not known, it is possible that peaks that appear prominent in our simulation would be broadened out, or shrunk to negligible levels. Our own simulation assumes an equal coverage of each surface and does not account for rotated domains. This is again a rudimentary characterisation of the surface. In actuality, the poor quality of the experimental apparatus has rendered suitable characterisation of the relative extents of previously observed domains on this surface impossible and the production a good reliability factor from LEED I-V analysis has not been possible. It is noteworthy that simulated curves comprising all three surfaces shares all of the peaks observed experimentally from the single-crystal surface, while experimental data from the thin film surface does not compare as well. It cannot be said that our experimental spectra represent an electron beam incident at 90º due to large inconsistencies in symmetrically equivalent spectra, however. And it is not clear if this is due to spatial inconsistencies in the channel-plate onl

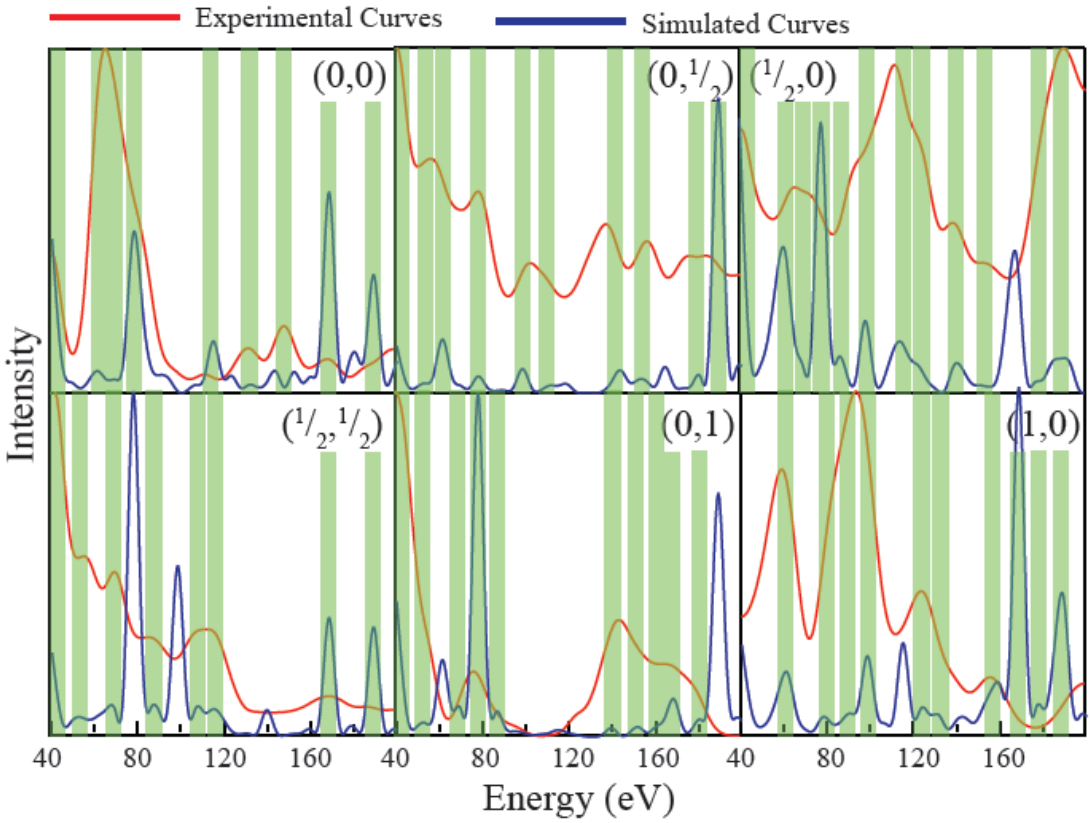

Fig 6.15: *Experimental LEED spectra from the Fe_3O_4(111) single-crystal surface (red), compared with equivalent simulated curves from a trial structure incorporating an additive, equally-weighted contribution from surfaces A',A and B. Where peaks occur at the same incident energy they are enclosed by a green square.*

6.5 Summary

Structural characterisation was carried out of the Fe_3O_4(111) single crystal surface using surface-science techniques. The surface was prepared with cycles of sputtering and annealing to 900 K. The experiment was set up to confirm three surface terminations, previously identified by STM by chemically characterising the reactants across the surface following exposure to acids that exhibit variable oxide chemistry, i.e. pyridine, formic acid and the

carbon tetrachloride. Removal of the adsorbate from the surface under the X-ray beam rendered characterisation by chemically-sensitive X-ray microscopy impossible, however. LEED I-V

was carried out, a technique that could also be used to structurally characterise the surface but with a significantly diminished risk of damage to the system by the probe particles. Analysis of symmetrically equivalent LEED spots revealed that a structural analysis by this route was not possible. Theoretical LEED I-V spectra were generated using the LEED analysis software *CLEED* for a number of trial structures, chosen to mimic previous STM studies of the thin-film and single-crystal surfaces and produced by modifying the atomic coordinates of Ritter *et al* for the iron terminated surface. A good reliability factor could not be established, however. Visual inspection showed that our simulation of a surface terminated by three distinct structures simultaneously had peaks that matched those of our experimental data, which was heavily mismatched with the experimental data of Sala *et al* from the thin film surface. This is the expected result as STM work of this thin film surface revealed a single structural termination, while previous STM analysis has shown the three surfaces proposed for out trial structure to cohabit the surface. Due to spatial inconsistencies in the channel plate efficiency, the tilt of the incident beam from the sample could not be characterised with certainty and it cannot be said that our experimental conditions match those of Sala *et al* or our simulations. A spatially uniform channel-plate combined (or performing the experiment on the rear-view LEED system in the preparation chamber) with on-site characterisation of the surface with LEEM or STM would have made it more possible to characterise the structure with our modified version of the *CLEED* software.

References

[1] R.M. Cornell and U. Schwertmann, *The Iron Oxides 2nd Ed.* (2003) Wiley.

[2] Z. Zhang and S. Satpathy, *Physical Review B*, **44** (1991) 13319.

[3] R.S. Cutting, C.A. Muryn, G. Thornton and D.J. Vaughan, *Geochemica et Cosmochimica Acta*, **70** (2006) 3593.

[4] R.E. Tanner, Y. Laing and E.I. Altman, *Surface Science*, **506** (2002) 251

[5] S.L. Silva, A.A. Patel, T.M. Pham and F.M. Leibsle, *Surface Science*, **441** (1999) 351

[6] S. Suzuki, Y. Yamaguchi, H. Oshini, K. Fuhui, T. Sasaki and Y. Iwasawa, *Catalysis Letters*, **50** (1998) 117.

[7] K. Abib, N. Camillone, J.P. Fitts, K.T. Rim, G.W. Flynn, S.A. Joyce and R.M. Osgood, *Surface Science*, **497** (2002) 127.

[8] K.T. Rim, T. Muller, J.P. Fitt, K. Adib, N. Camillone, R.M. Osgood, E.R. Batista, R.A. Friesner, S.A. Joyce and G.W. Flynn, Journal of Physical Chemistry B **108** (2004) 16753.

[9] S.S. Dhesi, S.A. Cavill, A. Potenza, H. Marchetto, R.A. Mott, P. Steadman, A. Peach, E.L. Shepherd, X. Ren, U.H. Wagner and R. Reininger, *AIP Conference Proceedings*, **1234** (2010) 311.

[10] M. Ritter and W. Weiss, *Surface Science*, **432** (1999) 81.

[11] G.J.P. Abreu, A. Pancotti, L.H. de Lima, R. Landers and A. de Siervo, *Journal of Nanoparticle Research*, **15** (2013) 1510.

[12] G. Ketteler and W. Ranke, *Journal of Physical Chemistry B*, **107** (2003) 4320.

[13] A. Barbieri, W. Weiss, M.A. Van Hove and G.A. Somorjai, *Surface Science*, **302** (1994) 259.

[14] W. Weiss, A. Barbieri, M.A. Van Hove and G.A. Somorjai, *Physical Review Letters*, **71** (1993) 259.

[15] W. Weiss and M. Ritter, *Physical Review B*, **59** (1999) 5201.

[16] A. Sala, H. Marchetto, Z.-H. Qin, S. Shaikhutdinov, Th. Schmidt and H.-J. Fruend, *Physical Review B*, **86** (2012) 155430.

[17] I. Leonov, A.N. Yaresko, V.N. Antonov and V.I. Anisimov, *Physical Review B*, **74** (2006) 165117.

[18] Z.Y. Wu, S. Gota, F. Jollet, M. Pollak, M. Gutier-Soyer and C.R. Natoli, *Physical Review B*, **55** (1997) 2570.

[19] Y. Ma, P.D. Johnson, N. Wassdahl, J. Guo, P. Skytt, J. Nordgren, S.D. Kevan, J.E. Rubensson, T. Böske and W. Eberhardt, *Physical Review B*, **48** (1993) 2109.

[20] A.R.B. de Castro, P.T. Fonseca, J.G. Pacheco, J.C.V. da Silva, E.G.L. da Silva and M.H.A. Santana, *Journal of Magnetism and Magnetic Materials*, **233** (2001) 69.

[21] S. Gota, F. Jollet, J.P. Crocombette, Z.Y. Wu, M. Pollak, N. Thromat, M. Gautier-Soyer and C.R. Natoli, *Journal de Physique IV France*, **7** (1997) 507.

[22] O. Bezencenet, D. Bonamy, R. Belkhou, P. Ohresser and A. Barbier, *Physical Review Letters*, **106** (2011) 107201.

[23] G. van der Laan, N.D. Telling, A. Potenza, S.S. Dhesi and E. Arenholz, *Physical Review B*, **83** (2011) 644409.

[24] J.P. Crocombette, M. Pollak, F. Jollet, N. Thromat and M. Gautier-Soyer, *Physical Review B*, **52** (1995) 3143.

[25] R.F. Egerton, P. Li and M. Malac, *Micron*, **35** (2004) 399.

[26] P. Marchand and L. Marmet, *Review of Scientific Instruments*, **54** (1983) 1034.

[27] J. B. Pendry, *Journal of Physics C: Solid State Physics*, **13** (1980) 1937.

[28] G. Held, *CLEED Manual*, private communication.

[29] M. Van Hove, private communication.

[30] L.J. Clarke, *Surface Crystallography: An Introduction to Low Energy Electron Diffraction 1st Ed*. (1985) Wiley.

[31] F.C. Voogt, T. Fujii, T. Hibma, M. Hoefman, P.J.M. Smulders, G.H. Wijnja, G.L. Zhang and L. Neisen, *Hyperfine Interactions*, **98** (1996) 99.

[32] W. Weiss, *Surface Science*, **377** (1997) 99.

[33] Y.J. Kim, C. Westphal, R.X. Ynzunza, Z. Wang, H.C. Galloway, M. Salmeron, M.A. Van Hove and C.S. Fadley, *Surface Science*, **416** (1998) 68.

[34] S.K. Shaikhutdinov, M. Ritter, X.G. Wang, H. Over and W. Weiss, *Physical Review B*, **60** (1999) 11062.

[35] S.K. Shaikhutdinov, W. Weiss and R. Schlogl, *Applied Surface Science*, **161** (2000) 497.

[36] W. H. Press, B. P. Flannery, S. A. Teukolsky and W. T. Vetterling, *Numerical Recipes in C* (1988) Cambridge University Press.

[37] J.A. Nedler and R. Mead, *Computer Journal*, **7** (1965) 308.

[38] M.K. Debe and D.A. King, *Journal of Physics C:Solid State Physics*, **15** (1982) 2257.

[39] V.B. Nascimento, R.G. Moore, J. Rundgren, J. Zhang, L. Cai, R. Jin, D.G. Mandrus and E.W. Plummer, *Physical Review B*, **75** (2007) 035408.

[40] G. Teeter, J.L. Erskine, F. Shi and M.A. Van Hove, *Physical Review B*, **60** (1999) 1975.

[41] W. Reimer, V. Penka, M. Skottke, R.J. Behm, G. Ertl and W. Moritz, *Surface Science*, **186** (1987) 45.

[42] S. Karakatsani, Q. Ge, M.J. Gladys, G. Held and D.A. King ,*Surface Science*, **606** (2012) 383.

[43] I. Karas, J. Houfek and V. Matolín, *WDS '05 Proceedings of Contributed Papers*, **3** (2005) 580.